Dynamic Modelling and Experimental Validation of the IS2-CVT Transmission Technology

Römers, L.H.J.

Award date:
2008

Dynamic Modelling and Experimental Validation of the IS^2-CVT Transmission Technology

L.H.J. Römers

DCT 2008-069

Confidential

Master Thesis

Supervisors: Prof. dr. ir. M. Steinbuch (TU/e)
Dr. ir. A.F.A. Serrarens (TU/e)
Dr. ir. B.G. Vroemen (DTI)

Eindhoven University of Technology
Department of Mechanical Engineering

Drivetrain Innovations BV

Eindhoven, June 2008

Summary

Recent developments in automotive technology show an increasing popularity of various new (semi-)automated transmission systems for passenger cars. Market shares of automated manual (AMT), dual clutch (DCT) and continuously variable transmissions (CVT) are increasing steadily. Not so long ago, the customer could only choose between a manual or a conventional automated transmission system. The fact that the average driver nowadays expects more comfort and less workload contributes to the rising popularity of automated transmissions. Improvements in fuel consumption figures, both for economic as well as environmental reasons, also play a significant role in recent developments. These are also the main incentives for manufacturers to focus strongly on hybrid technology, which is inherently 'automatic'.

The focus of this report will be on an innovative adaptation of the continuously variable transmission system. Although the efficiency of a CVT is less than that of a conventional AT or MT, overall fuel consumption is reduced considerably because the combustion machine can be operated in a fuel efficient manner. This generally means operating the engine at low rotational speeds and relatively high torque levels. The fuel saving potential of this transmission system has a significant drawback, which is bad acceleration response. Known also as jet-start or rubber-band effect, it is a direct consequence of fuel economic steady-state engine operation at high torque level and low speed. When a large increase in power output is requested, the system has trouble to deliver a fast response, which is caused by inertial delay. This means that better fuel economy comes at the expense of driveability.

Drivetrain Innovations BV has invented a solution for this penalty on driveability, while at the same time improving fuel economy even further. The concept is named the *IS²-CVT*, which is a mechanical add-on module fitted into an existing CVT housing, without the need for large adaptations. A steel flywheel unit is used to provide a purely mechanical assist during downshift transients, virtually eliminating rubber-band behaviour. Furthermore the flywheel unit is used to enable an engine idle-stop functionality during vehicle standstills, resulting in considerable fuel savings during city driving. Kinetic energy stored in the flywheel is used for fast re-starts of the combustion engine. The two main functions mentioned above go by the names *Impulse Shift* and *Impulse Start*, hence the name IS²-CVT.

This thesis will focus on the dynamic behaviour of this new powertrain and all of its functionalities. Since a prototype has already been developed, system behaviour can be validated, analysed and improved both in simulation and through experiments.

Contents

Chapter 1

Introduction

1.1 Developments in automotive transmission technology

Manual transmissions are still the most common in European passenger cars. Low costs, small packaging and high efficiency contribute to their success. The fact that a manual transmission (MT) provides the driver with a high level of control in combination with a high mechanical efficiency might be its biggest benefits. Despite these advantages, developments in automotive technology show an increasing popularity of various automated transmission systems for passenger cars. Market shares of concepts like conventional automatic transmissions (AT), automated manual (AMT), dual clutch (DCT) and continuously variable transmissions (CVT) are increasing steadily. Additionally, various hybrid powertrains are being introduced. Reduction of driver workload, better comfort and improved fuel economy are the main drivers to look for other transmissions than the conventional manual transmission. Current developments in environmental policy aim at a reduction of greenhouse gasses. For passenger cars this means reducing CO_2 emissions, which directly corresponds to improving overall fuel economy. Rising fossil fuel prices are another important motive for better fuel economy in passenger cars.

1.2 EcoDrive project

In 1997 the *EcoDrive* project was initiated to develop a new CVT based powertrain for passenger cars. EcoDrive was a cooperation between Van Doorne's Transmissie (VDT), the Technische Universiteit Eindhoven (TU/e) and TNO Automotive. The goal of the project was to achieve considerable fuel savings for a CVT based powertrain without compromising driveability.
Conventional CVT powertrains are unable to achieve both optimal fuel economy and good driveability at the same time. This paradox is caused by unwanted inertial effects encountered in a CVT based powertrain. While trying to find a solution for this paradox, a concept using an additional flywheel inertia resulted. The so-called Zero Inertia (ZI) powertrain exchanges kinetic energy between a steel flywheel and engine sided inertias. This enables optimisation of engine operating points for good fuel economy without penalizing driveability. To achieve a further reduction in fuel consumption, a ZI 'Stop-Go' version was developed. The 'Stop-Go' functionality enables engine shutdowns at vehicle

standstill, thereby saving additional fuel. Stored kinetic flywheel energy is used for engine restarts.
During the course of the EcoDrive project the assessment, modelling, control and testing of the Zero Inertia powertrain was realized. The project was assigned to three Ph.D. students, who earned their Ph.D. on different research topics within EcoDrive. In [2] the focus lies on the mechanical design and construction of the ZI transmission. The coordinated control of the ZI powertrain is treated in [10]. Finally in [11], component control of the ZI powertrain is the main topic. The target of the EcoDrive project was to achieve a 25% reduction in fuel consumption with respect to a 4-speed automatic transmission on the NEDC drive cycle, without compromising driveability. By means of the ZI (incl. 'Stop-Go') concept, an estimated 18% reduction in fuel consumption was achieved. Furthermore, driveability of the ZI powertrain was improved compared to the reference vehicle.

1.3 Drivetrain Innovations B.V.

After obtaining their Ph.D., the three researchers founded the company Drivetrain Innovations B.V. (DTI). DTI develops new and innovative transmission systems, aiming for better fuel economy and driveability. Various concepts are currently under development, ranging from applications for AMT and CVT transmissions in small to medium size passenger cars, high end sports road cars and heavy-duty trucks.

1.4 Master thesis objective and outline

One concept currently under development at DTI is the so-called IS^2-CVT. This concept is a successor of the Zero Inertia powertrain mentioned earlier. Similar to the (EcoDrive) ZI powertrain, the IS^2 concept enables the combination of low fuel consumption along with good driveability. Although the goals of both concepts are virtually the same, the topology and layout of both powertrains is different, as will become clear later on.
The IS^2 concept is an add-on transmission module designed to fit into an already existing CVT housing, without the need for large adaptations, as was the case for the ZI powertrain. The first function of the IS^2-concept is to use flywheel kinetic energy for counteracting unwanted inertial effects seen in conventional CVT drivetrains. In conventional CVT's usually additional fuel consumption has to be sacrificed to neutralize the inertial effects, or more general to improve driveability. Through exploiting the *Impulse Shift* functionality of the IS^2-concept, no compromise needs to be made between fuel economy and driveability. Next to Impulse Shift, the flywheel unit is used to eliminate idle fuel consumption at standstill, by means of an idle-stop functionality. Quick restarts of the engine are enabled by the so-called *Impulse Start* functionality, being the second operation mode within the IS^2-concept. The ability to shutdown and quickly restart the combustion engine from standstills results in considerable fuel savings, especially during stop-and-go city driving. Currently a prototype of the IS^2-CVT is ready for demonstration.

In Chapter 2 a system description is presented for both the reference as well as the IS^2 drivetrain. The working and functionalities of both conventional and new components will be elaborated. Furthermore, the theoretical background of the Impulse Shift and Impulse Start functionalities is introduced. In Chapter 3 a torsional compliance model describing the dynamics of the powertrain is presented. It will be used in later chapters for analysis and simulation purposes. A torsional vibrations analysis is carried out in Chapter 4.
The theoretical background and experimental validation of the Impulse Start functionality is covered in Chapter 5. A performance analysis of Zero Inertia shifting versus Impulse shifting is presented in Chapter 6. In Chapter 7 a method for dynamic set point generation is presented. It is validated by measurements done in the vehicle, for both Zero Inertia as well as Impulse shifting.
In Chapter 8 the realized improvement in fuel consumption is considered. Measurements done with the conventional CVT are compared to measurements with the fully functional IS^2-CVT. Finally, conclusions and recommendations are presented in Chapter 9.

Chapter 2

System description

2.1 Conventional CVT powertrain

The term *powertrain* refers to the whole system needed to propel the vehicle. It comprises all components ranging from the power source to (but not including) the drive shafts and wheels. The base powertrain on which the IS^2 concept is based, is shown in figure 2.1. It contains a four cylinder gasoline engine which is used to power the front wheels over a continuously variable transmission (CVT). Being positioned between the engine and the drive shafts, the CVT contains a torque converter, a hydraulic pump, a drive/neutral/reverse set, a variator, a final drive stage and a differential.

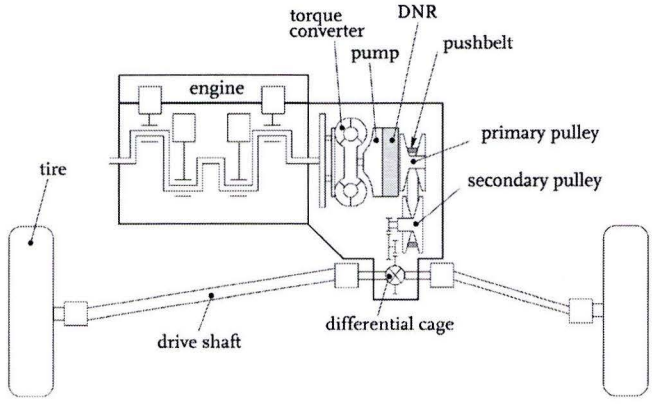

Figure 2.1: conventional CVT powertrain

Figure 2.2 shows a schematic representation of the CVT based powertrain. A torque converter acts as launch device, transmitting and amplifying engine torque during vehicle launch. To prevent unnecessary slip losses, a lockup clutch inside the torque converter is engaged at the end of the launch process. The drive/neutral/reverse set contains a planetary gear set and two clutches. Engaging either clutch enables driving forwards or backwards. An engine driven hydraulic pump provides pressure for the hydraulic circuit. Besides delivering oil flow for cooling and lubrication purposes, it also enables actuation of the variator and all present clutches.

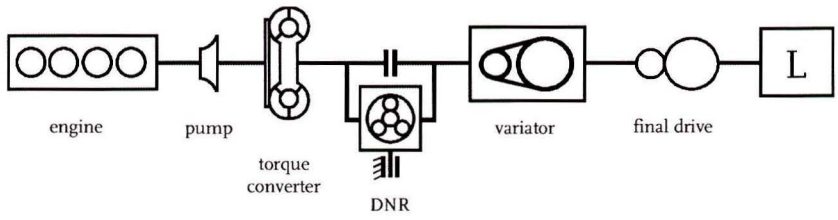

Figure 2.2: schematic representation of a conventional CVT powertrain

A construction drawing of the reference CVT can be found in appendix J.1. The variator forms the heart of the transmission and consists of two hydraulically actuated pulleys and a steel pushbelt. A picture of a variator produced by *Van Doorne's Transmissie* can be seen in figure 2.3(a). Each pulley has one rigid and one axially moveable conical disc, enabling it to clamp the pushbelt at a continuous range of radii.

Figure 2.3(b) schematically shows cross-sections of the variator at three typical ratios, being underdrive (or low ratio), medium and overdrive. Note the difference in axial position of the moveable pulley sheaves. Changes in ratio are accomplished by directing hydraulic fluid into and out of the primary sided pulley. This way, transmission ratio can be controlled automatically and continuously, reducing driver workload and increasing comfort. Normal forces needed to clamp the belt are generated by hydraulic pressure in both pulleys.

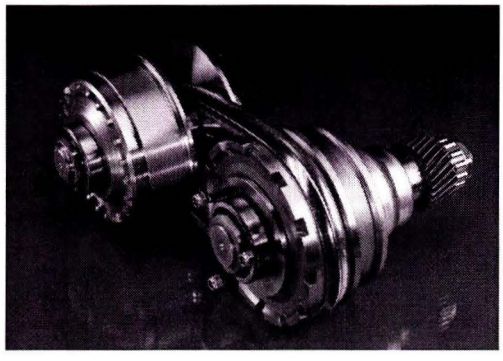

Figure 2.3(a): Van Doorne's Transmissie variator

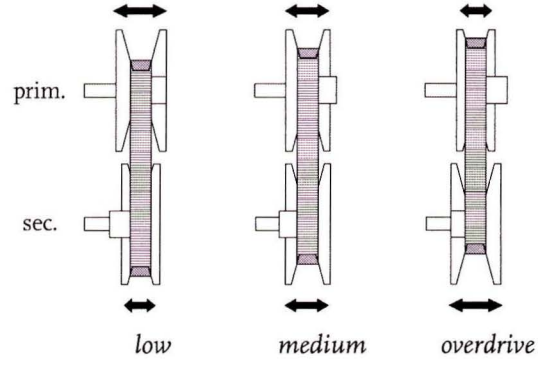

Figure 2.3(b): schematic variator cross-section

The large ratio coverage of the variator enables it to operate the combustion engine in fuel efficient operating points. This operating strategy is known as E-line (efficiency-line) tracking. It is displayed graphically in figure 2.4 by means of an engine map. The top curve corresponds to maximum engine torque, or wide-open-throttle (WOT) torque, of the 1.3L gasoline engine present in the test vehicle. The contour lines correspond to different levels of brake specific fuel consumption (BSFC), being a measure for engine efficiency.
A certain engine power output can be realised with various combinations of speed and torque, as indicated by the constant power hyperbolas. Along each power hyperbola different BSFC values can be seen. By finding the minimum value at each hyperbola and

subsequently connecting these operating points, the E-line can be constructed. Fuel consumption can be reduced significantly be applying an E-line tracking strategy. For example, an output power of 6 kW can be realised both in operating point A as well as B. Both operating points show different BSFC values however, approximately 310 g/kWh in point A and 255 g/KWh in point B. This means that by choosing the operating point located on the E-line, fuel consumption would be reduced by 18%.

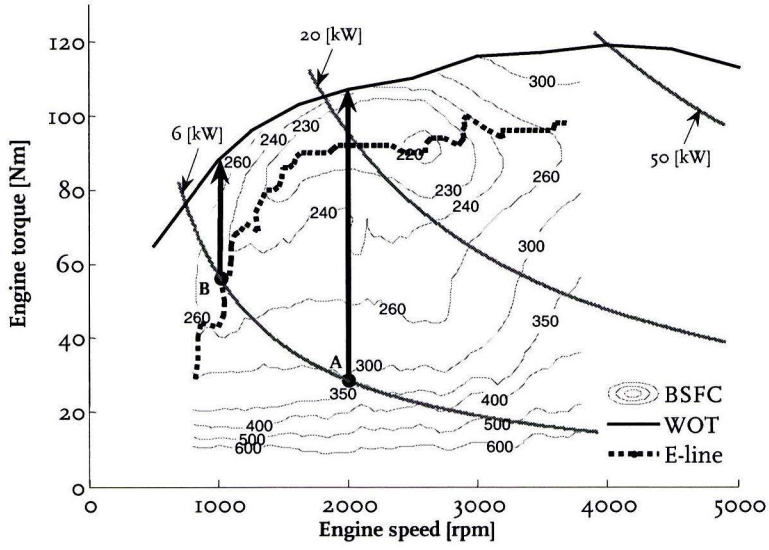

Figure 2.4: engine map with BSFC curves

Although significant improvements in fuel economy can be made by E-line tracking, there also is a drawback. Because the E-line is positioned at fairly high torque levels, only little extra torque is available before reaching the maximum torque curve. This so-called torque reserve is the additional torque which is instantly available when the driver presses the accelerator pedal. During operation on the E-line, torque reserve corresponds to the distance between the E-line and the WOT-curve. Both arrows in figure 2.4 indicate the torque reserve for two operating points at 6 kW. When the driver demands a power increase, the torque reserve in operating point B would result in a power increase of approximately 3 kW, to a total of 9 kW. In the case of point A, a much larger torque reserve is available, enabling an instant power increase of 15 kW to a total of 21 kW.

This example shows that raising the engine torque from the E-line to WOT-level results in little additional power. A large increase in power output can only be accomplished by increasing engine speed, requiring a downshift action. During such a downshift all inertia's located on the primary side of the CVT (engine, torque converter and primary pulley) need to be accelerated, which requires a significant amount of power to accomplish. In practice this means that the available (little) torque reserve is fully needed to accelerate primary sided inertia's, instead of instantly contributing to vehicle acceleration. As a result, the available power at the wheels experiences a significant time delay upon pedal depression.

This system property is known as *jet-start* or *rubber-band effect*. The driver might experience the delayed power increase as a lack of control over the vehicle.

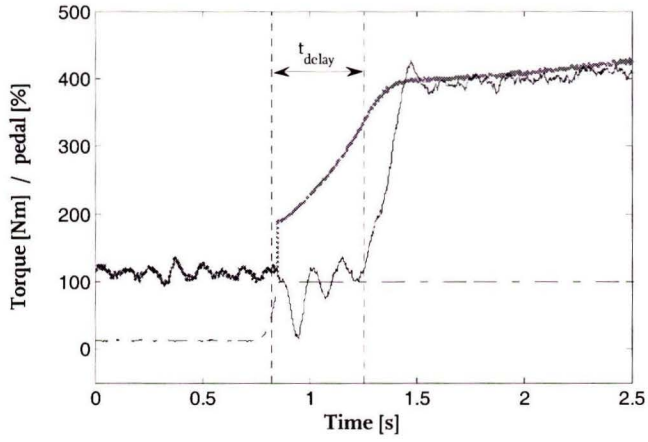

Figure 2.5: jet-start behaviour measured in the test vehicle

Figure 2.5 shows the jet-start behaviour as measured in the test vehicle. Following a kick down at 70 km/h, wheel torque starts rising after a delay of approximately half a second. Initially the torque at the wheels even drops slightly, causing vehicle acceleration to become negative for a short period of time. The upper curve represents the theoretical wheel torque in case of zero primary inertia, based on engine combustion power increase. The difference between both curves is the torque loss due to inertial effects.

2.2 IS²-CVT powertrain

In the previous paragraph, the paradox between optimal fuel economy and driveability of a conventional CVT based powertrain was elaborated. The IS²-concept counteracts the unwanted inertial phenomenon seen in a CVT by applying a mechanical flywheel assist during downshifts. Furthermore, the flywheel unit is used for kinetic energy storage during vehicle standstills, enabling an engine idle-stop functionality. Thereby the goal of the IS²-concept is twofold, namely improving driveability while at the same time reducing fuel consumption. The transition from reference powertrain to full IS²-CVT is done in three steps. These individual construction phases will be shortly addressed in this paragraph.

In the first construction phase, the torque converter is replaced by an engine flywheel and a wet plate launch clutch (see figure 2.6). The conventional drive clutch in the DNR-set is upgraded for launch purposes. This is done by increasing its diameter, number of friction surfaces and cooling capacity. By eliminating the rather large torque converter from the bellhouse, much needed space becomes available. Furthermore, an improvement in fuel economy is expected because engine speeds during launch can be reduced considerably. The steel pushbelt in the variator is replaced by a *GCI involute chain* [9]. By using the new

involute chain technology, mechanical losses in the variator are reduced, contributing to improved overall fuel economy.

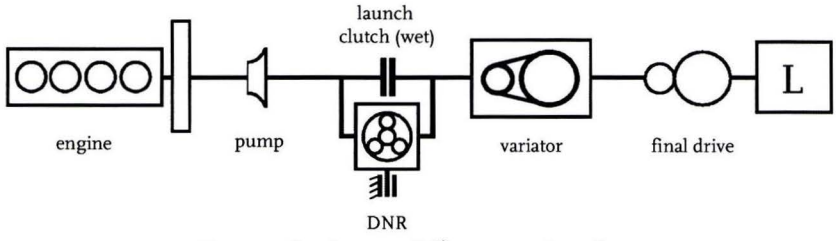

Figure 2.6: layout of 1st construction phase

During the second construction phase, the IS²-module is placed in the space now available in the bellhouse. It consists a planetary gear set, the steel IS²-flywheel and a reduction gear. When displayed schematically, these new components form a parallel branch over the variator and the launch clutch, see figure 2.7. Although not visible in the representation below, both the planetary gear set as well as the IS²-flywheel are axially aligned with the crankshaft and primary pulley. This intermediate layout enables the Impulse Shift functionality, which is introduced in the next paragraph.

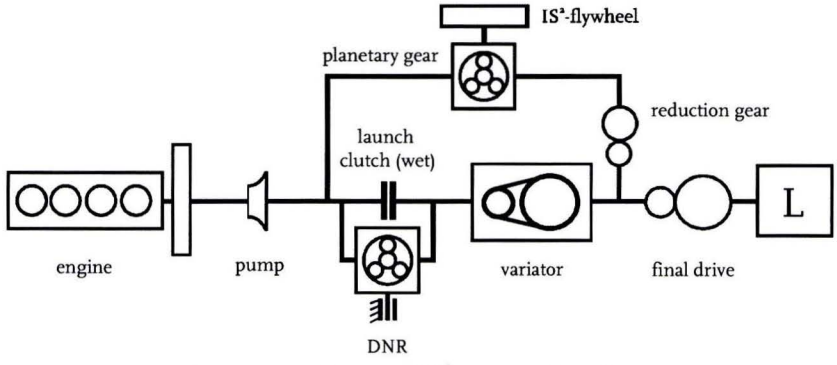

Figure 2.7: layout of 2nd construction phase

In the third and final construction phase, an additional clutch is added to the IS²-module. The hydraulically actuated (cone-)clutch is located between the planetary gear and the reduction gear, see figure 2.8. This so-called impulse start clutch adds a degree of freedom to the drivetrain, making it possible to let the IS²-flywheel rotate in freewheeling mode. This ability is necessary to enable the Impulse Start functionality, which is introduced in the next paragraph. For demonstration purposes, the impulse start clutch can also be opened during normal driving. By doing so, the conventional and improved acceleration responses can be demonstrated during a single test drive. Construction drawings of all three layouts mentioned above, as well as the layout of the reference CVT, are presented in appendix J.

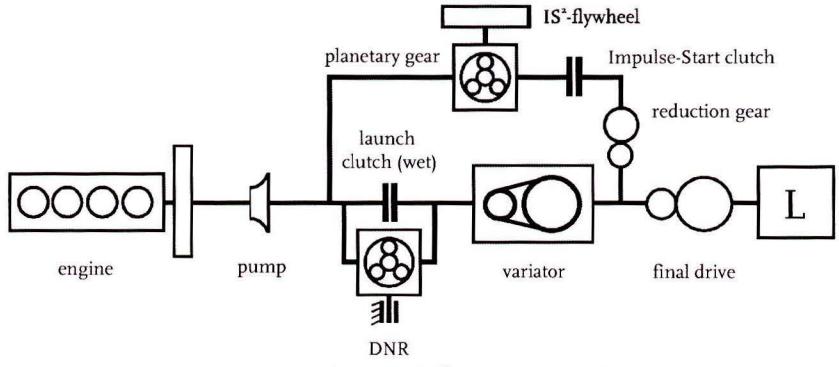

Figure 2.8: layout of 3rd construction phase

2.2.1 Impulse Shift functionality

The Impulse Shift functionality is meant to eliminate the rubber-band effect seen in conventional CVT equipped powertrains. As mentioned earlier, the combination of little torque reserve and large primary inertia's results in a delayed acceleration response when performing a downshift. In [2, 10, 11] a solution for this paradox is presented in the form of an additional flywheel inertia whose kinetic energy level decreases during downshift transients, creating a purely mechanical assist.

This is realised by adding a planetary gear set in combination with a steel flywheel in parallel with the variator. A planetary gear set consists of three rotational members, being the sun gear, planet carrier and annulus (or ring) gear. A schematic drawing of a basic planetary gear is shown in figure 2.9.

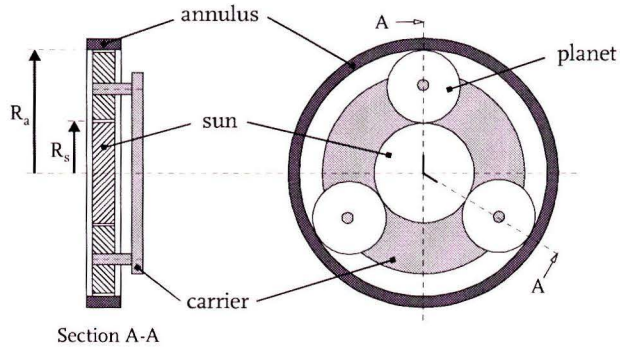

Figure 2.9: planetary gear set

A planetary gear set prescribes a linear relation between the speeds of its three members, depending on the characteristic planetary gear ratio '*z*'. In the IS²-concept the sun gear is connected to the IS²-flywheel and the engine is connected to the annulus. In case of a closed impulse start clutch, the planet carrier is connected to the secondary drivetrain causing its speed to be proportional with vehicle speed.

During steady-state driving situations, the engine is operated fuel efficient along the E-line, at low speed and high torque. In practice this corresponds to early upshifting, causing overdrive ratio to be reached fairly soon. The speed relation of the planetary gear is chosen in such a way that IS²-flywheel speed is high at these high CVT ratios. This can be displayed graphically by means of the nomogram in figure 2.10.

The grey line represents the speed relation of the planetary gear during steady-state driving at 80 km/h. With the variator controlled in overdrive, engine speed is approximately 1800 rpm and flywheel speed is close to 5000 rpm. If a large power increase is demanded by the driver, a downshift towards medium ratio is performed causing engine speed to increase and flywheel speed to decrease. In the nomogram this action causes the grey line to pivot clockwise around the virtually constant vehicle speed, as is indicated by both arrows. At the end of this downshift, engine speed has increased to 4000 rpm and the flywheel is almost at a standstill (black line). Because its kinetic energy level decreases during this downshift, the IS²-flywheel temporarily acts as an additional power source. This purely mechanical assist compensates for the lack of torque reserve, thereby preventing the unwanted jet-start phenomenon seen in conventional CVT powertrains.

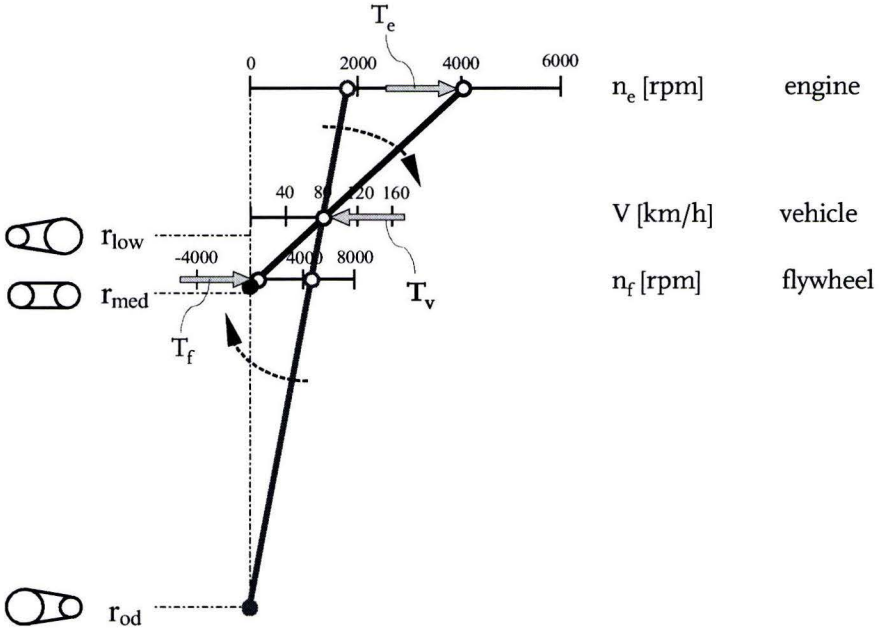

Figure 2.10: nomogram of a downshift at 80 km/h

In contrast to the Zero Inertia powertrain presented in [2, 10, 11], the annulus connection of the IS²-CVT is located on the engine side of the launch clutch (see figure 2.8). This means that when performing a fast downshift, the drive clutch may be temporarily opened. All torque will than instantly travel via the planetary gear set through the parallel transmission path. Whether this is necessary depends on achievable variator shift-speed and initial response time, as will become clear in later chapters.

2.2.2 Impulse Start functionality

The second feature of the IS²-module is an engine *idle-stop* functionality. Idle-stop refers to the capability to shutdown the combustion engine at vehicle standstill, and restart quickly when needed. This enables the elimination of idle fuel consumption. The impulse start clutch, located on the carrier-branch of the parallel path, enables the IS²-flywheel to freewheel during vehicle standstill. When the driver releases the brake pedal, the impulse start clutch is closed and kinetic energy stored in the IS²-flywheel is used to rapidly restart the combustion engine.

The Impulse Start sequence is depicted in figure 2.11 by means of four nomograms. In figure 2.11(a) the vehicle comes to a halt after opening the drive clutch at approximately 8 km/h. At standstill, the speed relation of the planetary gear set reduces to:

$$\omega_{sun} = -z\omega_{annulus} \qquad \text{or} \qquad \omega_{flywheel} = -z\omega_{engine} \tag{2.1}$$

Flywheel speed is proportional with engine speed, but opposite in direction. By controlling engine speed, the amount of kinetic energy in the flywheel can be regulated. After a certain delay, the impulse start clutch is opened and the engine is shut down, as seen in figure 2.11(b). The IS²-flywheel now freewheels for as long as the driver presses the brake pedal. During this waiting period, various frictional losses will cause flywheel speed to decrease steadily, as seen in figure 2.11(c). When the driver releases the brake pedal the impulse start clutch is closed rapidly, decelerating the IS²-flywheel and accelerating the engine towards its idle speed level, figure 2.11(d). While approaching idle speed, combustion is re-initiated and the engine can accelerate further under its own power.

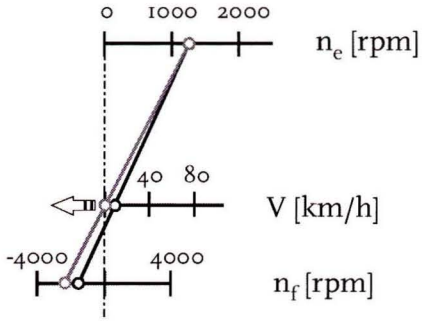

a) drive clutch opens and vehicle stops

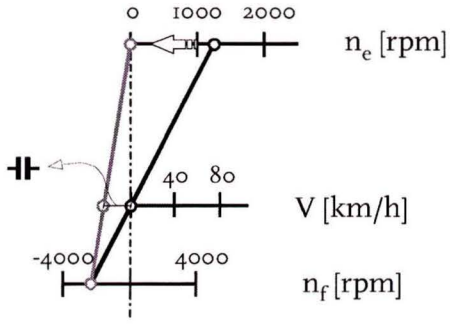

b) IS-clutch opens before engine shutdown

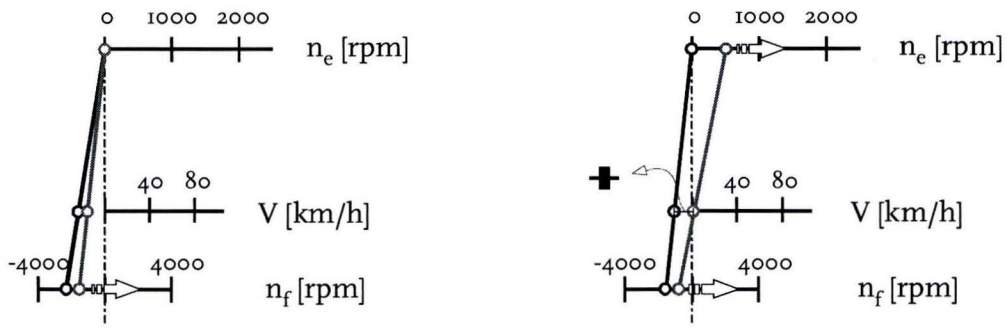

c) freewheeling IS²-flywheel

d) IS-clutch closes when brake pedal is released

Figure 2.11: nomograms of Impulse Start sequence

Target starting times, defined as the time needed to reach idle speed, are in the order of 150 ms. The impulse start clutch is designed to transmit high torque levels during synchronisation. Furthermore, drag losses present in the open clutch need to be low, maximizing the idle-stop period. These requirements have led to a hydraulically actuated cone-shaped clutch. A more detailed analysis of the Impulse Start functionality is presented in Chapter 5.

2.3 Prototype and test vehicle

The Aisin AW CVT is chosen as the donor transmission for the IS²-concept. This transmission is being manufactured for use in the Toyota Vitz (Yaris on the European market). It is a conventional V-pulley type CVT. The variator has a ratio coverage of 5.6 and originally contains a steel pushbelt manufactured by *Van Doorne's Transmissie*. A side view of the Aisin AW CVT can be seen in figure 2.12.

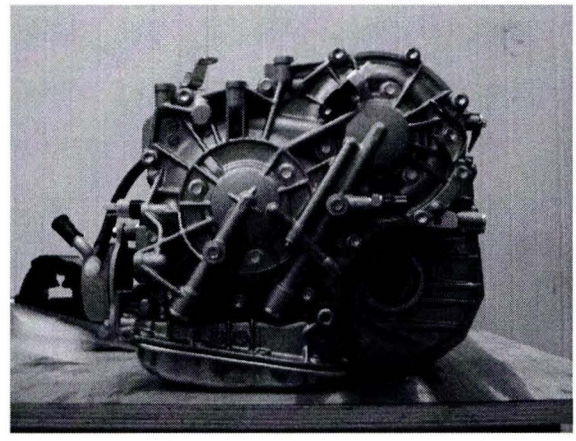

Figure 2.12: Aisin AW CVT donor transmission

Initial testing of each construction phase is carried out on a test stand (figure 2.13), on which the transmission is driven by an electric machine. Once new components and control strategies function correctly, the transmission is transferred to the test vehicle.

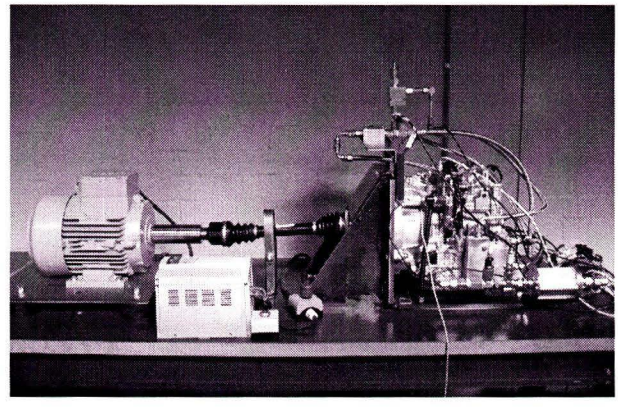

Figure 2.13: IS²-CVT mounted on the test stand

The Toyota Vitz test vehicle (figure 2.13) is a subcompact B-segment passenger car. It is powered by a 4-cylinder, 1.3L gasoline engine. Data acquisition and control in the test vehicle is realised by a *dSpace* system which runs on software created in *MatLab/Simulink/Stateflow*.

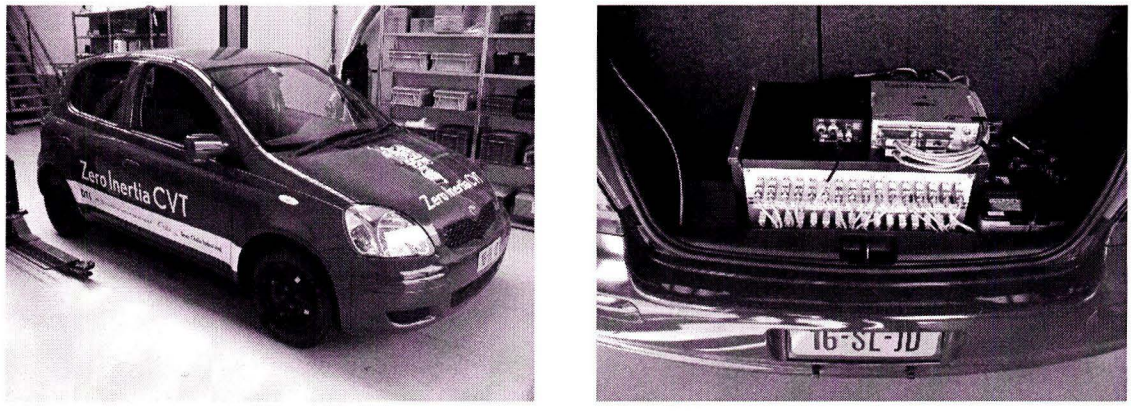

Figure 2.14: Toyota Vitz test vehicle with dSpace acquisition and control system

Chapter 3

Dynamic modelling

Before considering the main functionalities of the IS²-CVT drivetrain, a torsional compliance powertrain model is constructed. In this chapter the modelling method is described. First, the layout and component models of the drivetrain without IS²-module are considered. Next, the dynamic model of the full IS²-CVT drivetrain is treated.

3.1 Drivetrain without IS²-module

A schematic representation of the drivetrain without IS²-module, corresponding to the first construction phase, is displayed in figure 3.1 It contains an engine inertia, which is the combined inertia of the crankshaft, connecting rods, pistons, camshafts, pump and engine flywheel. Behind the engine a torsion damper, modelled as a spring-damper, provides the necessary vibration reduction. The drive clutch in the drive/neutral/reverse (DNR) unit connects the torsion damper to the primary pulley via the primary input shaft. The variator contains both pulley inertia's and the pushbelt or involute chain in between. A final drive gear stage and flexible drive shafts form the connection towards the wheels. No differential gear is modelled, since only straight line driving is of interest. A non-linear damper is used to model the traction forces between tires and road. Finally, the vehicle body mass is represented by its rotational form.

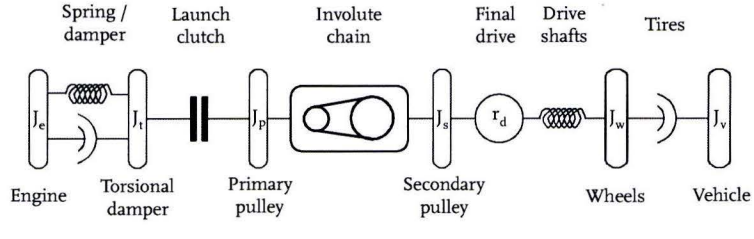

Figure 3.1: first construction phase drivetrain

A number of assumptions are made to simplify the dynamic model. First of all, the variator is assumed to be free of slip. Mechanical losses in the variator are modelled by means of a

friction torque acting on the secondary pulley. Furthermore, the drivetrain is assumed to be free of backlash. Spring elements (torsion damper and drive shafts) are assumed to be fully linear. Gears are assumed to be mass-less and free of losses. Both drive shafts have been lumped into a single spring, representing a combined stiffness. The same has been done for both tires. Along these assumptions the free-body diagram of figure 3.2 can be constructed.

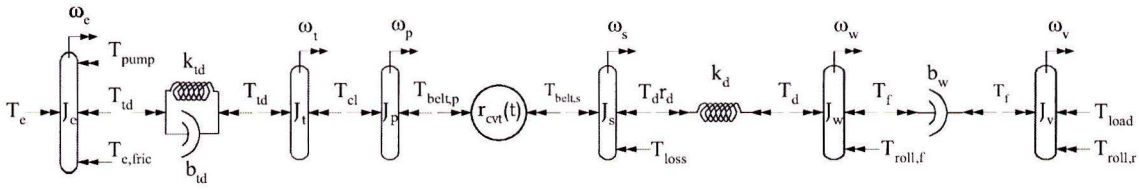

Figure 3.2: first construction phase, free-body diagram

The differential equations corresponding to the free-body diagram of figure 3.2 are presented in appendix B. In the remainder of this chapter the dynamics of the full IS²-CVT will be considered.

3.2 Drivetrain with IS²-module

All components creating the parallel transmission branch are joined in a single module. It contains a planetary gear set, steel flywheel, impulse start clutch and a connection gear stage, see figure 3.3.

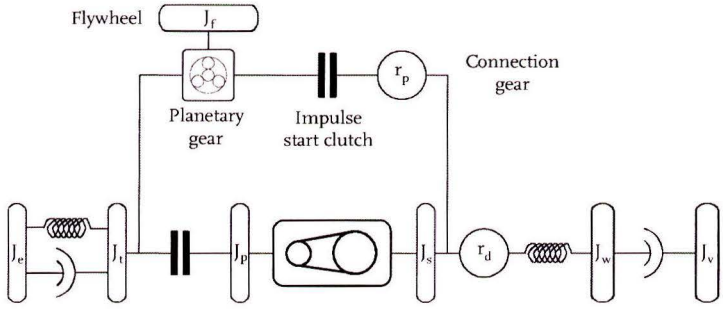

Figure 3.3: IS²-CVT drivetrain

The planetary gear set (figure 2.9) prescribes a linear relation between the speeds of its three rotating members, being the annulus, carrier and sun gear [3]:

$$\omega_{sun} = (z+1)\omega_{carrier} - z\omega_{annulus} \qquad \text{where :} \qquad z = \frac{R_a}{R_s} \tag{3.1}$$

The torque relations between the members of the planetary gear are given by:

$$T_{annulus} = zT_{sun} \qquad T_{carrier} = (z+1)T_{sun} \tag{3.2}$$

In figure 3.3 the flywheel is connected directly to the sun gear of the planetary, the annulus is connected to the primary input shaft (between torsion damper and launch clutch) and the carrier is connected to the impulse start clutch. In case of a synchronized impulse start clutch the linear speed relation can be written as:

$$\omega_f = \frac{z+1}{r_p}\omega_s - z\omega_t \qquad \text{where:} \qquad z = \frac{71}{37}\ ,\ r_p = \frac{40}{28} \tag{3.3}$$

When looking at (3.3) it can be seen that in case of a synchronized impulse start clutch flywheel speed is zero when:

$$z\,\omega_t = \frac{z+1}{r_p}\omega_s \tag{3.4}$$

For a closed launch clutch this corresponds to:

$$r_{cvt} = r_{gn} = \frac{zr_p}{z+1} \tag{3.5}$$

This particular CVT ratio, where flywheel speed is zero, is named *geared-neutral* ratio. For the chosen parameters, geared-neutral ratio lies close to medium (r_{gn} = 0.94). Below this ratio flywheel speed is negative and above this ratio flywheel speed is positive.

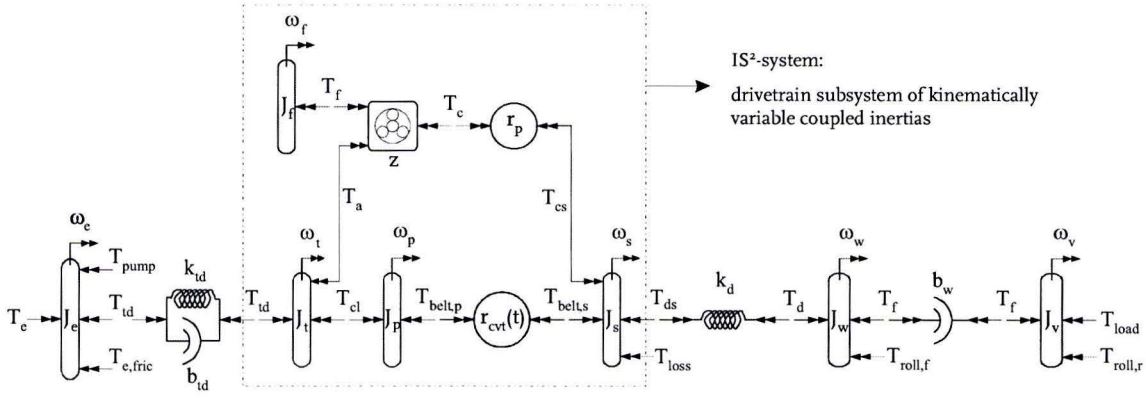

Figure 3.4: full IS²-CVT drivetrain, free-body diagram

The free-body diagram of the full IS²-CVT drivetrain is displayed in figure 3.4. The core of the transmission, between the torsion damper and drive shafts, contains four inertia's,

being J_t, J_p, J_f, and J_s (see figure 3.5). When both clutches are closed and the CVT ratio is given, there is only one degree of freedom in this part of the drivetrain. Since there are four differential equations, one for each inertia, the system is clearly over-determined. As this will cause algebraic loops in a simulation environment, a solution needs to be found. It was decided to lump the flywheel and primary pulley inertia to the torsion damper and secondary pulley positions, reducing the number of equations to two. By using a *Karnopp* expression [4] for the sticking drive clutch these two degrees of freedom can be retained without causing numerical difficulties. The lumping process of flywheel and primary pulley inertia is described next.

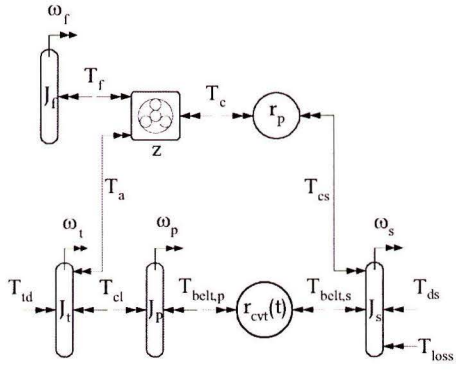

Figure 3.5: IS² system, free-body diagram

Both velocity as well as acceleration of all three members of the planetary gear are related according to:

$$\omega_f = \frac{z+1}{r_p}\omega_s - z\omega_t \qquad \dot{\omega}_f = \frac{z+1}{r_p}\dot{\omega}_s - z\dot{\omega}_t \tag{3.6}$$

Furthermore, the torques acting on its members are related according to:

$$T_a = zT_f \qquad T_c = (z+1)T_f \tag{3.7}$$

$$T_f = -J_f\dot{\omega}_f \qquad \text{where:} \qquad J_f = 0.082 \quad [kgm^2] \tag{3.8}$$

The torque stemming from the IS²-flywheel can be mapped to the torsion damper and secondary pulley positions by writing:

$$T_a = zT_f = J_f z^2\dot{\omega}_t - J_f\frac{z^2+z}{r_p}\dot{\omega}_s \tag{3.9}$$

$$T_{cs} = \frac{z+1}{r_p}T_f = J_f\frac{z^2+z}{r_p}\dot{\omega}_t - J_f\left(\frac{z+1}{r_p}\right)^2\dot{\omega}_s \qquad \text{with:} \quad T_{cs} = \frac{T_c}{r_p} \tag{3.10}$$

On the torsion damper position, the lumped dynamics now correspond to:

$$J_t\dot{\omega}_t = T_{td} - T_{cl} - T_a \tag{3.11}$$

$$J_t\dot{\omega}_t = T_{td} - T_{cl} - J_f z^2\dot{\omega}_t + J_f\frac{z^2+z}{r_p}\dot{\omega}_s \tag{3.12}$$

$$J_t^*\dot{\omega}_t = T_{td} - T_{cl} + J_f\frac{z^2+z}{r_p}\dot{\omega}_s \qquad \text{with:} \quad J_t^* = J_t + J_f z^2 \tag{3.13}$$

The primary pulley torques can be mapped to the secondary pulley position:

$$T_{belt,p} = T_{cl} - J_p\dot{\omega}_p \qquad \text{where:} \qquad \dot{\omega}_p = \frac{\dot{\omega}_s}{r_{cvt}} - \frac{\omega_s\dot{r}_{cvt}}{r_{cvt}^2} \tag{3.14}$$

$$T_{belt,s} = \frac{T_{belt,p}}{r_{cvt}} = \frac{T_{cl} - J_p\dot{\omega}_p}{r_{cvt}} = \frac{T_{cl}}{r_{cvt}} - J_p\left(\frac{\dot{\omega}_s}{r_{cvt}^2} - \frac{\omega_s\dot{r}_{cvt}}{r_{cvt}^3}\right) \tag{3.15}$$

On the secondary pulley position, the lumped dynamics now correspond to:

$$J_s\dot{\omega}_s = T_{belt,s} - T_{ds} - T_{loss} + T_{cs} \qquad \text{with:} \quad T_{ds} = r_d T_d \tag{3.16}$$

$$J_s\dot{\omega}_s = \frac{T_{cl}}{r_{cvt}} - \frac{J_p}{r_{cvt}^2}\dot{\omega}_s + \frac{J_p\omega_s}{r_{cvt}^3}\dot{r}_{cvt} - T_{ds} - T_{loss} + J_f\frac{z^2+z}{r_p}\dot{\omega}_t - J_f\left(\frac{z+1}{r_p}\right)^2\dot{\omega}_s \tag{3.17}$$

$$J_s^*\dot{\omega}_s = \frac{T_{cl}}{r_{cvt}} + T_{shift,s} - T_{ds} - T_{loss} + J_f\frac{z^2+z}{r_p}\dot{\omega}_t \tag{3.18}$$

$$\text{with:} \quad J_s^* = J_s + \frac{J_p}{r_{cvt}^2} + J_f\left(\frac{z+1}{r_p}\right)^2 \quad , \quad T_{shift,s} = \frac{J_p\omega_s}{r_{cvt}^3}\dot{r}_{cvt}$$

Two interrelated differential equations have now been found for the torsion damper and secondary pulley accelerations, namely (3.13) and (3.18). By inserting torsion damper acceleration of (3.13) into (3.18), a decoupled differential equation for the equivalent secondary pulley inertia can be found:

$$J_s^*\dot{\omega}_s = \frac{T_{cl}}{r_{cvt}} + T_{shift,s} - T_{ds} - T_{loss} + J_f\frac{z^2+z}{r_p}\frac{T_{td} - T_{cl} + J_f\dfrac{z^2+z}{r_p}\dot{\omega}_s}{J_t^*} \tag{3.19}$$

$$J_s^{**}\dot{\omega}_s = \left(\frac{1}{r_{cvt}} - \gamma_s\right) T_{cl} + T_{shift,s} - T_{ds} - T_{loss} + \gamma_s T_{td} \tag{3.20}$$

$$J_s^{**}\dot{\omega}_s = \sigma_{cl} T_{cl} + T_{shift,s} - T_{ds} - T_{loss} + \gamma_s T_{td} \tag{3.21}$$

Where the equivalent secondary pulley inertia is given by:

$$J_s^{**} = J_s^{*} - \frac{1}{J_t^{*}}\left(J_f \frac{z^2 + z}{r_p}\right)^2 \tag{3.22}$$

The torque amplification factor from the planetary gear to the secondary pulley is defined as:

$$\gamma_s = \frac{J_f}{J_t^{*}} \frac{z^2 + z}{r_p} \tag{3.23}$$

And the drive clutch torque gain to the secondary side is given by:

$$\sigma_{cl} = \frac{1}{r_{cvt}} - \gamma_s \tag{3.24}$$

By inserting secondary pulley acceleration of (3.18) into (3.13), a decoupled differential equation for the equivalent torsion damper inertia can be found:

$$J_t^{*}\dot{\omega}_t = T_{td} - T_{cl} + J_f \frac{z^2 + z}{r_p} \frac{\frac{T_{cl}}{r_{cvt}} + T_{shift,s} - T_{ds} - T_{loss} + J_f \frac{z^2 + z}{r_p}\dot{\omega}_t}{J_s^{*}} \tag{3.25}$$

$$J_t^{**}\dot{\omega}_t = T_{td} - \left(1 - \frac{\gamma_t}{r_{cvt}}\right) T_{cl} + \gamma_t \left(T_{shift,s} - T_{ds} - T_{loss}\right) \tag{3.26}$$

$$J_t^{**}\dot{\omega}_t = T_{td} - \tau_{cl} T_{cl} + \gamma_t \left(T_{shift,s} - T_{ds} - T_{loss}\right) \tag{3.27}$$

Where the equivalent torsion damper inertia is given by:

$$J_t^{**} = J_t^{*} - \frac{1}{J_s^{*}}\left(J_f \frac{z^2 + z}{r_p}\right)^2 \tag{3.28}$$

The torque amplification factor from the planetary gear to the torsion damper is defined as:

$$\gamma_t = \frac{J_f}{J_s^{*}} \frac{z^2 + z}{r_p} \tag{3.29}$$

And the drive clutch torque gain to the primary side is given by:

$$\tau_{cl} = 1 - \frac{\gamma_t}{r_{cvt}} \tag{3.30}$$

Having found these lumped expressions, only two degrees of freedom remain as graphically depicted in figure 3.6.

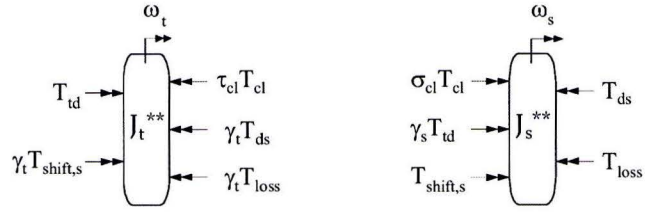

Figure 3.6: lumped dynamics of the IS² system

In case of a sticking drive clutch, a Karnopp expression for the clutch torque can be used. By doing this, both degrees of freedom can be retained without causing algebraic loop conflicts. The derivation of the Karnopp expression is presented in appendix I. The clutch torque for both states can be written as:

$$T_{cl} = \begin{cases} T_{applied} \cdot sign(\omega_t - \omega_p) & \text{for a slipping clutch, in case: } |\omega_t - \omega_p| > \varepsilon \\ T_{Karnopp} & \text{for a sticking clutch, in case: } |\omega_t - \omega_p| \le \varepsilon \quad \wedge \quad T_{Karnopp} < T_{applied} \end{cases}$$

The final differential equation for the lumped secondary pulley inertia, in case of a sticking clutch (Zero Inertia mode), now becomes:

$$J_s^{**}\dot{\omega}_s = \sigma_{cl}\left(\frac{-J_t^{**}\left(T_{shift,s} - T_{ds} - T_{loss} + \gamma_s T_{td} - T_{shift,p}^{*}\right) + J_s^{**} r_{cvt}\left\{T_{td} + \gamma_t\left(T_{shift,s} - T_{ds} - T_{loss}\right)\right\}}{J_t^{**}\sigma_{cl} + J_s^{**} r_{cvt}\tau_{cl}}\right) + T_{shift,s} - T_{ds} - T_{loss} + \gamma_s T_{td} \tag{3.31}$$

And in case of an open or slipping clutch (Impulse Shift mode):

$$J_s^{**}\dot{\omega}_s = \sigma_{cl}T_{cl} + T_{shift,s} - T_{ds} - T_{loss} + \gamma_s T_{td} \tag{3.32}$$

By inserting $J_f = 0$ into the equations derived above, the dynamics of the drivetrain without IS²-module remain, which corresponds to the standard CVT. The differential equations of the engine, wheel and vehicle inertia's are no different than for the drivetrain of paragraph 3.1. This is also true for the equations describing the compliances (torsion damper, drive shafts and tires). These equations can be found in appendix B.

Chapter 4

Torsional vibrations analysis

To gain valuable insights regarding the torsional dynamics of the IS²-CVT a vibration analysis is performed. The IS²-flywheel is expected to have a profound influence on drivetrain torsional behaviour. Whether it has a positive effect like improved vibration reduction, or a negative effect like problematic eigenfrequencies will be analysed in the following paragraphs.

4.1 Description of operating modes

The drivetrain described in the previous chapter contains two clutches, being the launch or drive clutch and the impulse start clutch. Closing or opening either clutch changes the dynamic behaviour of the system. In total, four different combinations can be created. These so-called operating modes are displayed in figure 4.1.

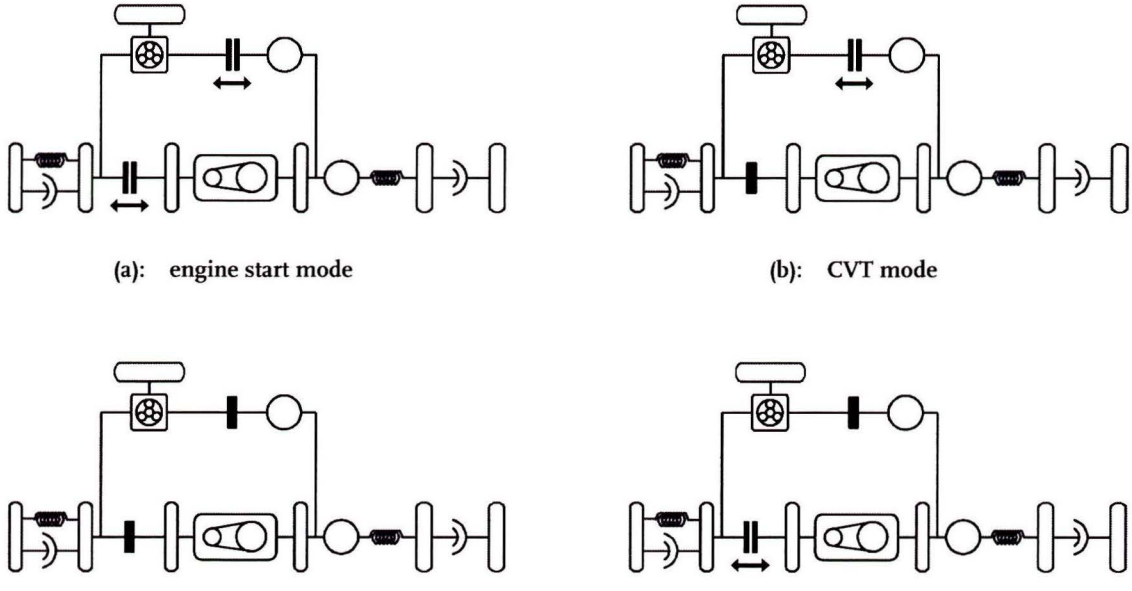

(a): engine start mode

(b): CVT mode

(c): Zero Inertia mode

(d): Impulse Shift mode

Figure 4.1 : operating modes encountered in the IS² drivetrain

During vehicle standstill and engine start or shutdown, both clutches are open. This operating mode is displayed in figure 4.1(a) and is named *engine start mode*. Note that conventional (starter motor) starting is considered in this chapter, impulse starting will be treated in Chapter 5. When driving with an open impulse start clutch the flywheel rotates freely, having no influence on drivetrain dynamics. In this case drivetrain dynamics are quite similar to those of a conventional CVT (with torque converter lock-up engaged). Therefore this operating mode is named *CVT mode*, see figure 4.1(b). When driving with both clutches closed, drivetrain dynamics are similar to that of the Zero Inertia powertrain as described in [2, 10, 11]. The *Zero Inertia mode* is displayed in figure 4.1(c). As explained earlier, temporarily opening the drive clutch during a fast downshift may be favorable. This would result in the situation of figure 4.1(d), named *Impulse Shift mode*.

In paragraph 4.2 a linear analysis of all modes encountered during drive-situations is presented, being CVT, ZI and IS mode. Paragraph 4.3 covers the linear analysis of engine start mode, which changes during the various construction phases.

4.2 Linear analysis of drive modes

For each operating mode encountered during drive situations (CVT, ZI and IS) a linear model can be constructed to investigate the torsional dynamics of the drivetrain. In appendix D.1 the linear models of these three operating modes are presented, along with the assumptions made to obtain linear drivetrain dynamics. Being the main excitation source present in the drivetrain, engine torque is chosen as input. Acceleration levels on two positions downstream have been chosen as outputs, namely torsion damper acceleration and vehicle acceleration. Besides the states of both clutches, the CVT ratio has a profound influence on torsional vibration behaviour. Therefore, the aforementioned operating modes will be compared for three different ratios, being low, geared-neutral and overdrive ratio.

For a 4-stroke engine, the frequency of the main excitation order can be expressed as:

$$f_{ex} = \frac{N_{cyl}}{2}\frac{n_e}{60} \qquad [Hz] \tag{4.1}$$

For a four cylinder engine this results in 30 Hz at 900 rpm and 200 Hz when running at 6000 rpm.

4.2.1 Low ratio

The resulting frequency responses in low ratio are shown in figure 4.2. When looking at the torsion damper acceleration in figure 4.2(a), two resonance frequencies can be recognized for all three operating modes. For very low frequencies the acceleration magnitude obeys Newton's second law of motion. In this range the IS mode magnitude lies on a higher level since it is kinematically undetermined.

The lowest eigenfrequency corresponds to the drive shaft resonance. Above this frequency the vehicle mass can no longer follow the drivetrain, hence the decay of 40 dB per decade seen in figure 4.2(b). The second eigenfrequency corresponds to the torsion damper resonance. Above this frequency the transmission is virtually decoupled from the engine. This is the case for the entire engine excitation range, indicated by the vertical lines.

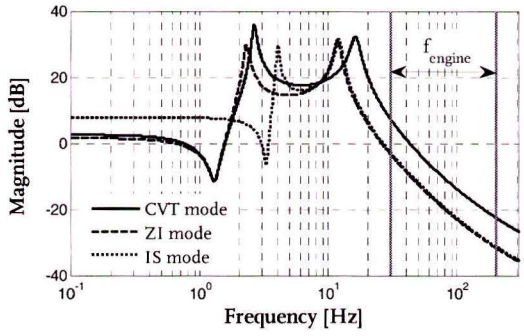

Figure 4.2(a): MRF from T_e to $\dot{\omega}_t$

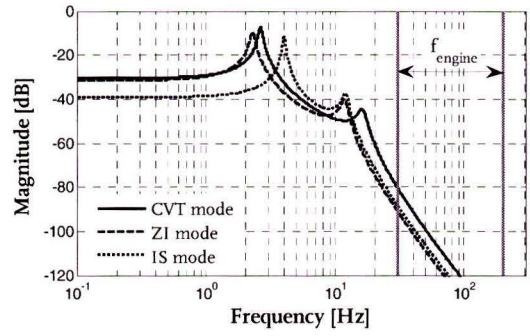

Figure 4.2(b): MRF from T_e to $\dot{v}$

Drive shaft resonance frequency is highest in IS mode (4 Hz) and lowest in ZI mode (2 Hz). It can be seen that both magnitudes are approximately 5 dB lower than seen in CVT mode. Torsion damper resonance frequency lies highest in CVT mode (17 Hz), whereas in ZI and IS mode it lies much lower (11 Hz). Since the torsion damper inertia decouples earlier in ZI and IS mode, it shows a 10 dB reduction in acceleration magnitude compared to CVT mode at higher frequencies. Apparently the additional flywheel inertia has a positive effect on vibration reduction in low ratio. It functions like a dual-mass-flywheel, reducing transmission vibration levels by increasing overall transmission inertia.

4.2.2 Geared-neutral ratio

As explained in the previous chapter, geared-neutral ratio corresponds to the CVT ratio where the flywheel is at standstill. This ratio (r_{gn} = 0.94) lies quite close to medium. When looking at the resulting frequency responses in figure 4.3, the first observation is that the curves of CVT and ZI mode are exactly the same.

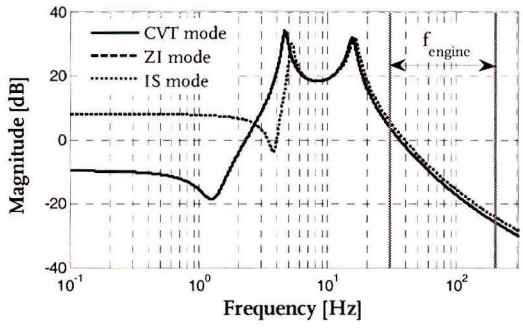

Figure 4.3(a): MRF from T_e to $\dot{\omega}_t$

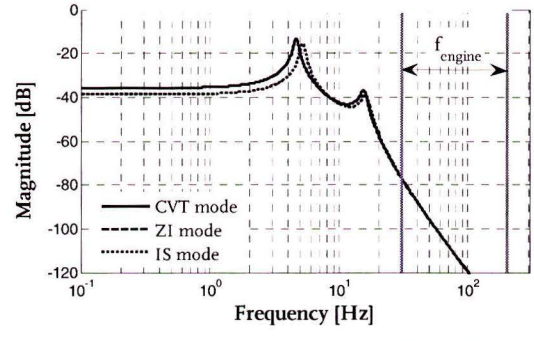

Figure 4.3(b): MRF from T_e to $\dot{v}$

This is not surprising since the flywheel speed is zero than and does not contribute any drivetrain inertia with respect to the standard CVT. The improvements in vibration reduction seen in low ratio for ZI and IS mode are no longer present in geared-neutral ratio. Drive shaft resonance frequency in CVT and ZI mode has increased to 4.5 Hz.

4.2.3 Overdrive ratio

In overdrive ratio the dual-mass-flywheel properties of the IS²-flywheel in ZI mode are present again, as can be seen in figure 4.4. The IS²-flywheel lowers both the frequency as well as the magnitude of both resonances in ZI mode. The drive shaft resonance is now found at 5.5 Hz for ZI mode and 7 Hz for CVT mode, with a 10 dB difference in magnitude. Torsion damper resonance lies at 9 Hz in ZI mode and 13 Hz in ZI mode, with a 5 dB difference in magnitude.

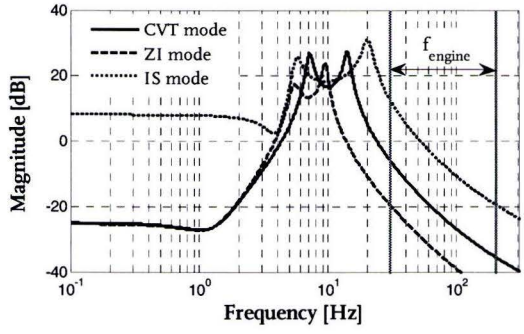

Figure 4.4(a): MRF from T_e to $\dot{\omega}_t$

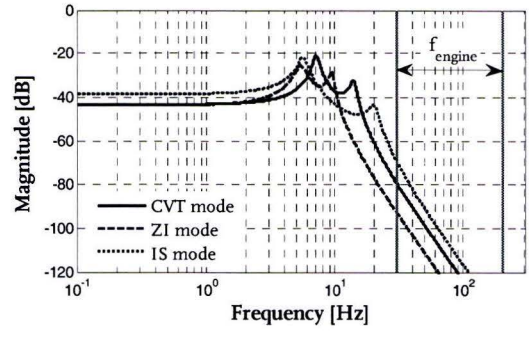

Figure 4.4(b): MRF from T_e to $\dot{v}$

Since the combustion machine is operated on the E-line in most drive situations, a large percentage of time will be spent near overdrive. The additional vibration reduction introduced by the IS²-flywheel is most effective here, since vibration levels are usually worst at low engine speeds in combination with high torque levels.

4.3 Linear analysis of engine start mode

In the previous paragraph the torsional dynamics of all drive modes were considered, without considering engine start mode. As was already addressed in paragraph 2.2, the transformation from conventional to IS²-CVT takes place in three construction phases, see figure 4.5.

During the first and third construction phases, engine and torsion damper are fully disconnected from the remaining drivetrain during conventional (starter motor) engine starts. This leads to a situation no different than in the reference drivetrain. During the second construction phase the absence of the impulse start clutch leads to a very different situation however. Via the parallel transmission branch, engine and torsion damper are

connected to both the IS²-flywheel as well as the secondary side of the drivetrain. This results not only in unwanted reaction torque at the wheels during engine starts, but also introduces a problematic eigenfrequency similar to that seen in dual-mass flywheel applications [7].

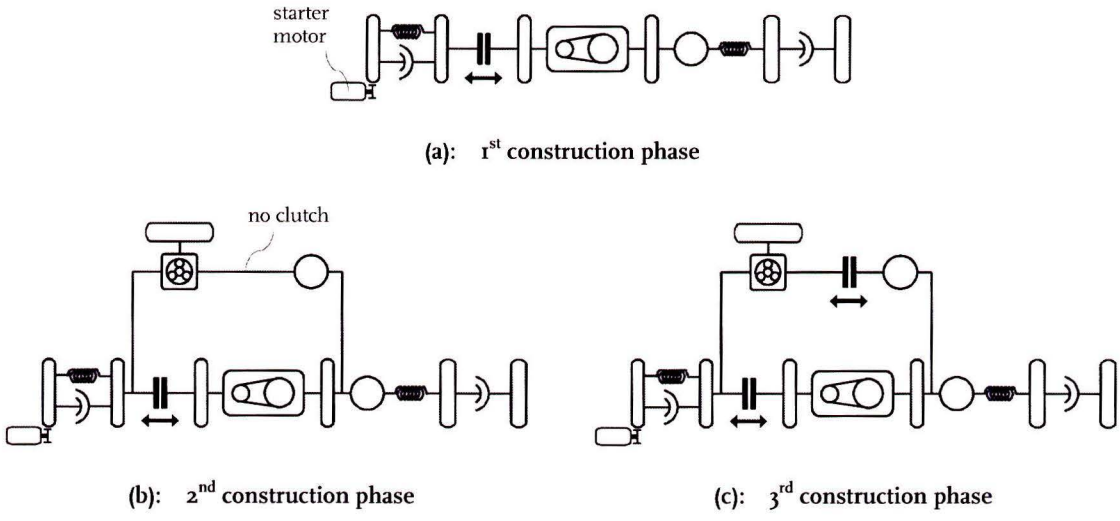

(a): 1st construction phase

(b): 2nd construction phase

(c): 3rd construction phase

Figure 4.5: schematic overview of different construction phases

By constructing linear models of the three drivetrains, engine start dynamics can be compared in the frequency domain. These linear models can be found in appendix D.2 along with a linear model of a simple dual-mass flywheel representation. In figure 4.6(a) the resulting frequency responses are displayed.

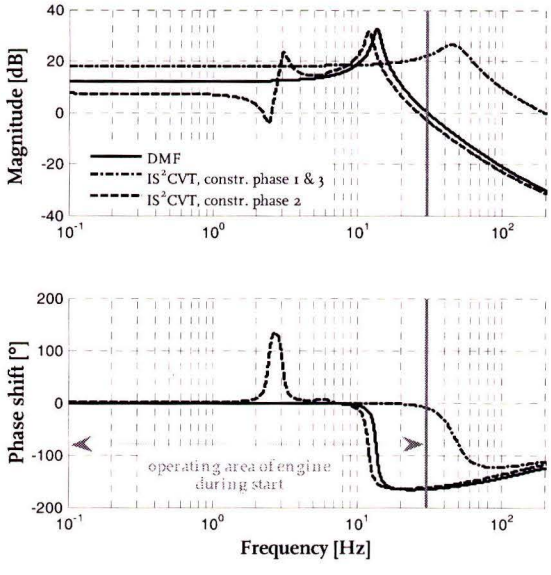

Figure 4.6(a): frequency response from T_e to $\dot{\omega}_t$

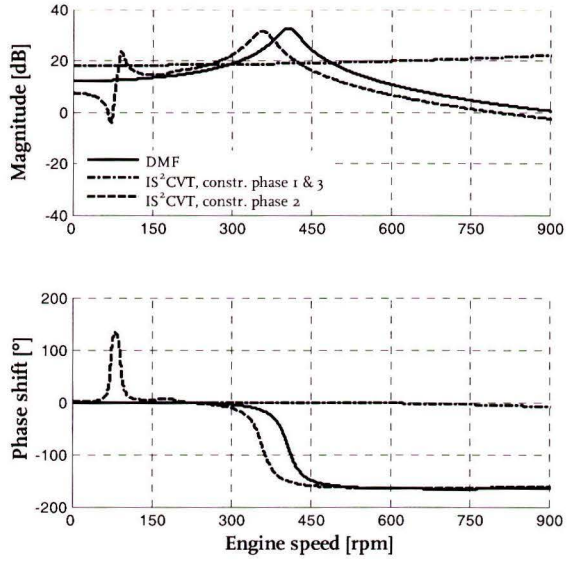

Figure 4.6(b): responses expressed as a function of engine operating speeds during start

During engine start the frequency range up to 30 Hz (900 rpm) is of interest. In this range no resonance is seen during the first and third construction phases, as expected. The curve corresponding to the second construction phase shows two resonances below 30 Hz, being a drive shaft resonance at 3 Hz and a torsion damper resonance at 11 Hz. During engine start both resonances will be encountered. This is clarified by means of figure 4.6(b) in which the frequency range of interest is expressed as a function of engine operating speed, using equation (4.1). Especially the torsion damper resonance is problematic, since it very much resembles the start dynamics of a dual mass-flywheel (DMF). Long arc springs present in a DMF can absorb the large relative angles that occur when crossing the resonance peak. The (standard) torsion damper in the test vehicle is not designed for such large relative angles, therefore mechanical failure may occur if no countermeasures are taken.

4.4 Time domain analysis of engine start resonance

A model of the second construction phase drivetrain is set up in *Simulink* to investigate the foreseen starting problems in the time domain. For this particular case a starter motor has been added to the drivetrain model. The engine model as described in appendix C has been calibrated to match measurements done in the test vehicle, as seen in figure 4.7(a).

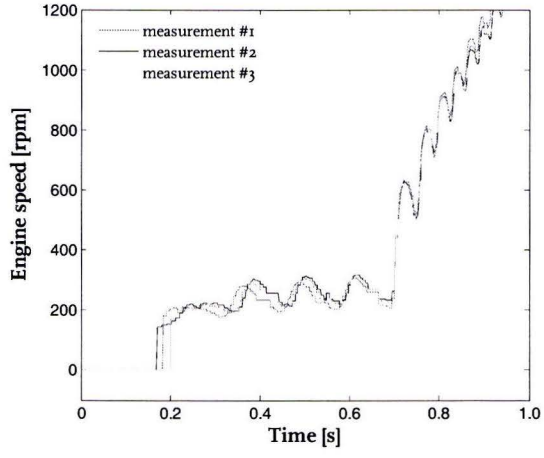

Figure 4.7(a): engine start measurements

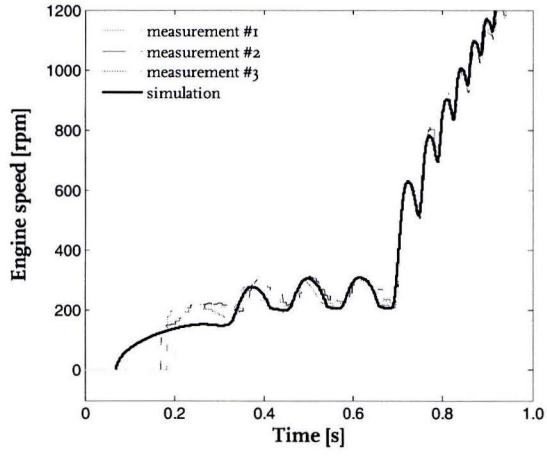

Figure 4.7(b) engine start reconstruction

By tuning the average torque output of the first ten power strokes, the engine speed profile can be reconstructed in simulation, see figure 4.7(b). The average torque values obtained from this reconstruction can now be used as an input for simulating a 2nd construction phase engine start. The results of this simulation are displayed in figure 4.8.

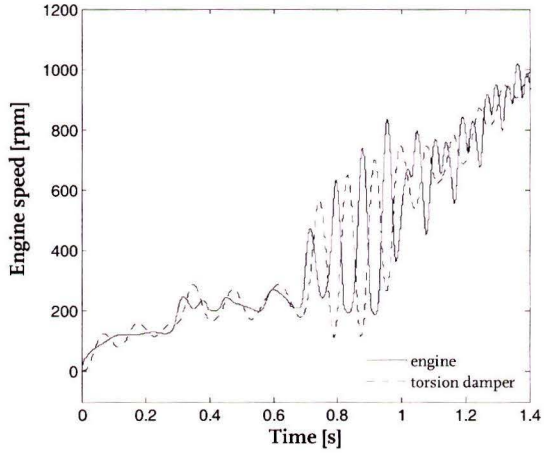

Figure 4.8(a): 2nd constr. phase start simulation

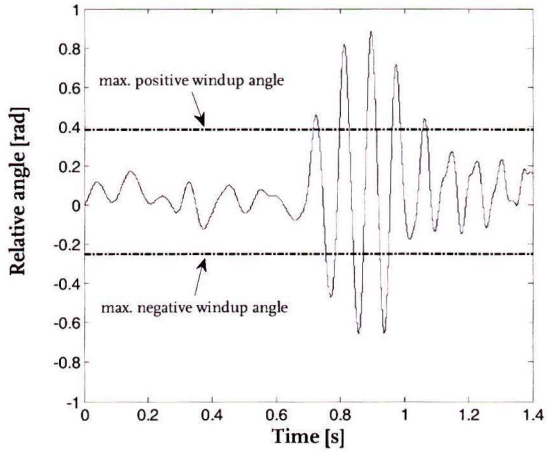

Figure 4.8(b): torsion damper relative angle

The 11 Hz resonance frequency can be clearly recognized, resulting in very large torsion damper angles. In this simulation the torsion damper windup angle was not restricted. In practice the windup angle is limited to the values indicated with the dotted lines in figure 4.8(b). In a dual-mass flywheel, long arc springs are able to absorb these large relative angles.

To prevent mechanical damage to the torsion damper, a temporary solution in the form of friction elements is considered. The amount of dry friction needed to prevent the torsion damper from reaching its end-stops is estimated based on simulation results.

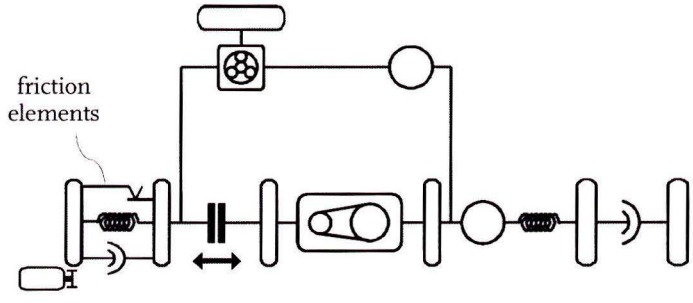

Figure 4.9: friction elements added to torsion damper

Figure 4.10 shows the simulation results when adding 40 Nm of dry friction to the torsion damper. This is enough to prevent the torsion damper to reach its end-stops, as is seen in figure 4.10(b). Off course, the vibration isolating properties of the torsion damper are heavily compromised with this amount of added friction. However, this is deemed acceptable since it is only a temporary solution needed for this particular construction phase.

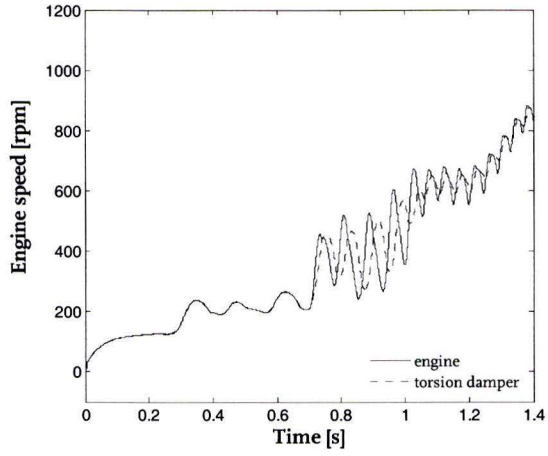

Figure 4.10(a): simulation of friction solution

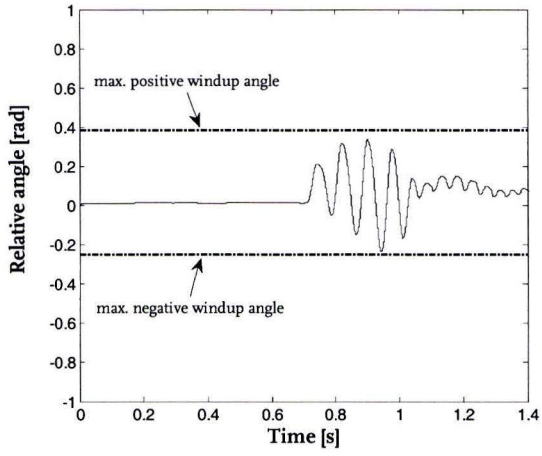

Figure 4.10(b): torsion damper relative angle

After adding six adjustable friction elements between the engine flywheel and the torsion damper, a successful engine start has been carried out. The measured start is displayed in figure 4.11.

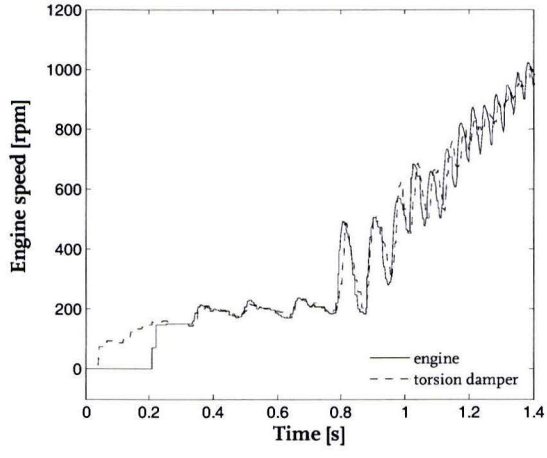

Figure 4.11(a): measurement of engine start

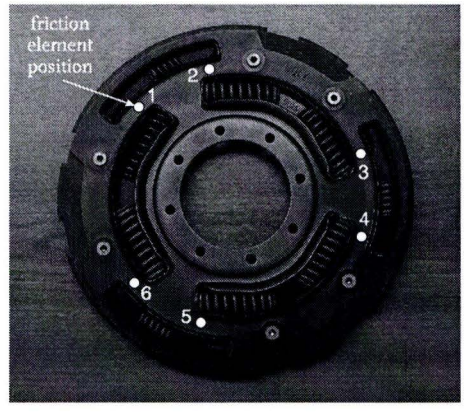

Figure 4.11(b): engine side of torsion damper with indicated friction element positions

Chapter 5

Impulse Start functionality

In this chapter an analysis of the Impulse Start functionality of the IS²-CVT is presented. The Impulse Start system is a purely mechanical idle-stop system able to restart the combustion engine after a shutdown period at vehicle standstill. A significant improvement in fuel economy can be achieved with idle-stop capabilities, especially during city driving. The goal is to enable an engine start fast enough to be virtually unnoticeable for the driver. Furthermore, the level of vibrations felt by the driver should be as low as possible.

5.1 Theory

Kinetic energy stored in the IS²-flywheel can be used as an energy buffer during engine shut down periods. The impulse start clutch located on the parallel transmission path allows the carrier of the planetary gear to rotate freely. Opening this clutch when the flywheel is at a high state of charge will cause it to freewheel. If the engine is subsequently shut down, a speed difference over the impulse start clutch will result. After the driver releases the brake pedal, the engine can be re-started by rapidly closing the impulse start clutch. Rewriting of equation (3.7) yields that the torque acting on the torsion damper relates to impulse start clutch torque according to:

$$T_a = \frac{z}{z+1} T_{iscl} \tag{5.1}$$

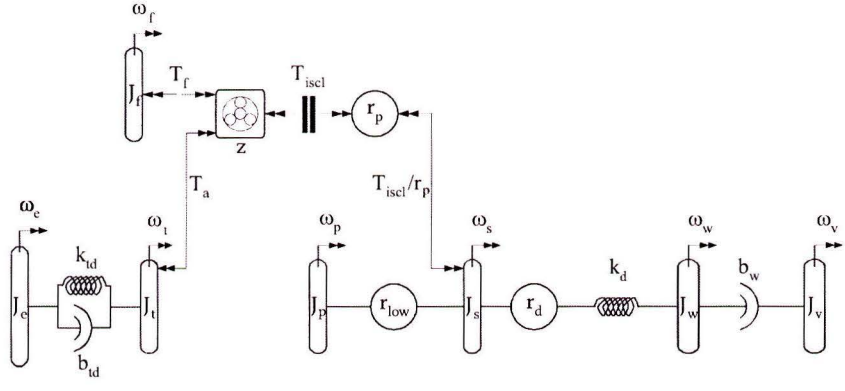

Figure 5.1: reaction torques when closing the impulse start clutch

For the torque generated by the impulse start clutch to have the correct sign, the speed difference over the clutch must be such that:

$$sign\left(\omega_{car} - \frac{\omega_s}{r_p}\right) = -1 \tag{5.2}$$

Since $\omega_s = 0$ at vehicle standstill, the carrier speed ω_{car} must be negative after the engine is shut down. This is only the case when the IS²-flywheel is released in its negative speed range, as for a stopped engine and open impulse start clutch carrier speed corresponds to:

$$\omega_{car} = \frac{\omega_f}{z+1} \tag{5.3}$$

Three situations during an Impulse Start sequence can be visualized by means of a nomogram, see figure 5.2. Line (1) represents initial situation, where the vehicle has just reached a standstill and the impulse start clutch is being opened. The line (2) represents the standby situation where the engine is shut down and the impulse start clutch remains open. Here, the flywheel is freewheeling in its negative speed range, ensuring the correct slip sign over the clutch. When the impulse start clutch is actuated, reaction torques occur on the flywheel and torsion damper. As a result, the flywheel decelerates and the engine is accelerated towards its idle speed (600 rpm). The final situation is represented by line (3). For an Impulse Start to be successful, the engine needs to be accelerated close to idle speed or higher. It is obvious that a higher flywheel state of charge will enable a higher engine speed to be reached.

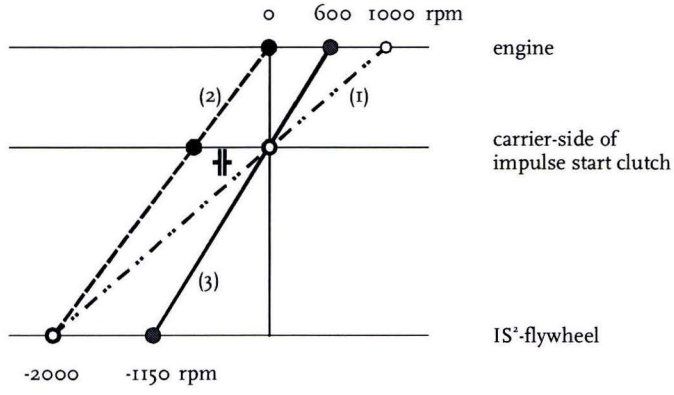

Figure 5.2: nomogram of an Impulse Start sequence

Considering all compliances in the drivetrain to be rigid, flywheel speed can be expressed as a function of vehicle speed and engine speed in case of a closed impulse start clutch:

$$\omega_f = \left(\frac{z+1}{r_p r_d R_w}\right) v_v - z\omega_e \tag{5.4}$$

The contour plot in figure 5.3 shows flywheel speed values for the entire vehicle operating range (except driving in reverse). Furthermore, the curves corresponding to low and overdrive ratio are displayed.

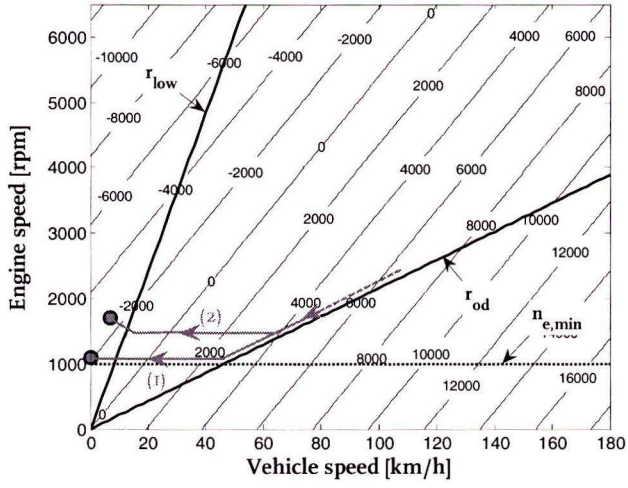

Figure 5.3: Flywheel speed [rpm] for full vehicle operating range

The goal is to release the flywheel at a large negative speed during a vehicle deceleration towards standstill. It can be seen that for a closed launch clutch, high engine speeds in low ratio are required to achieve large negative flywheel speeds. In the area where the launch clutch is opened, left of the low ratio boundary, only moderate engine speeds are needed. In fact the required engine speed is lowest when the vehicle has just reached a standstill. For example, the flywheel speed is close to –2000 rpm when the engine runs at 1000 rpm at vehicle standstill, as indicated by circle (1) in figure 5.3. By keeping the engine speed at a slightly elevated level, it is possible to achieve a good flywheel state of charge.
To reach an even higher flywheel state of charge, a strategy can be adopted which keeps the engine speed at 1500 rpm during vehicle coast downs (2). When reaching low ratio, the drive clutch is opened and simultaneously the engine speed is increased slightly before shutdown. Using this strategy flywheel speeds up to –3000 rpm are achievable.

The minimum flywheel release-speed depends on the critical speed needed to perform a successful Impulse Start in combination with the flywheel coast down rate resulting from various frictional losses. Air drag, bearing losses and clutch drag will cause the flywheel speed to slowly decrease over time. Therefore, the flywheel release-speed must have a certain margin over the critical speed needed for impulse starting. A longer shut down period will need a higher flywheel release-speed. Simulations have been performed to investigate the flywheel speeds needed to reach certain engine speed levels. This analysis is presented in paragraph 5.3.

5.2 Preventing motion of the secondary drivetrain

When looking at the drivetrain representation in figure 5.1, it can be seen that the impulse start clutch torque also acts on the secondary drivetrain over the connection gear stage. Without countermeasures, this will result in a negative torque at the wheels during an Impulse Start action. If brake pedal release is used as a trigger for starting, this would even cause the vehicle to shortly move backwards. To prevent this, two possible solutions will be explored:

- prolonged actuation of the brake discs during impulse starting
- engaging a park pawl during impulse starting

The vibrations resulting from both solutions will be simulated and compared. In both cases large reaction torques act on the transmission housing. Therefore additional dynamics of the engine/transmission block including its mounts have been included in the model. Appendix F describes the modelling method used.

5.2.1 Prolonged brake disc actuation

Actuating the brake discs while impulse starting would prevent vehicle motion to occur. A model of the drivetrain with applied brakes has been generated in *Simulink*, see figure 5.4. The inertia J_h represents the combined inertia of the transmission housing and engine block. It is connected to the vehicle chassis via flexible engine mounts. Reaction torques of the connection gear stage r_p, the final drive gear stage r_d and the engine act on it. The dynamic engine torque model, as described in appendix C, is used to predict engine reaction torques during impulse starting.

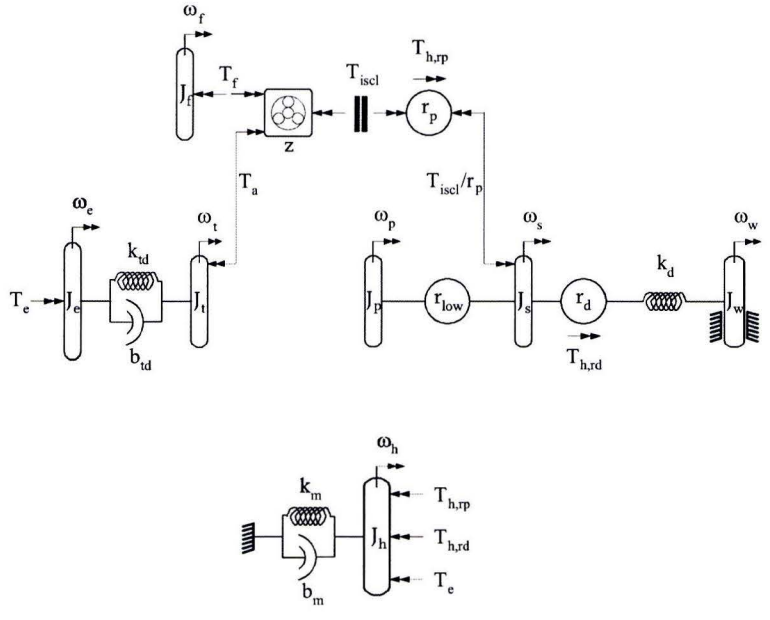

Figure 5.4: impulse starting with brakes applied

Figure 5.5 shows the results of a simulated Impulse Start with an initial flywheel speed of –2000 rpm. Impulse start clutch torque has been prescribed as a ramp, with a torque rate of 1500 Nm/s until synchronization is complete. Using these parameters, a starting time of approximately 150 ms is realised and the engine is accelerated to 700 rpm, which is considered to be more than enough to restart combustion.

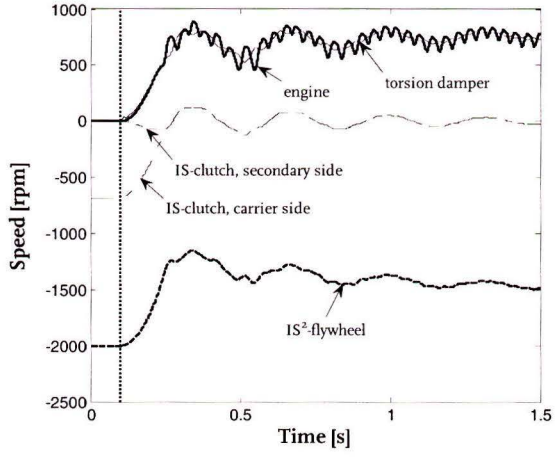

Figure 5.5(a): brake disc actuation, speeds

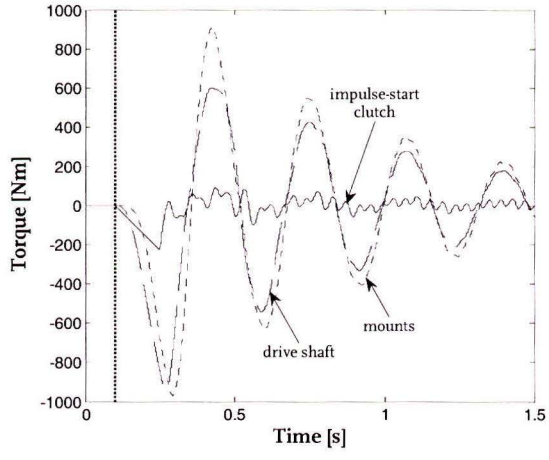

Figure 5.5(b): brake disc actuation, torques

When looking at the resulting torque levels in figure 5.5(b), very large torques acting on the drive shafts as well as the mounts can be seen. The impulse start clutch torque is amplified over the differential gear causing the drive shafts to be wound up. Upon synchronization of the clutch, relaxation of the drive shafts results in a 3 Hz vibration felt throughout the entire drivetrain. Being poorly damped, this drive shaft resonance remains present for some time.

5.2.2 Engaging a park pawl

By engaging a device similar to a conventional park pawl on the secondary side of the drivetrain, vehicle motion can also be prevented. In this case, to prevent it from moving, the secondary pulley is directly connected to the transmission housing and thus the engine block. Normally, pawl-like mechanisms need a certain amount of backlash for engaging and disengaging. In this case, a pawl free of backlash is assumed.

Again an Impulse Start was simulated with an initial flywheel speed of –2000 rpm, see figure 5.7. The same clutch torque ramp is applied as before. Both starting time and achieved engine speed are comparable to those seen in figure 5.5(a). Torque levels on both the drive shafts as well as the engine mounts are much lower in this case, since clutch torque is not amplified over the differential gear. Rotation of the engine block in its mounts will cause some minor torque to arise at the drive shafts. Because movement of the engine block is much more damped, compared to the drive shaft resonance seen earlier, vibrations

only last a fraction of the time. Based on these results, the pawl solution for suppressing vehicle motion is chosen to be implemented.

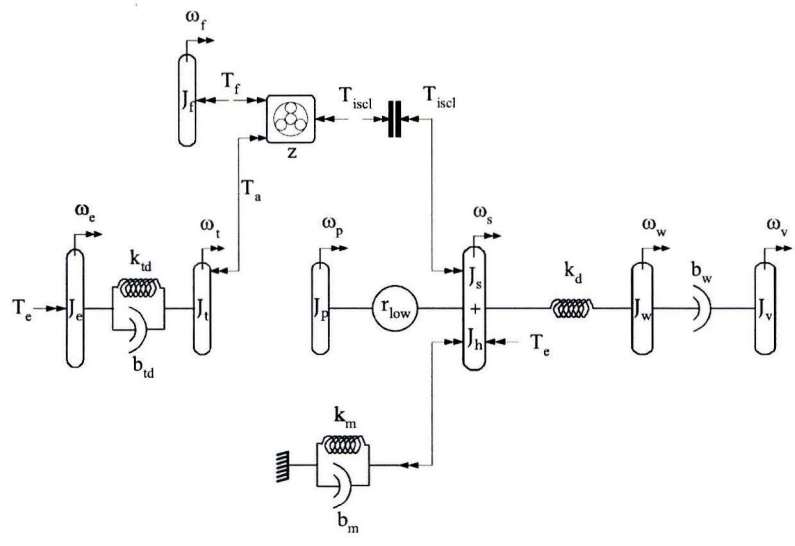

Figure 5.6: impulse starting with park pawl engaged

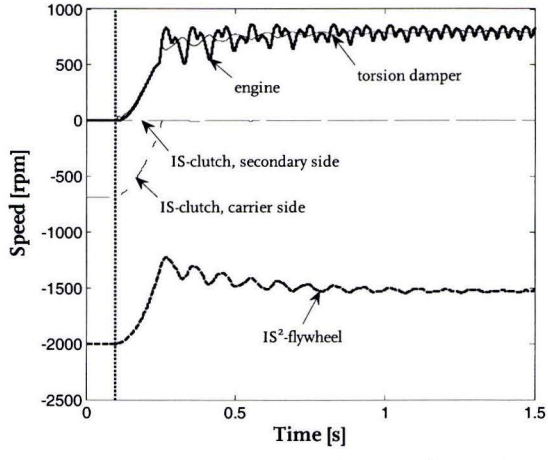

Figure 5.7(a): park pawl engaged, speeds

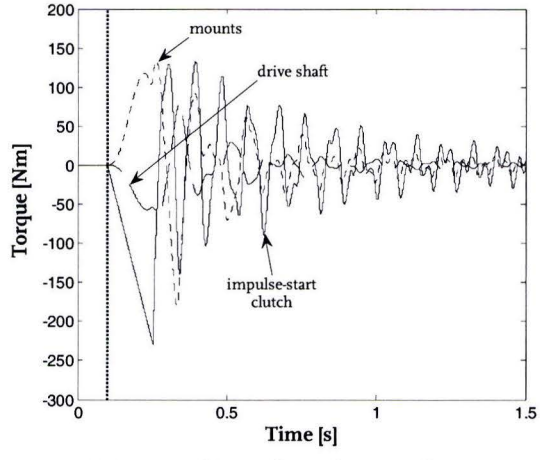

Figure 5.7(b): park pawl engaged, torques

5.3 Minimum flywheel speed needed for impulse starting

Below a certain flywheel speed it is impossible to reach a sufficiently high engine speed, which may lead to a failed attempt to resume combustion. Since the Toyota Vitz test vehicle has an idle speed of 600 rpm, it was decided that the flywheel would have to be able to crank the engine to this speed or higher. A second criterion for impulse starting is a short starting time, in the order of 150 ms.

Achievable engine speed and starting time depend on both initial flywheel speed as well as clutch closing rate. A *Simulink* model of the drivetrain in figure 5.6 is used to investigate the influence of both parameters. Combustion is not restarted in the simulation, resulting in engine cranking powered purely by the flywheel.

In figure 5.8(a) an Impulse Start is simulated with different initial flywheel speeds (bottom graph). A clutch closing rate of 1500 Nm/s is applied, resulting in the engine speeds displayed in the upper graph. It can be seen that the engine speed reached with an initial flywheel speed of –1500 rpm lies at approximately 650 rpm. An initial flywheel speed of –2000 rpm results in an achieved engine speed of over 800 rpm.

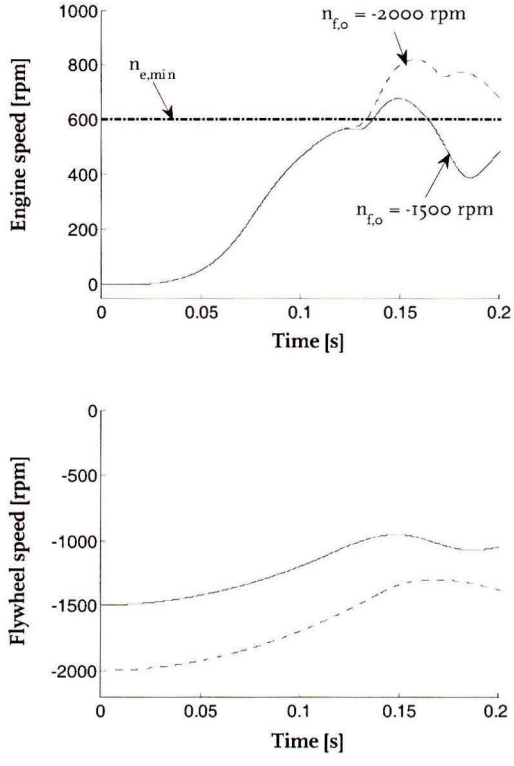

Figure 5.8(a): initial flywheel speed influence

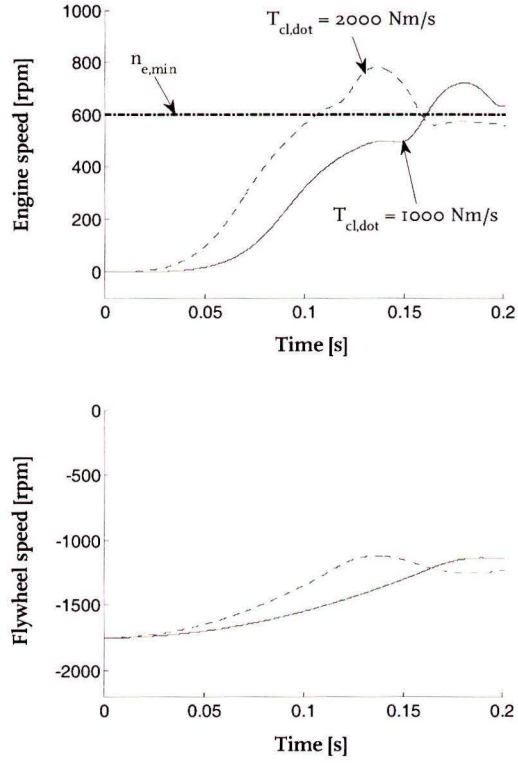

Figure 5.8(b): clutch torque rate influence

Figure 5.8(b) shows simulations of impulse starting with different clutch closing rates, for an initial flywheel speed of -1750 rpm. When closing the clutch at a rate of 1000 Nm/s a start time of 160 ms is found, whereas a closing rate of 2000 Nm/s results in a start time of 110 ms. Furthermore, the achieved engine speed is slightly increased in case of a high closing rate.

By conducting multiple simulations with different combinations of initial flywheel speed and clutch torque rate, contour plots of achievable engine speed and starting time can be constructed, see figure 5.9. It is seen that for an initial flywheel speed of -1500 rpm the

engine can still be accelerated to its idle speed by synchronizing the impulse start clutch. Tests in the vehicle will have to show whether lower target speeds are still acceptable. Figure 5.9(b) shows the influence of clutch torque rate on the time needed to reach idle speed.

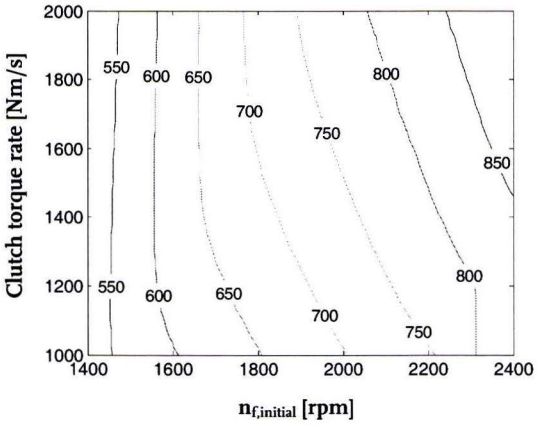

Figure 5.9(a): achievable engine speed [rpm]

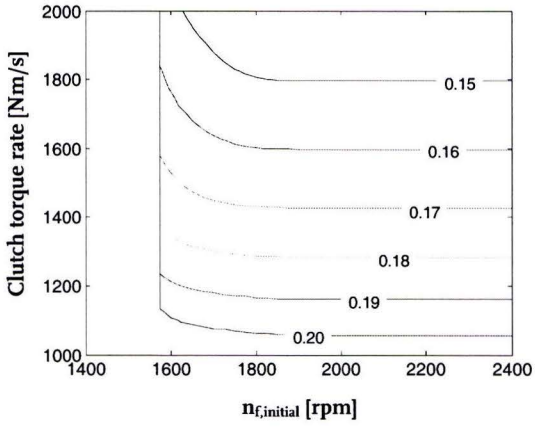

Figure 5.9(b): time to reach 600 rpm [s]

An additional parameter which might influence both starting-time and achievable engine speed is the initial crank shaft angle. The entire speed transient takes place within approximately one revolution of the crank shaft. Therefore initial crank position could prove to be of importance. Results shown in figure 5.9 were found using an initial crank angle of 0°, corresponding to top dead centre of the first cylinder.

This analysis has been repeated for five more initial crank positions, being 30°, 60°, 90°, 120° and 150° after top dead centre (TDC). Since a 4-cylinder engine behaves periodically every half revolution, an initial angle of 180° would not deliver additional insights. The results are presented in appendix E. Based on these simulation results it is concluded that the influence of the initial crank angle is relatively small. An initial flywheel speed of -1500 rpm in combination with a high clutch torque rate is enough to crank the engine to its idle speed for all initial crankshaft positions.

5.4 Testing and results

Following previous analyses, impulse starting can be tested using the available prototype transmission in the test vehicle. Initially the transmission is placed on the test stand for functionality tests of all new components. If this is successful, testing will continue in the vehicle.

5.4.1 Impulse starting on the test stand

On the test stand an electric machine powers the primary input shaft of the transmission (figure 5.10).

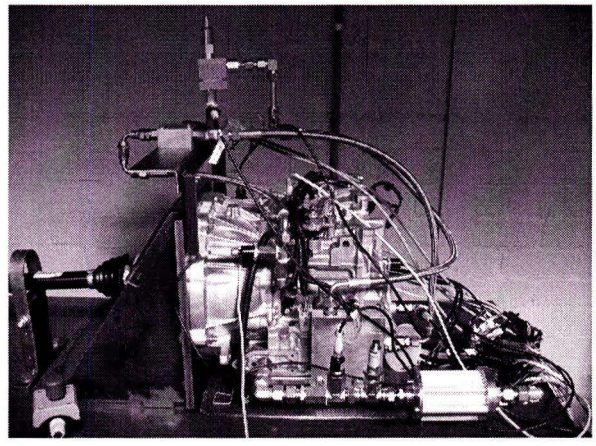

Figure 5.10: IS²-CVT on the test stand

A schematic overview of the hydraulic components involved with impulse starting is presented in figure 5.11. The impulse start clutch pressure is controlled with a proportional valve. Whenever the engine is running, pressure is supplied by the hydraulic pump. For engine stop periods an accumulator (with shut-off valve) has been added to the hydraulic circuit to provide pressure. In this case, a check valve prevents hydraulic flow to leak backwards through the supply line. A complete overview of the transmission's hydraulics can be found in appendix G.

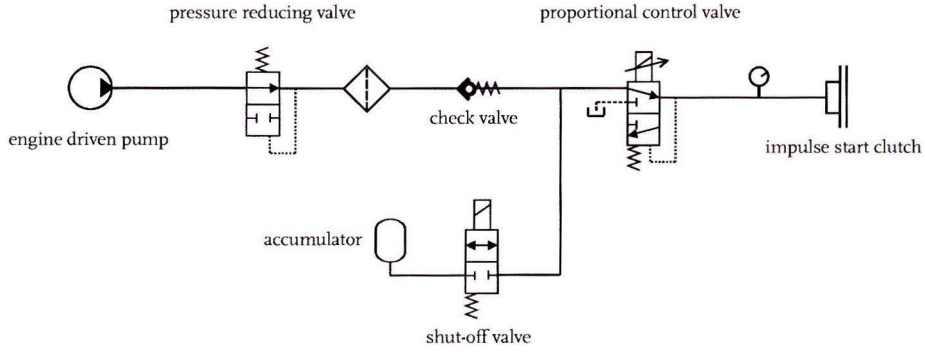

Figure 5.11: impulse start clutch hydraulics

The stationary characteristic of the proportional valve has been identified, see figure 5.12(a). By looking at flywheel accelerations during clutch synchronization at different pressure

levels, the clutch characteristic can also be determined. The characteristic in figure 5.12(b) has been determined at low rotational speeds, where centrifugal pressure effects can be neglected. An offset of 1.3 bar can be seen, corresponding to the pressure needed to overcome the spring package acting on the plunger. Above this 'kiss-point' 45 Nm is generated for every additional bar of pressure.

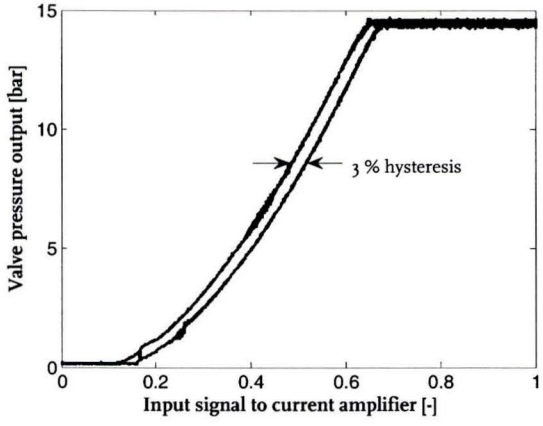

Figure 5.12(a): control signal to pressure output

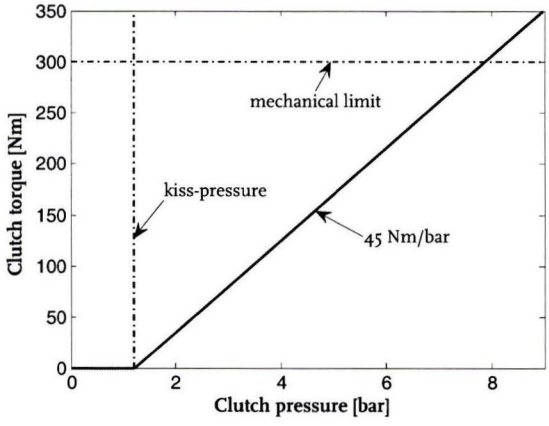

Figure 5.12(b): clutch pressure to torque

The coast down rate of the flywheel has also been identified on the test stand. Two measured flywheel coast downs are displayed in figure 5.13. In the speed range of interest (-3000 until -1500 rpm) deceleration is almost constant. Frictional losses cause the flywheel to decelerate at an average rate of approximately 29 rpm per second. This corresponds to a combined drag torque of 0.25 Nm acting on the flywheel. A maximum standby period slightly over 50 seconds is seen when released at -3000 rpm. Transmission temperature during this test was not completely at its operating value, which is difficult to reach when testing without a load on the test stand. When fully warm, the coast down time is expected to be lower.

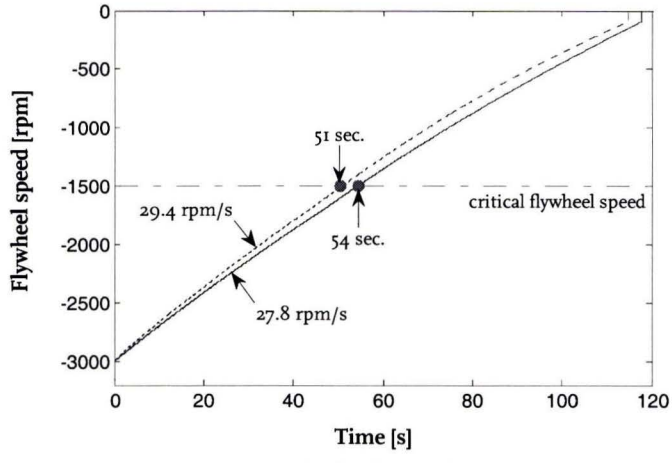

Figure 5.13: flywheel coast down rate

Initial testing of the Impulse Start functionality has been done on the test stand. Instead of the combustion engine, the electric machine is accelerated by the IS²-flywheel. It has less inertia and less friction than a combustion engine, but it can nevertheless be used as a substitute. One of the performed tests is displayed in figure 5.14. The carrier speed has been reconstructed, based on flywheel (sun) and torsion damper (annulus) speeds.

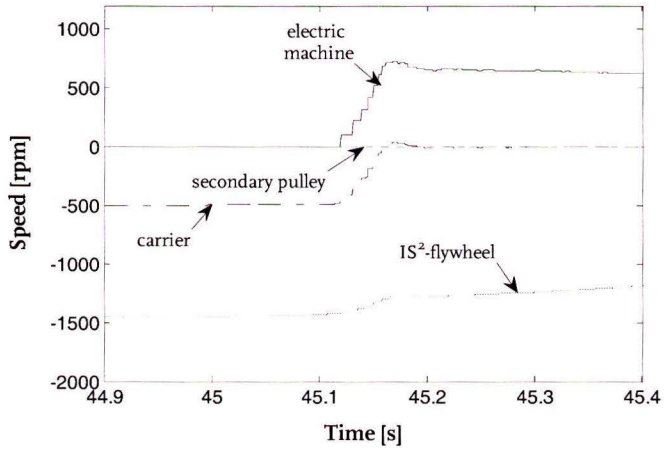

Figure 5.14: impulse starting the electric machine on the test stand

During these tests, the controls of the proportional pressure valve as well as the accumulator shut-off valve where tested successfully. It was noticed that the response time of the impulse start clutch was longer than favorable (0.3 seconds). This is a result of leakage along rotating seals in the plunger chamber, which causes transmission oil to leak out. When initiating an Impulse Start the plunger chamber needs to be completely filled before any torque can be transmitted. A pre-filling strategy was considered, by using the available pressurized oil in the accumulator to compensate for leakage during the standby period. This resulted in a delay of only 0.07 seconds. However, the limited accumulator capacity does not allow compensation of the leakage for long periods. Since this would result in an unacceptable penalty on idle-stop time, the pre-filling strategy was abandoned.

5.4.2 Impulse Start performed in the vehicle

Based on the results in paragraph 5.2, the conventional park pawl has been automated by means of a solenoid actuator. The park pawl is engaged during Impulse Starts to provide reaction torque in the drivetrain during the start while simultaneously preventing vehicle motion.

A measured Impulse Start cycle is displayed in figure 5.15. The flywheel is accelerated into its negative speed range when the vehicle is coming to a standstill. When a predefined flywheel target speed is reached, the impulse start clutch is opened and the engine is shut down. After a stand-still period of 25 seconds, flywheel speed becomes critical and triggers

an Impulse Start. The whole cycle is controlled by a *Stateflow* chart implemented in the *Simulink* control software.

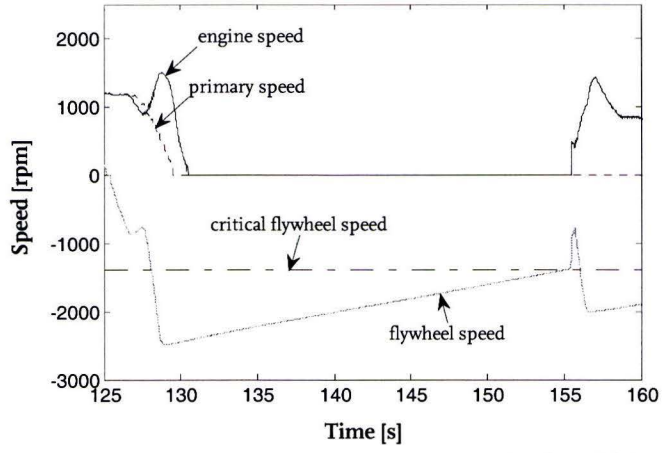

Figure 5.15: Impulse Start cycle measured in the vehicle

In figure 5.16 the measured Impulse Start action has been enlarged. It is seen that an engine speed slightly over 500 rpm can be achieved by closing the impulse start clutch. This is in accordance with the results of paragraph 5.3. Once rotating, the ECU needs one full revolution to determine the crankshaft position. Afterwards another full rotation is needed to prepare a combustible mixture in one of the cylinders. This explains the small drop in engine speed after clutch synchronization. Once combustion is restarted the engine speeds up and the flywheel is accelerated further into its negative speed range again. The engine initially accelerates itself to 1500 rpm, which is not strictly necessary. By lowering this target speed, additional fuel can be saved and auditive comfort can be improved. However, to do so would require access to the ECU which is impossible at this time.

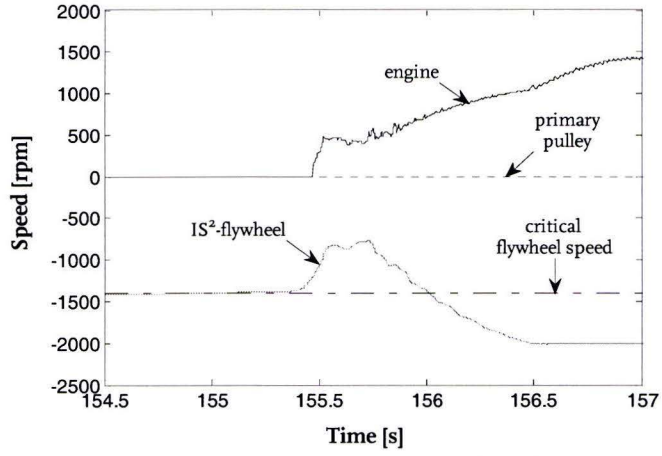

Figure 5.16: Impulse Start triggered by critical flywheel speed

The second possibility for an Impulse Start to be triggered is a driver brake-release followed by a vehicle launch. A measurement of this situation can be seen in figure 5.17.

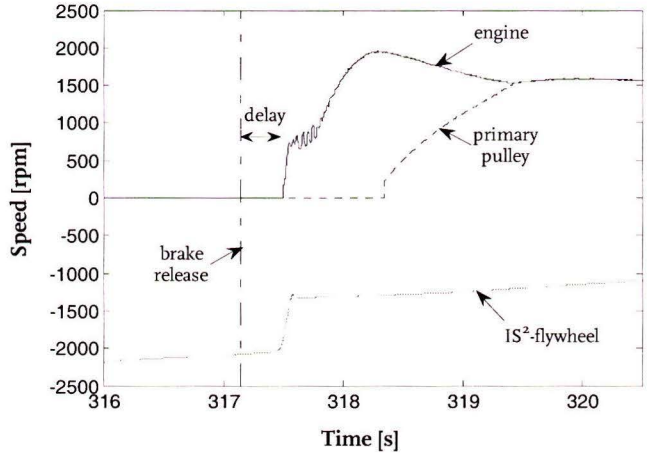

Figure 5.17: Impulse Start triggered by brake pedal release

In this case the engine is accelerated to 750 rpm by the flywheel before combustion starts. A delay of 0.3 seconds is seen after releasing the brake pedal. This is caused by the open hydraulic circuit used to actuate the impulse start clutch, as was already addressed in paragraph 5.4.1. Once combustion is resumed, the launch clutch is actuated to initiate a vehicle launch. The high engine speed seen after impulse starting is not a problem in this case, as is corresponds well to the desired engine speed during vehicle launch, which begins immediately afterwards.

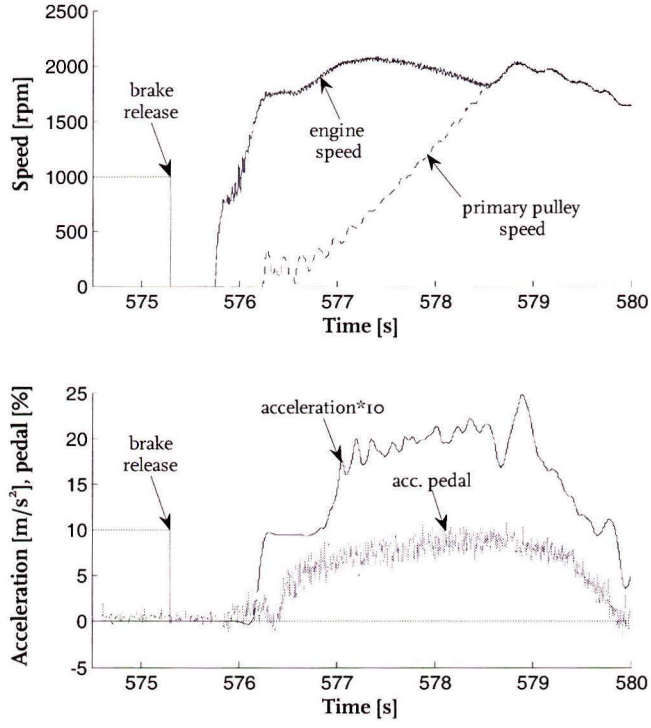

Figure 5.18: Impulse Start action, followed by launch

Figure 5.18 shows another Impulse Start followed by a launch. In the lower graph the corresponding brake pedal release, accelerator pedal depression and vehicle acceleration are displayed (note that vehicle acceleration is scaled up by a factor of 10). It is seen that the vehicle starts accelerating approximately 0.8 seconds after brake pedal release is detected.
A launch can only be initiated once hydraulic pressure for the launch clutch is available. Since the hydraulic pump is driven by the engine, it takes some time for pump pressure to reach its normal operating level. Tests have shown that this delay is much smaller than the delay caused by the impulse start clutch actuation. It might be possible to actuate the launch clutch somewhat earlier and stronger during impulse starting. This would result in a faster acceleration response and lower engine speeds. However, these adaptations have not been tested in the vehicle yet.

In figure 5.19 a comparison is made between conventional (starter motor) starting and impulse starting. The delayed impulse start clutch response is a large penalty on overall starting time. However, an Impulse Start with hydraulic delay is still faster than a conventional start. For future applications a closed hydraulic circuit or minimal leakage is recommended. An electrically powered pump, replacing the current accumulator, could also be used to compensate for leakage during standstill periods.

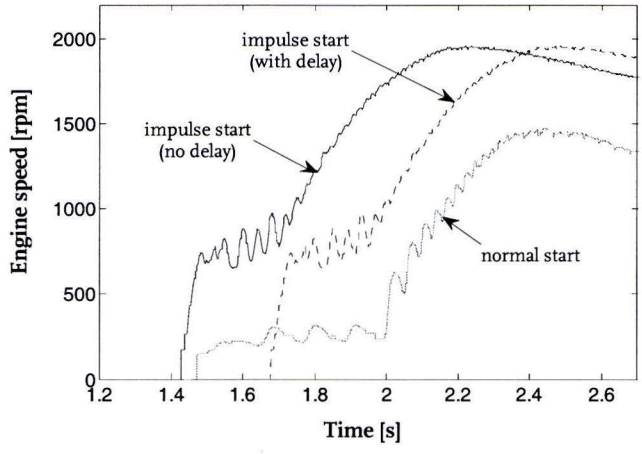

Figure 5.19: comparison between conventional starting and impulse starting

Chapter 6

Performance analysis Zero Inertia vs. Impulse Shift

Through the Impulse Shift functionality the IS²-module enables elimination of rubber-band behaviour seen in conventional CVT's. If the driver demands a sudden power increase a downshift is performed, during which engine speed increases and flywheel speed decreases. As a result positive torque at the wheels is available instantly, see figure 6.1.

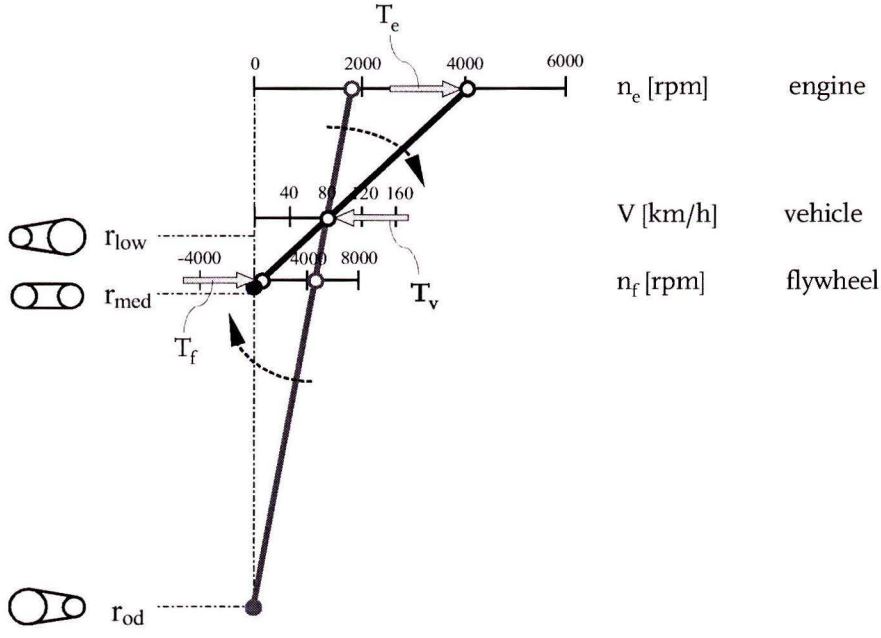

Figure 6.1: nomogram of a kick down action at 80 km/h

The grey curve represents the situation during constant speed driving at 80 km/h. To achieve low fuel consumption, the CVT ratio is controlled in overdrive to keep the engine at low speed and high torque (figure 6.2). When performing a kick down the variator is controlled towards medium ratio, represented by the black curve.

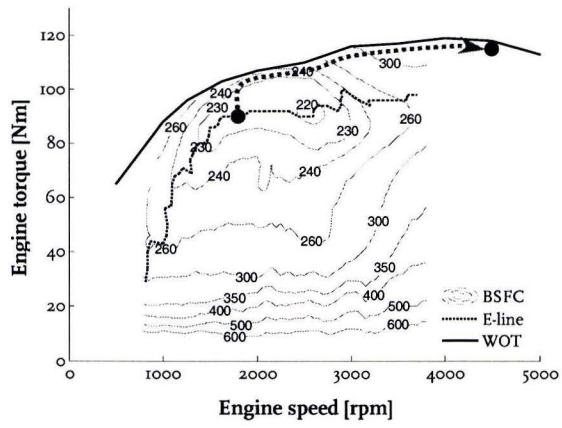

Figure 6.2(a): engine operating point transient

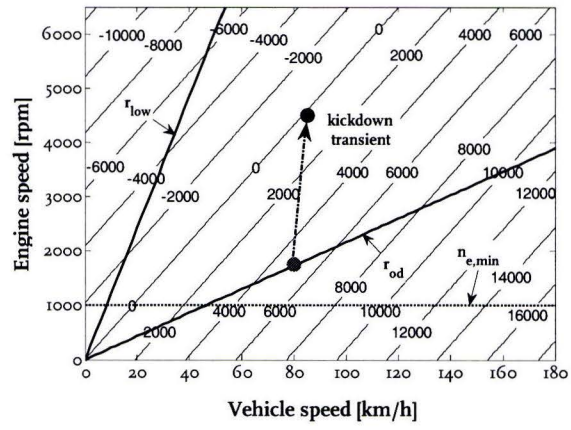

Figure 6.2(b): flywheel speed transient

Two different control strategies for the performance downshift will be investigated. When applying the Zero Inertia strategy, the drive clutch remains fully closed during downshifting. Saturation of CVT shift speed may penalize performance, in this case the Impulse Shift control strategy could be favourable. By temporarily opening the drive clutch, the engine will accelerate by its combustion torque while experiencing a load torque from the planetary gear and the IS²-flywheel. Achievable performance of both strategies will be analysed and compared in this chapter.

6.1 Zero Inertia mode

When applying the Zero Inertia strategy, the drivetrain representation of figure 6.3 is used for analyses. In this paragraph the kinetic energy within the drivetrain, as well as achievable vehicle acceleration at instationary drivetrain dynamics is researched.

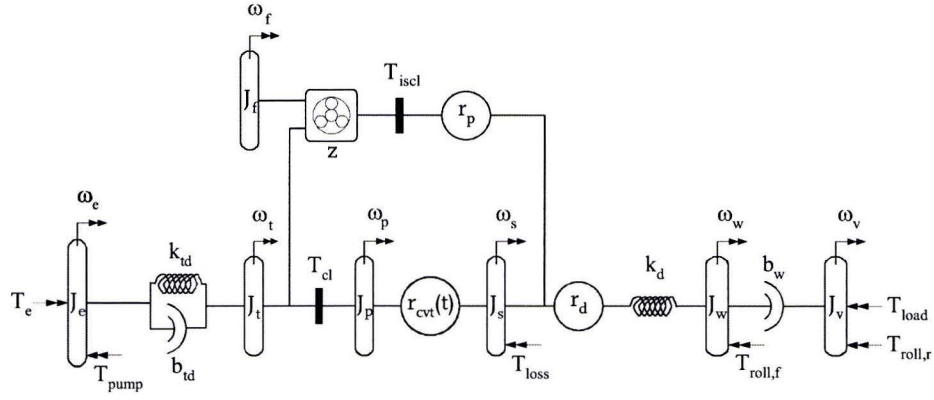

Figure 6.3: Zero Inertia mode

6.1.1 Kinetic energy

With both clutches fully closed, the flywheel speed can be expressed as:

$$\omega_f = \alpha_s \omega_s - \alpha_p \omega_p \qquad \text{with:} \quad \alpha_p = z \;,\; \alpha_s = \frac{z+1}{r_p} \;,\; \omega_s = r_{cvt}\omega_p \tag{6.1}$$

Rewriting of (6.1) shows that flywheel speed is zero in case CVT ratio equals:

$$r_{cvt} = r_{gn} = \frac{\alpha_p}{\alpha_s} = \frac{z r_p}{z+1} \tag{6.2}$$

Below this so-called geared-neutral ratio flywheel speed is negative, while higher ratio's result in a positive flywheel speed. This means that during a downshift action starting at overdrive, the kinetic energy level of the flywheel is continuously reduced until geared-neutral ratio is reached. The release of this kinetic energy compensates for the increasing kinetic energy level of all primary sided inertia's, that is J_e, J_t and J_p in figure 6.3. Kinetic energy of both flywheel and primary inertia's can be written as a function of secondary pulley speed and CVT ratio:

$$E_f = \tfrac{1}{2} J_f \omega_f^2 \qquad \text{with:} \quad \omega_f = \alpha_s \left(1 - \frac{r_{gn}}{r_{cvt}}\right)\omega_s \tag{6.3}$$

$$E_{pri} = \tfrac{1}{2}\left(J_e + J_t + J_p\right)\omega_p^2 \qquad \text{with:} \quad \omega_p = \frac{\omega_s}{r_{cvt}} \tag{6.4}$$

By dividing both expressions by vehicle kinetic energy level:

$$E_{veh} = \tfrac{1}{2}(J_v r_d^2 + 2J_w r_d^2 + J_s)\omega_s^2 \tag{6.5}$$

a measure for relative kinetic energy is found, which is only dependent on CVT ratio. In case of the flywheel this leads to:

$$e_f = \frac{E_f}{E_{veh}} = \frac{\tfrac{1}{2} J_f \omega_f^2}{\tfrac{1}{2}(J_v r_d^2 + 2J_w r_d^2 + J_s)\omega_s^2}$$

$$= \frac{J_f}{J_v r_d^2 + 2J_w r_d^2 + J_s} \alpha_s^2 r_{gn}^2 \left(\frac{1}{r_{gn}} - \frac{1}{r_{cvt}}\right)^2 \tag{6.6}$$

For the primary sided inertia's the following expression is found:

$$e_{prim} = \frac{E_{prim}}{E_{veh}} = \frac{\frac{1}{2}(J_e + J_t + J_p)\omega_p^2}{\frac{1}{2}(J_v r_d^2 + 2J_w r_d^2 + J_s)\omega_s^2}$$

$$= \left(\frac{J_e + J_t + J_p}{J_v r_d^2 + 2J_w r_d^2 + J_s} \right) \frac{1}{r_{cvt}^2} \tag{6.7}$$

In figure 6.4 the relative kinetic energy levels are displayed as a function of CVT ratio. Relative primary energy increases quadratically with decreasing ratio. Relative flywheel energy shows a minimum at geared-neutral ratio, where the flywheel is at standstill.

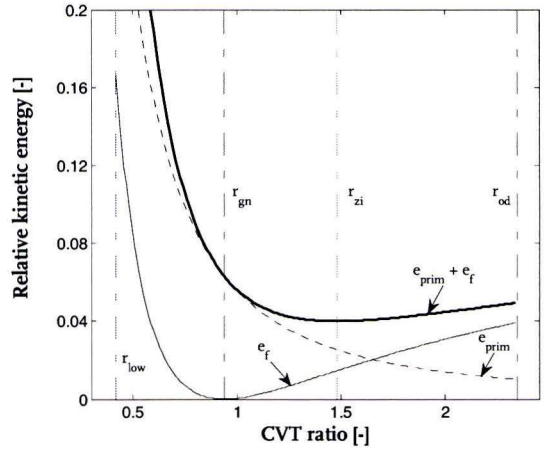

Figure 6.4: relative kinetic energy

When considering the sum of both relative energy's, a minimum is found somewhere between geared-neutral and overdrive ratio. Here the combined relative kinetic energy is insensitive for ratio-change:

$$\frac{\delta(e_{prim} + e_f)}{\delta r_{cvt}} = 0 \tag{6.8}$$

When downshifting through this ratio, the decrease in flywheel kinetic energy exactly equals the increase of primary kinetic energy. Because overall relative kinetic energy doesn't change in this ratio, it is named *Zero Inertia* ratio:

$$r_{zi} = \left(1 + \frac{J_e + J_t + J_p}{J_f \alpha_s^2 r_{gn}^2} \right) r_{gn} \qquad \text{or} \qquad r_{zi} = \left(1 + \frac{J_e + J_t + J_p}{J_f z^2} \right) r_{gn} \tag{6.9}$$

By substituting the current parameter values, a Zero Inertia ratio of $r_{zi} = 1.46$ is found.

6.1.2 Vehicle acceleration

As a measure for kick down performance, the vehicle acceleration is evaluated. By assuming all compliances to be rigid and neglecting drivetrain losses, according to [10] the lumped drivetrain dynamics can be described by:

$$J^*_{v,zi}\frac{\dot{v}_v}{R_w} = \frac{T_e}{r_{cvt}r_d} + \frac{J^*_{prim}v_v}{R_w r^3_{cvt} r^2_d}\dot{r}_{cvt} - T_{rl} \tag{6.10}$$

where:
$$J_{prim}{}^* = J_e + J_t + J_p + \left(z^2 - \frac{z^2+z}{r_p}r_{cvt}\right)J_f$$

$$J^*_{v,zi} = m_v R^2_w + 2J_w + \frac{J_s}{r^2_d} + \frac{J_e + J_t + J_p}{r^2_{cvt} r^2_d} + \left(\frac{z}{r_{cvt}} - \frac{z+1}{r_p}\right)^2 \frac{J_f}{r^2_d}$$

The lumped vehicle acceleration can be expressed as the sum of three torques:

$$J^*_{v,zi}\dot{\omega}_v = \frac{1}{r_{cvt}r_d}T_e + T_G - T_{rl} \qquad \text{with:} \qquad T_G = \frac{J^*_{prim}v_v}{R_w r^3_{cvt} r^2_d}\dot{r}_{cvt} \tag{6.11}$$

Apart from terms depending on engine and road-load torque a third term known as the *gyrator element* is present. It scales proportional with vehicle speed:

$$T_G = G(r_{cvt}, \dot{r}_{cvt})v_v \qquad \text{with:} \qquad G = \frac{J^*_{prim}(r_{cvt})\dot{r}_{cvt}}{R_w r^3_{cvt} r^2_d} \tag{6.12}$$

The gyrator modulus '*G*' is a function of the CVT ratio and its shift speed. The corresponding contour plot is displayed in figure 6.5(b). By setting flywheel inertia to zero, a gyrator modulus for the conventional layout can be found, see figure 6.5(a). One can see that for the conventional CVT the gyrator modulus is negative for the full downshift range ($\dot{r}_{cvt} < 0$) and positive for the full upshift range ($\dot{r}_{cvt} > 0$).

In Zero Inertia mode the gyrator modulus has a 'saddle-shape', being positive when downshifting at ratio's above r_{zi} and negative when downshifting at ratio's below r_{zi}. At $r_{cvt} = r_{zi}$, the gyrator modulus is zero and changes sign. When downshifting in the range $r_{gn} < r_{cvt} < r_{zi}$, the gyrator modulus is negative, but less negative than for a conventional CVT. At geared-neutral ratio, where the IS^2-flywheel is at standstill, the gyrator modulus in Zero Inertia mode is the same as in CVT mode.

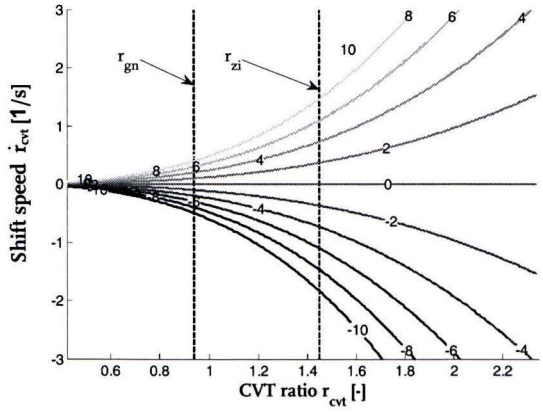

Figure 6.5(a): gyrator modulus for CVT mode

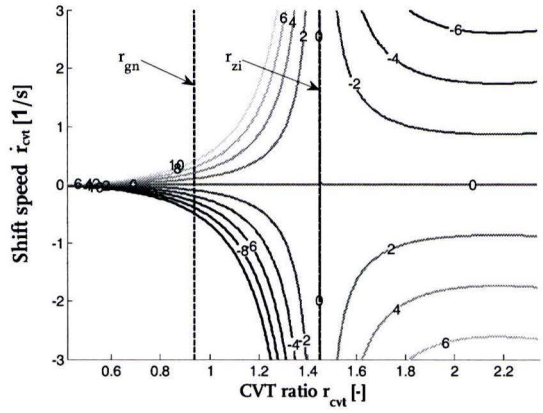

Figure 6.5(b): gyrator modulus for ZI mode

When downshifting below geared-neutral ratio, the IS²-flywheel is accelerated into its negative speed range, thereby acting as a load instead of a mechanical assist. Therefore, it might be beneficial to disconnect the IS²-flywheel when downshifting below geared-neutral. Especially when performance is requested at relatively low vehicle speeds between 50 and 80 km/h, disconnecting the flywheel is necessary, since the ratio transient is likely to end below geared-neutral ratio.

Vehicle acceleration in Zero Inertia mode is given by:

$$\dot{\omega}_v = \frac{\frac{T_e}{r_{cvt} r_d} + T_G - T_{rl}}{J^*_{v,zi}} \tag{6.13}$$

In paragraph 6.3 this expression is compared to the results found for the Impulse Shift strategy, which is treated in the next paragraph.

6.2 Impulse Shift mode

When applying the Impulse Shift strategy, the drivetrain representation of figure 6.6 is used for analyses. In case the driver performs a (semi-)kick down action the drive clutch is instantly opened, enabling the engine to accelerate while pushing itself of against the IS²-flywheel. The torque at the wheels originates fully from the parallel transmission branch in this case.

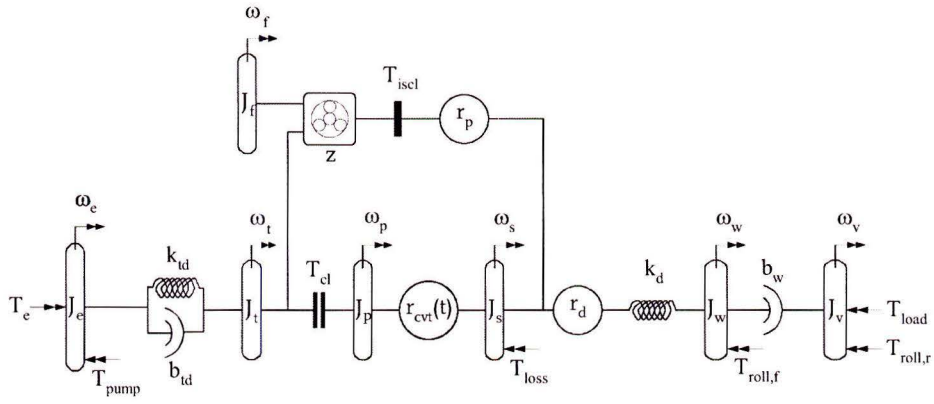

Figure 6.6: Impulse Shift mode

In paragraph 3.2 it was shown that the differential equation for the equivalent secondary pulley inertia can be written as:

$$J_s^{**}\dot{\omega}_s = \sigma_{cl}T_{cl} + T_{shift,s} - T_{ds} - T_{loss} + \gamma_s T_{td} \tag{6.14}$$

When in Impulse Shift mode and neglecting drivetrain losses, equation (6.14) reduces to:

$$J_s^{**}\dot{\omega}_s = T_{shift,s} - T_{ds} + \gamma_s T_{td} \tag{6.15}$$

Considering all compliances to be rigid, equation (6.15) can be manipulated to find the lumped vehicle dynamics:

$$J_{v,is}^{*}\dot{\omega}_v = \frac{\gamma_{s,lump}}{r_d}T_e + \frac{T_{shift,s}}{r_d} - T_{rl} \tag{6.16}$$

where:

$$J_{v,is}^{*} = m_v R_w^{\,2} + 2J_w + \frac{J_{s,lump}^{**}}{r_d^{\,2}}$$

$$J_{s,lump}^{**} = J_s^{*} - \frac{1}{J_e + J_t^{*}}\left(J_f \frac{z^2 + z}{r_p}\right)^2$$

$$\gamma_{s,lump} = \frac{J_f}{J_e + J_t^{*}}\frac{z^2 + z}{r_p}$$

Beside a road-load torque, vehicle acceleration is a function of engine torque and variator shift torque. Even though the drive clutch is open during Impulse Shifting, a downshift action is still needed. Without doing so, the primary pulley would remain at low speed, while engine speed continuously increases. The shift torque term takes primary pulley acceleration into account.

Vehicle acceleration in Impulse Shift mode is given by:

$$\dot{\omega}_v = \frac{\frac{\gamma_{s,lump}}{r_d} T_e + \frac{T_{shift,s}}{r_d} - T_{rl}}{J^*_{v,is}} \tag{6.17}$$

In the next paragraph the achievable accelerations in Zero Inertia and Impulse Shift mode are compared.

6.3 Comparison of kick down performance

By inserting engine torque and various shift speeds into (6.13) and (6.17), achievable acceleration can are compared. This is done for a constant engine torque of 110 Nm (assuming a flat WOT-curve, as in figure 6.7) while driving 70 km/h. A constant road-load torque of 90 Nm has been assumed, which corresponds to driving 70 km/h on a flat road.

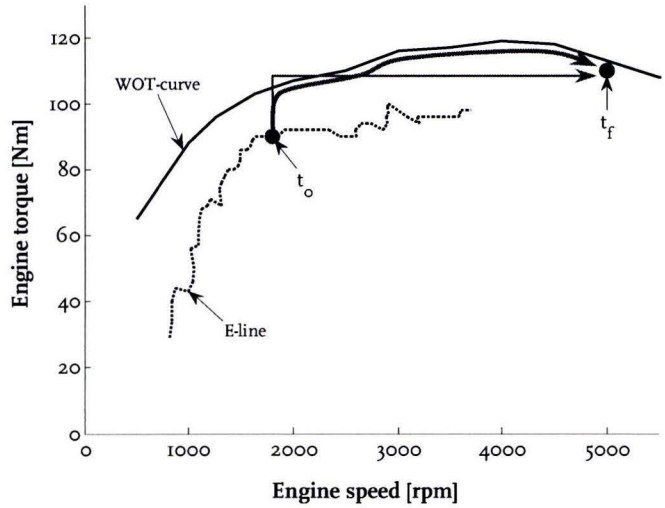

Figure 6.7: engine operating point transient for a kick down at 70 km/h

Figure 6.8(a) shows the acceleration levels for Zero Inertia shifting. Clearly, acceleration increases with shift speed above r_{zi}. Below this ratio, a higher shift speed results in lower acceleration. All curves intersect at Zero Inertia ratio, indicating that the acceleration at this ratio is independent of shift speed. These results are in accordance with those seen in figure 6.5. In figure 6.8(b) similar curves are displayed for the Impulse Shift strategy. Acceleration level is constant when no shifting takes place during the clutch opening period. Increasing downshift speed reduces the acceleration level, as the primary pulley acts as a parasitic load.

Comparing both figures shows that an acceleration advantage can be obtained by using the Zero Inertia shift strategy. However, high shift speeds above r_{zi} are necessary to outperform the Impulse Shift strategy.

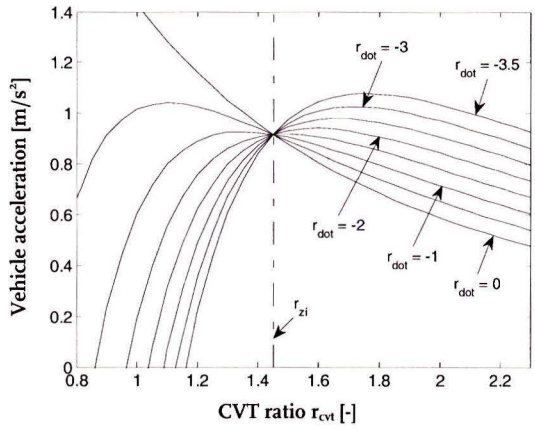

Figure 6.8(a): ZI-acceleration for range of ratio's and shift speeds at V = 70 km/h and T_e = 110 Nm

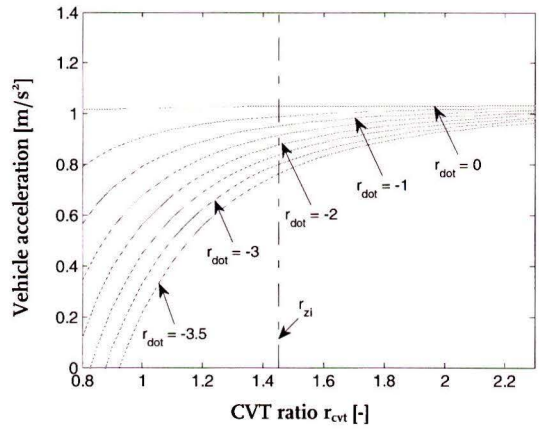

Figure 6.8(b): IS-acceleration for range of ratio's and shift speeds at V = 70 km/h and T_e = 110 Nm

Similar plots have been constructed for a vehicle speed of 100 km/h, again in combination with a constant engine torque of 110 Nm. The road-load torque is 130 Nm when driving this speed on a flat road.

Figure 6.9(a) shows the results for Zero Inertia downshifting. The influence of shift speed is more substantial in this case. This can be explained by the fact that the gyrator torque (see equation 6.12) scales proportionally with vehicle speed. In figure 6.9(b) the accelerations for impulse shifting are displayed.

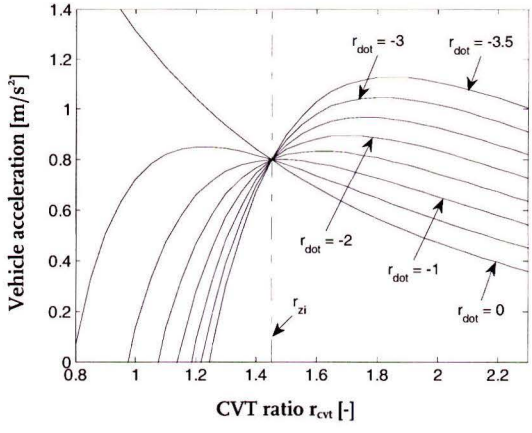

Figure 6.9(a): ZI-acceleration for range of ratio's and shift speeds at V = 100 km/h and T_e = 110 Nm

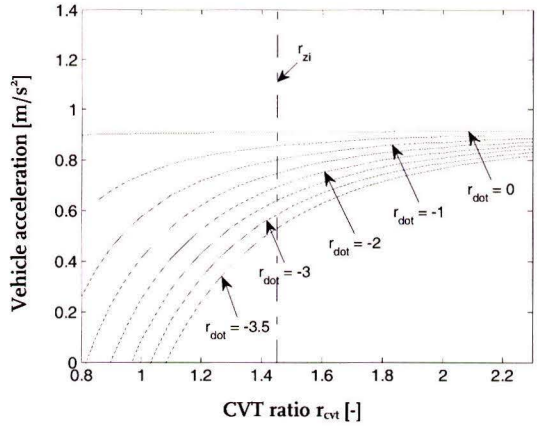

Figure 6.9(b): IS-acceleration for range of ratio's and shift speeds at V = 100 km/h and T_e = 110 Nm

Above r_{zi} the Zero Inertia strategy again outperforms the Impulse Shift strategy, but only in case very high shift speeds can be realized. The difference is even more substantial at 100 km/h, resulting from the gyrator effect mentioned above. If the shift speed is limited by the

transmission's variator, impulse shifting could result in the best performance. For the Toyota Vitz test vehicle this is not the case however, as will be shown in the next chapter.

Looking at figure 6.9(a), the best kick down performance can be achieved by maximizing shift speed above r_{zi}. This results in an unwanted side effect however. As mentioned before, vehicle acceleration at Zero Inertia ratio is independent of shift speed. When maximizing shift speed at higher ratio's, a drop in acceleration level results near r_{zi}. This would be comparable to a sag phenomenon seen in conventional CVT drivetrains. Engine WOT-torque increases slightly during the transient, which offers some compensation.

When looking at figure 6.8(a) and 6.9(a), it is seen that there is a combination of CVT ratio's and shift speeds that results in a constant acceleration level over the full downshift range. This combination is indicated with the arrow in figure 6.10. By starting with a high shift speed in overdrive, and progressively reducing shift speed towards lower ratio's, a constant acceleration can be achieved.

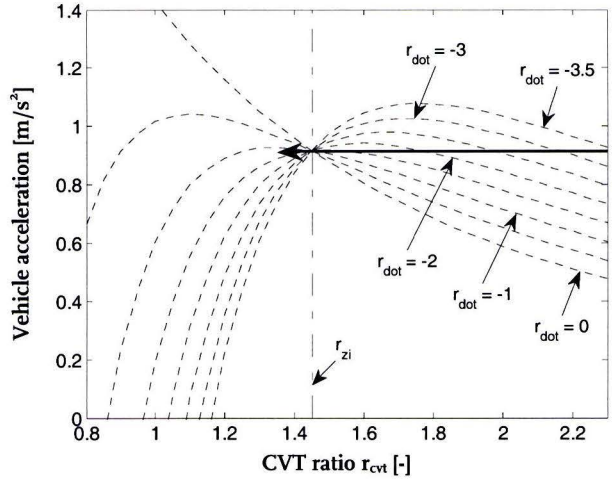

Figure 6.10: combination of ratio's and shift speeds resulting in a constant acceleration

It was found that the shift trajectory indicated with the arrow in figure 6.10 results when primary pulley acceleration is prescribed as:

$$\dot{\omega}_p^* = \frac{T_e}{J_e + J_t + J_p + z^2 J_f} \tag{6.18}$$

being 236 rad/s² (or 2250 rpm/s) for the 110 Nm engine torque example. When applying this shift trajectory no torque is transmitted through the variator. Instead, all torque is temporarily directed through the parallel transmission branch.

In the next chapter, a method for ratio set point generation will be described and validated by measurements done in the test vehicle.

Chapter 7

Dynamic set point generation for Zero Inertia mode

Measurements have shown that the Aisin AW transmission present in the Toyota Vitz test vehicle is capable of high shift speeds. Therefore, Zero Inertia strategy is chosen to optimise kick down performance. Since torque at the wheels depends strongly on both CVT ratio as well as shift speed a set point generation tool is needed.

7.1 Ratio trajectory generation

The desired engine operating point is determined by accelerator pedal depression and vehicle speed. During normal driving conditions, the goal is to keep the engine on the E-line, enabling low fuel consumption. This strategy is abandoned when performance is requested by the driver. Interpretation of accelerator pedal depression is done by means of a DPT (Driver Pedal Translation) map. Every combination of vehicle speed and pedal depression results in a desired engine power, see figure 7.1.

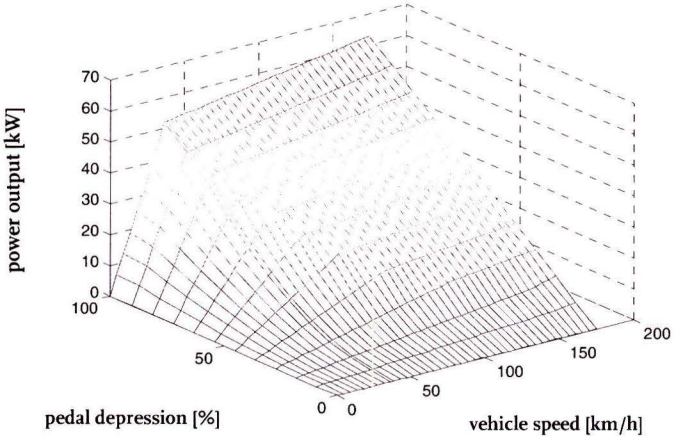

Figure 7.1: driver pedal translation map

The DPT map acts as a look-up table for the coordinated control, providing a desired power output. To find the corresponding engine operating point, the desired power level needs to be localized on the E-line. This is done by using a power interpretation of the E-line (figure 7.2).

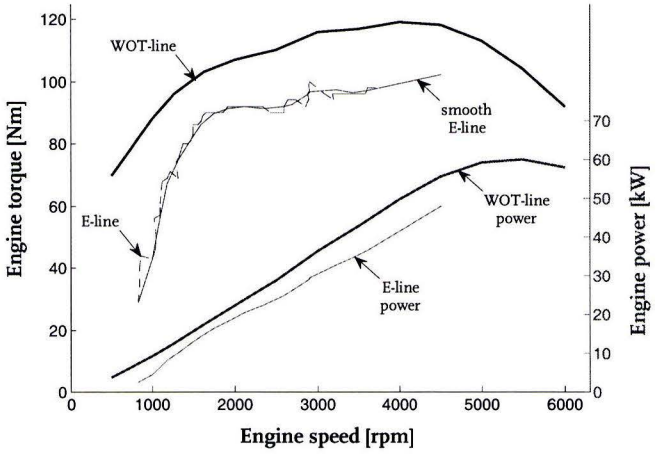

Figure 7.2: torque and power interpretations of the E-line and WOT-line

Having determined the desired engine speed and torque, CVT ratio follows from:

$$r_{cvt,d} = \frac{v_v}{R_w r_d \omega_{e,d}} \tag{7.1}$$

During mild driving situations shifting is quasi-stationary. In these cases shift speed is not a critical control parameter. When a large and fast ratio transient is requested, both ratio and shift speed need to be controlled. As explained in previous chapters, system behaviour changes when passing certain CVT ratio's. Between Zero Inertia and overdrive ratio, a high shift speed is favourable, resulting in both a time and wheel torque advantage. Between geared-neutral and Zero Inertia ratio, shift speed needs to be reduced, since flywheel deceleration no longer fully compensates primary inertia acceleration. Finally, below geared-neutral the flywheel behaves as a parasitic load, which can be prevented by opening the impulse start clutch.

In Chapter 6 a shift speed expression was found that resulted in a constant vehicle acceleration and zero torque transfer through the variator (despite having a fully closed drive clutch):

$$\dot{\omega}_p^* = \frac{T_e}{J_e + J_t + J_p + z^2 J_f} \tag{7.2}$$

For a constant engine (WOT-)torque, this shift speed will result in a constant wheel torque throughout a large part of the downshift, see figure 7.3.

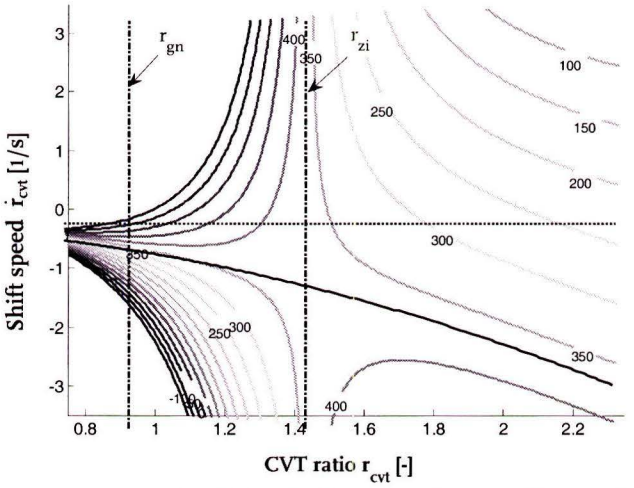

Figure 7.3: contour plot of the wheel torque at T_e = 100 Nm and 80 km/h

The black curve corresponds to the shift speed given by (7.2), it forms a wheel torque asymptote. A lower shift speed leads to positive variator torque, whereas a higher shift speed results in negative variator torque. In this case mechanical power-looping occurs, meaning that a certain amount of power flowing through the parallel path is directed back through the variator. A number of shift lines have been defined around the wheel torque asymptote, see figure 7.4. The shift lines are defined as:

- $r_{zi} < r_{cvt} \leq r_{od}$ $\qquad \dot{\omega}_{p,d} = C_1 \dot{\omega}_p^* \qquad C_1 \geq 1$ (7.3)
- $r_{cvt} \leq r_{zi}$ $\qquad \dot{\omega}_{p,d} = C_2 \dot{\omega}_p^* \qquad C_2 \leq 1$ (7.4)

where the gains C_1 and C_2 are used to scale primary acceleration over the corresponding ratio range. If C_1 and C_2 are both unity, the torque asymptote of figure 7.3 is found.

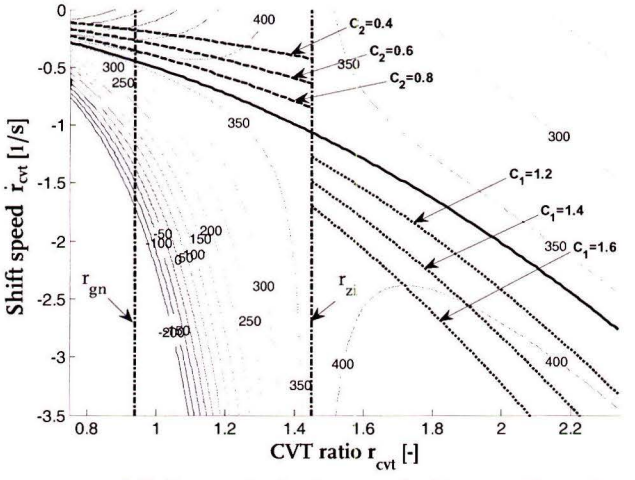

Figure 7.4: shift lines and wheel torque for T_e = 100 Nm at 80 km/h

If C_1 is chosen above unity, high shift speeds in the region above Zero Inertia ratio lead to extra torque at the wheels. Furthermore, Zero Inertia ratio is reached sooner. If C_2 is chosen below unity, a torque advantage can be obtained below Zero Inertia ratio, however the final ratio will be reached later. Various combinations of both gains are possible, making a discontinuous transition at Zero Inertia ratio. A discontinuity in shift speed at this ratio is allowed, since wheel torque becomes insensitive for $\dot{r}_{cvt}$ when passing through r_{zi}.

For a certain combination of shift lines, a ratio trajectory can be created by defining:

$$r_{cvt,d}^{(t+\delta t)} = r_{cvt,d}^{(t)} + \dot{r}_{shift-line}^{(t)}\delta t \qquad \text{where:} \quad \dot{r}_{shift-line} = f(r_{cvt}, T_e) \qquad (7.5)$$

Ratio trajectory will be varied by implementing different combinations of the gains C_1 and C_2 in an attempt to find an optimal combination.

7.2 Simulation in time domain

The drivetrain of figure 6.3 has been modelled in *Simulink*. Hydraulic pump losses as well as mechanical losses are taken into account (see appendix H). Since little efficiency data is available for the Aisin transmission, values measured in a different CVT are used [10]. A road-load characteristic, representing tire rolling resistance and air drag, has been measured in the test vehicle (appendix H).

Figure 7.5 shows simulation results for three different values of C_1, while keeping C_2 constant. A stationary driving speed of 80 km/h is assumed at the start of the simulation. At t=2 a kick down is initiated. The various engine accelerations are displayed in figure 7.5(b). The resulting wheel torque responses show differences in initial torque and in time needed to reach the final level.

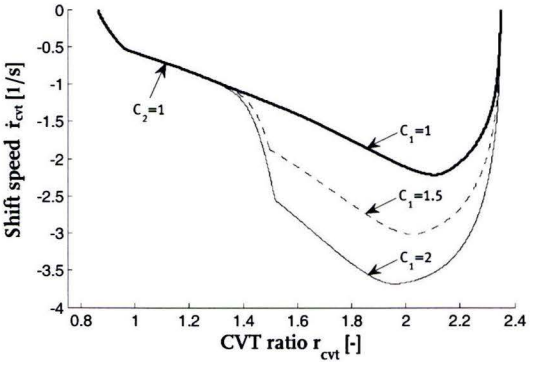

Figure 7.5(a): simulation of different C_1-values, ratio and shift speed

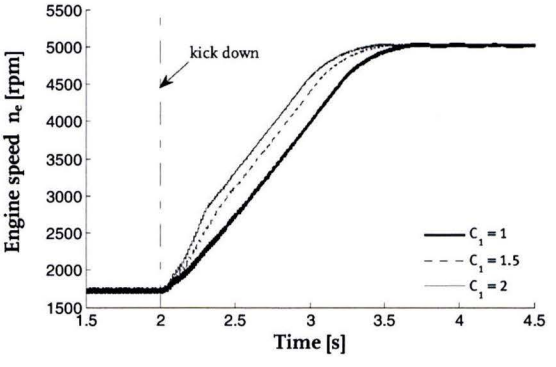

Figure 7.5(b): simulation of different C_1-values, engine speed transient

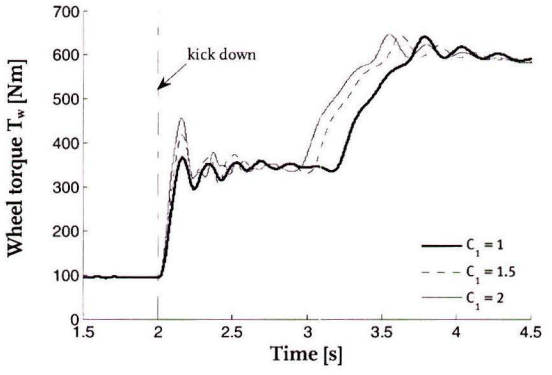

Figure 7.5(c): simulation of different C_1-values, wheel torque

The same analysis is done for parameter C_2, see figure 7.6. Here differences are seen in the second part of the transient. High shift speed below Zero Inertia ratio causes wheel torque to remain constant during a large part of the transient, before quickly rising to its final level. Low shift speeds in this range result in a continuously rising torque. However, time to reach the final level increases.

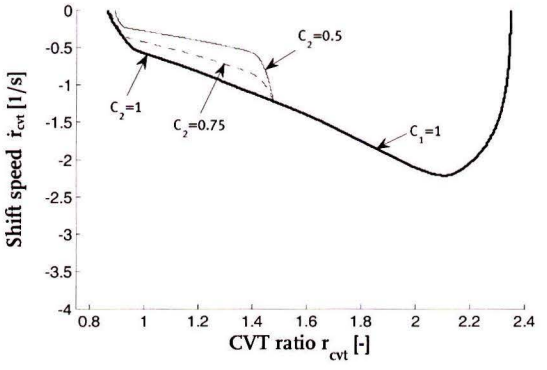

Figure 7.6(a): simulation of different C_2-values, ratio and shift speed

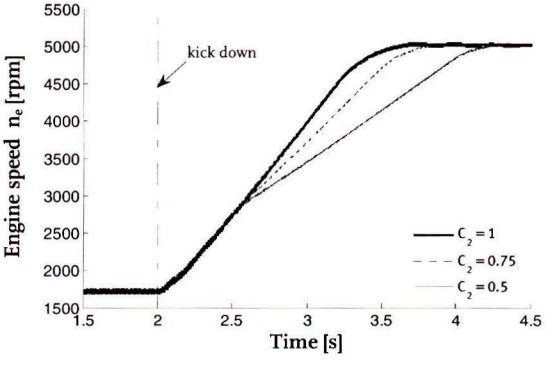

Figure 7.6(b): simulation of different C_2-values, engine speed transient

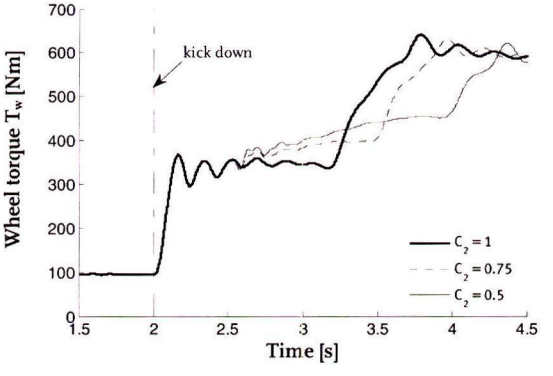

Figure 7.6(c): simulation of different C_2-values, wheel torque

From these simulations, it is expected that the combination of a high value for C_1 (close to 2) in combination with an average value for C_2 (close to 0.75) could deliver good results. Testing in the vehicle will have to show which wheel torque shape is preferred by the driver.

7.3 Experimental validation of Zero Inertia shifting

For testing in the vehicle the control structure of figure 7.7 has been implemented. Vehicle speed and accelerator pedal position act as inputs for the DPT map, resulting in a desired power output. The Zero Inertia control locates the desired power on either the E-line or the WOT-line and determines the desired engine speed and torque. This automatically leads to a desired CVT ratio. Ratio trajectory is shaped using the method described in paragraph 7.2. In order to avoid negative flywheel speeds during deep downshifts, the impulse start clutch is controlled to open and close when crossing geared-neutral ratio.

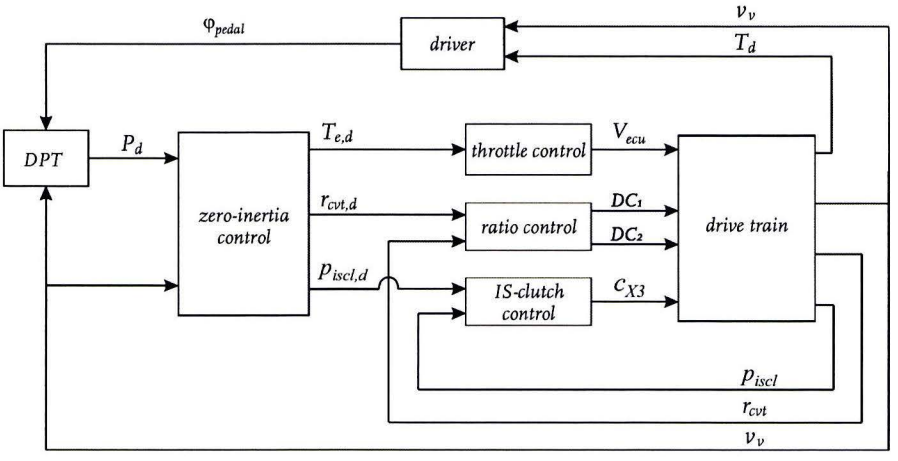

Figure 7.7: layout of Zero Inertia control

On component level, the CVT ratio is controlled by actuating the primary pulley flow valve. The controller comprises a model-based feed-forward in combination with PID-feedback of the measured ratio. The output is a 40 Hz duty-cycle signal that actuates two hydraulic pilot valves. Both pilots operate the main primary flow valve. The impulse start clutch is controlled with a proportional pressure valve. The controller comprises feed-forward of its stationary characteristic in combination with PI-feedback of the measured pressure. The output is a voltage signal leading to a valve amplifier, which generates a current for the proportional pressure valve. Finally, engine torque is steered by an input voltage to the ECU. Measurements have shown a good correlation between this control signal and resulting throttle position.

First, the shift strategy described in paragraph 7.1 is validated by measurements. Figure 7.8 shows two performance downshifts measured with different values for the parameters C_1

and C_2. The black curve represents a downshift with $C_1 = 1.4$ and $C_2 = 0.6$ and the grey curve a downshift with $C_1 = C_2 = 1$.

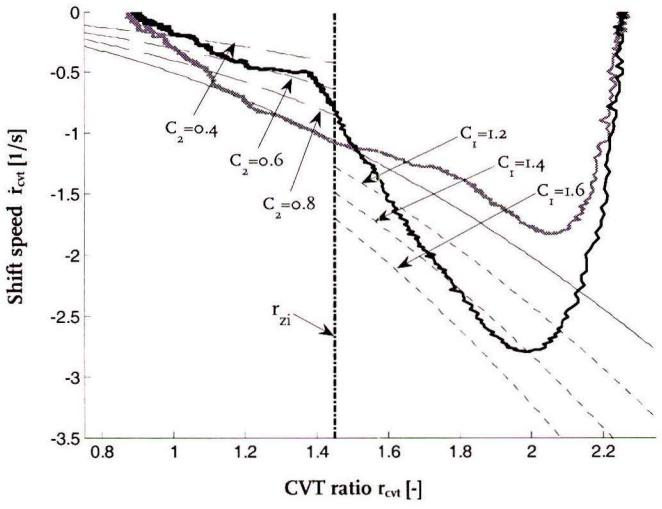

Figure 7.8: measured shift trajectory's with different values for C_1 and C_2

The corresponding wheel torque responses are displayed in figure 7.9. It is seen that the initial fast shift results in a faster wheel torque response as well a higher torque level. Below r_{zi} the lower shift speed also results in a torque advantage. Therefore, the high C_2-value in combination with a low C_1-value proves to deliver good results.

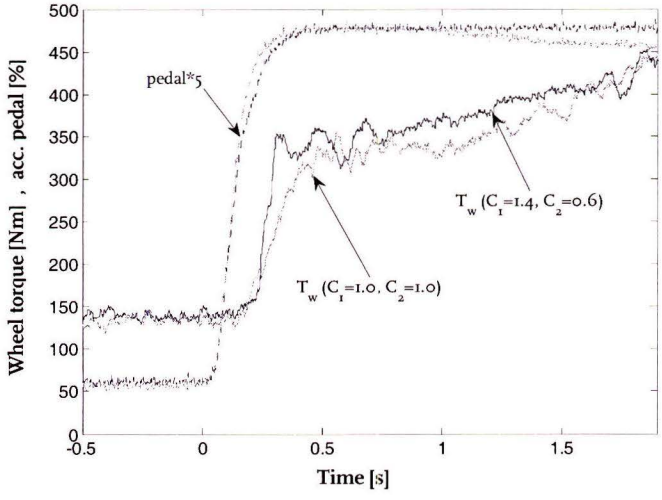

Figure 7.9: measured wheel torque response for different values for C_1 and C_2

Kick down measurements have been done at speeds ranging from 60 to 90 km/h. Resulting wheel torque response will be compared to that measured in the reference vehicle. Figure 7.10 shows a Zero Inertia kick down measurement done at 80 km/h.

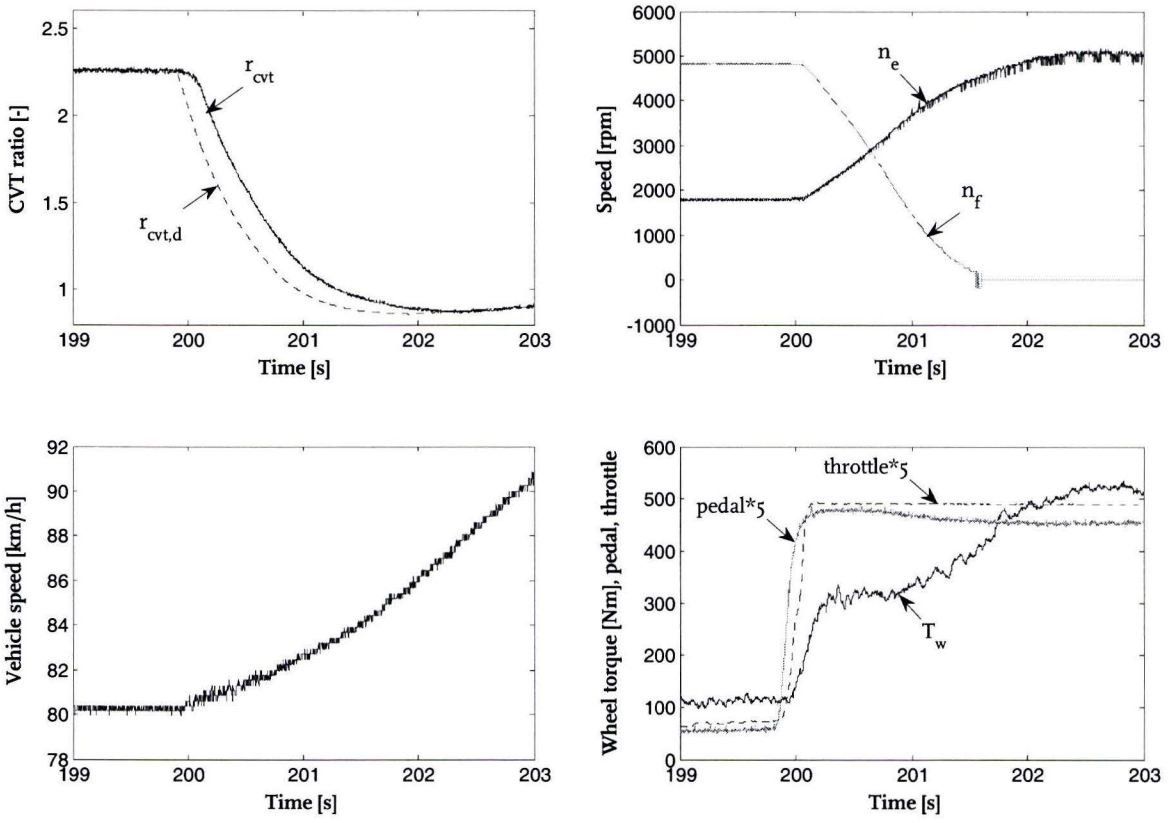

Figure 7.10: measurement of a Zero Inertia kick down at 80 km/h

The delay of wheel torque increase after pedal depression is approximately 0.2 seconds. Wheel torque remains virtually constant until Zero Inertia ratio is reached. The initial wheel torque ramp is a result of variator response time. It takes 0.25 seconds for the variator to reach the desired shift speed level. Below Zero Inertia ratio engine acceleration is slowly decreased, resulting in a further wheel torque increase. When geared-neutral ratio is reached the IS²-flywheel is disconnected by opening the impulse start clutch.

Figure 7.11 shows a similar measurement done in the reference vehicle with the conventional CVT. During this measurement the conventional Toyota controls were still active. Toyota has chosen a different shift strategy, resulting in a fast engine acceleration until 3400 rpm, after which shift speed is reduced considerably. During the initial fast shift action, a sag phenomenon is seen. Instead of instantly rising to a higher level, wheel torque drops almost to zero. Not only does this result in a delayed acceleration response, it even causes vehicle acceleration to become negative for a short period. The final torque level is lower than that seen in the Zero Inertia measurement. This is a direct result of the Toyota shift strategy which does not reach ratio's below medium.

Comparing figures 7.10 and 7.11, it is seen that at the end of the 3 second kick down timeframe, vehicle speed has increased by 10 km/h for the IS²-CVT and only 8 km/h for the conventional CVT.

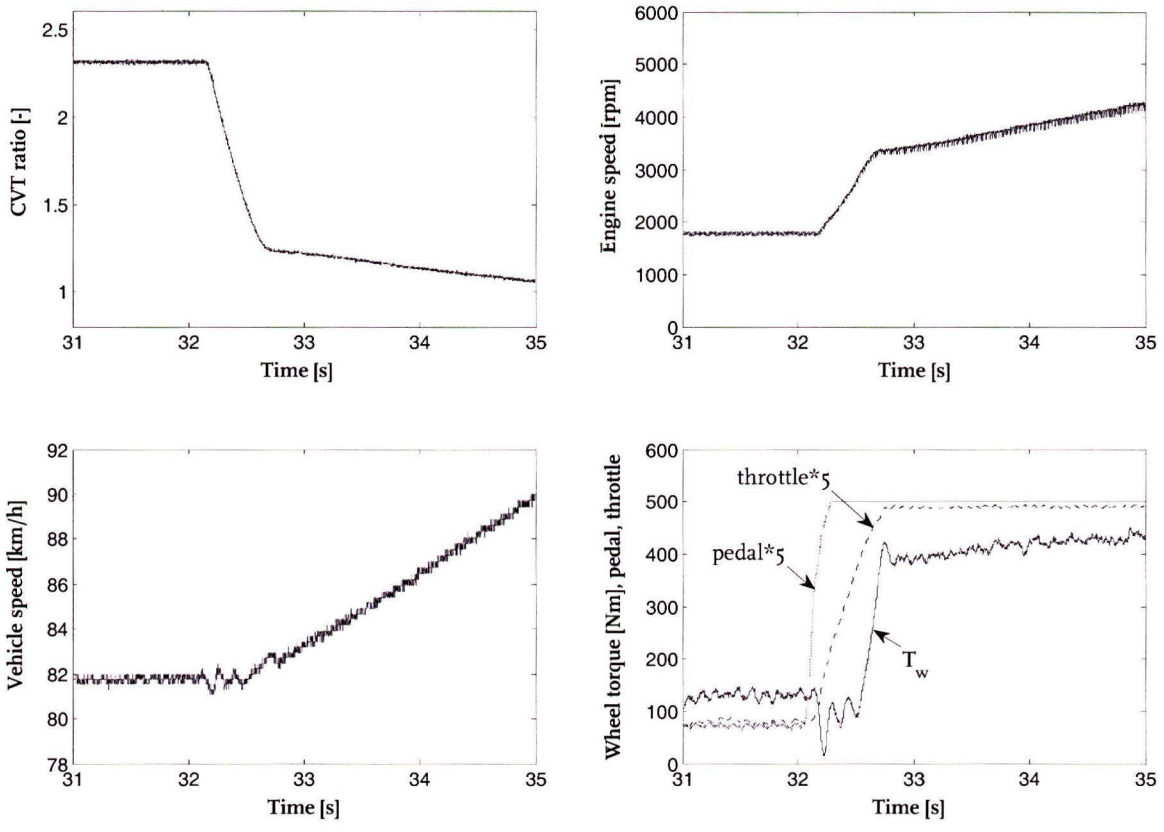

Figure 7.11: measurement of a kick down with the conventional CVT and Toyota controls at 80 km/h

Various tests have been done to tune the kick down wheel torque response according to the findings in paragraph 7.2. A collection of achieved wheel torque curves is shown in figure 7.12. The wheel torque response of the conventional CVT is also shown.

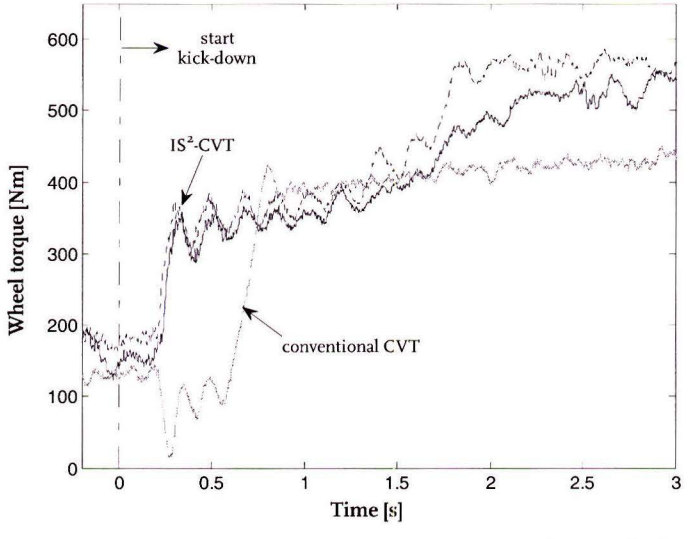

Figure 7.12: wheel torque responses during kick down at 80 km/h

7.4 Experimental validation of impulse shifting

Although previous analyses have shown that impulse shifting would not yield a performance improvement in case of the Toyota Vitz test vehicle, it may well be used to eliminate the initial variator response delay seen during Zero Inertia shifting. By instantly opening the drive clutch when a kick down is detected wheel torque should be available with minimal delay. To investigate this potential, Impulse Shift controls have been implemented in the control software (figure 7.13).

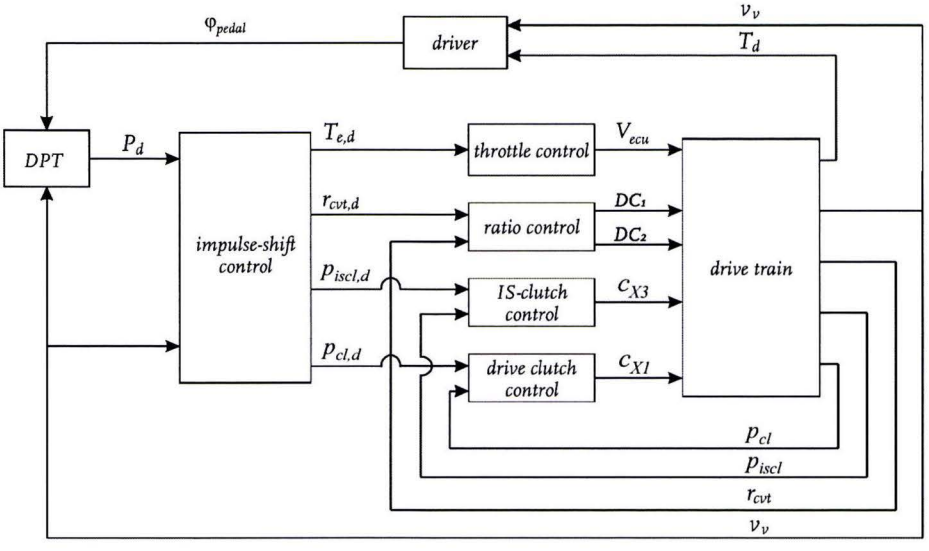

Figure 7.13: layout of Impulse Shift control

The control layout is quite similar to that of Zero Inertia shifting. One extra output is needed for controlling drive clutch pressure. The proportional pressure valve used is identical to the one used for the impulse start clutch. It is controlled by means of feed-forward of its stationary characteristic and PI-feedback of the measured clutch pressure.
Two different control strategies are tested. First, the drive clutch remains open until the variator has passed Zero Inertia ratio. Next, a much shorter clutch opening period is tried, purely covering the variator shift delay.

Figure 7.14 shows an Impulse Shift measurement in which the drive clutch remains open for approximately 1 second. The speed difference over the drive clutch remains fairly small, this is a direct result of the generated ratio trajectory. Initial wheel torque delay has been reduced to 0.13 second, instead of 0.25 seconds seen during Zero Inertia shifting. As expected, the drive clutch response is faster than the variator response. Synchronization of the drive clutch below Zero Inertia ratio is not completely smooth as a small jerk-effect can be seen in the wheel torque at this time. Final wheel torque level is higher than in previous measurements, which is caused by a somewhat lower vehicle speed during this measurement.

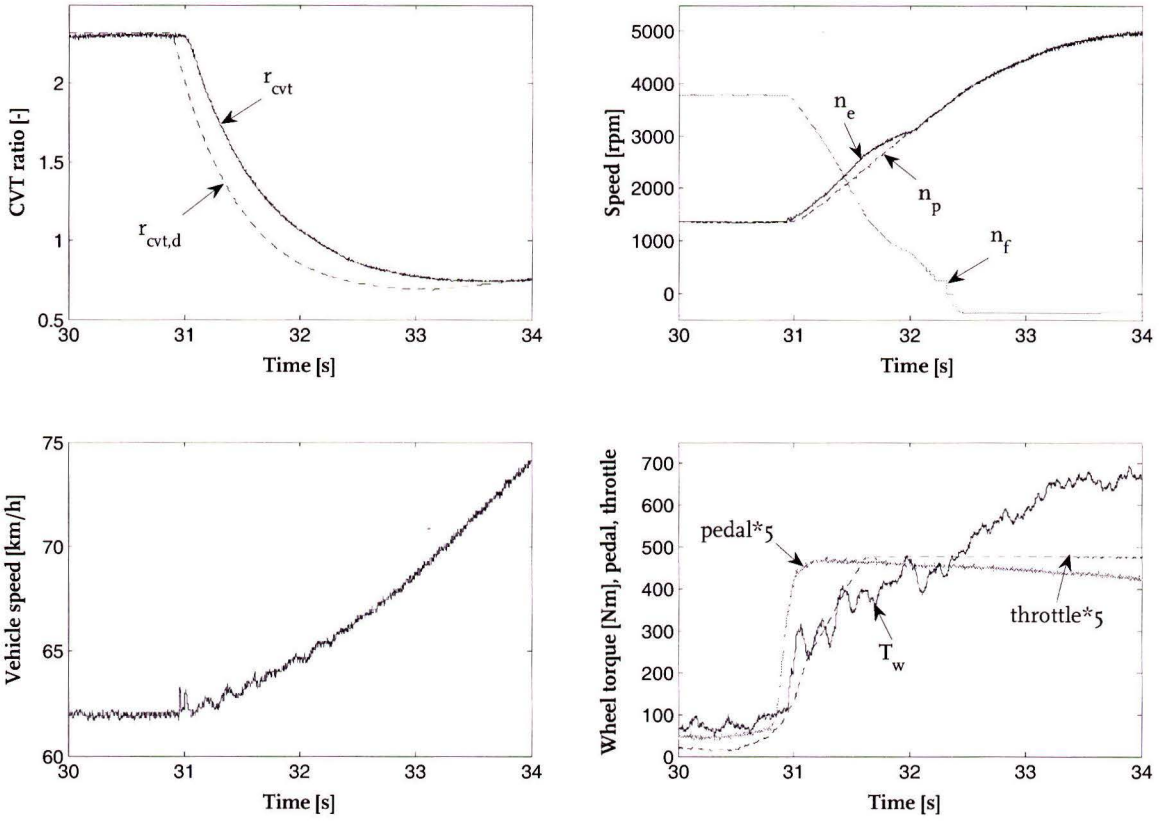

Figure 7.14: measured Impulse Shift kick down at 62 km/h, drive clutch open for 1 second

In figure 7.15 a different strategy is tried, in which the drive clutch is opened only during the initial variator delay. In the upper right figure, it can be seen that the drive clutch is opened for only 0.4 seconds. This strategy is basically a combination of Zero Inertia and Impulse shifting. Once the drive clutch is closed again, the variator shift speed is at its desired value, after which the remaining downshift is completed in Zero Inertia mode.

Although the initial wheel torque delay is reduced by opening the drive clutch, no significant performance increase is made by using the Impulse Shift control strategy, being in accordance with previous analyses. A different choice in design parameters, for example other values for flywheel inertia and geared-neutral ratio, could improve the Impulse Shift performance. Engine flywheel inertia might also be chosen lower, as the IS²-flywheel also helps in reducing transmission vibrations.
The same is true for Zero Inertia shifting. Although the realized kick down performance is already quite good, other design parameters could further improve acceleration response. In case of the Toyota Vitz test vehicle, packaging constraints have limited the design freedom. For future designs, it is recommended to choose a lower Zero Inertia ratio if possible. The current value of r_{zi} = 1.45 is reached quite soon during a performance downshift. A lower value, towards medium, would present much more freedom in shaping the wheel torque response.

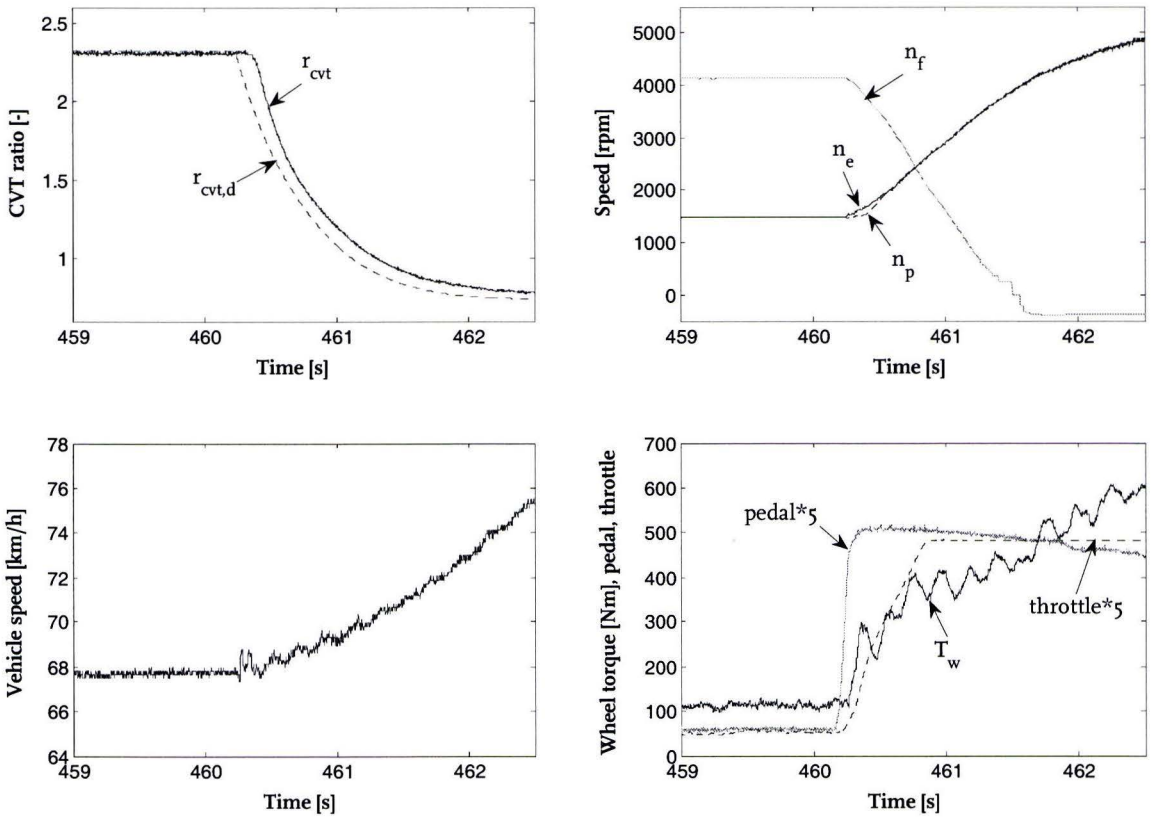

Figure 7.15: measured Impulse Shift kick down at 68 km/h, drive clutch open only during variator delay

Chapter 8

Fuel consumption measurements

Adaptations made to the conventional Aisin CVT are expected to have a considerable impact on fuel economy. Overall, four changes have been made that are meant to effect fuel consumption:

- idle-stop function has been enabled by impulse starting (- 12 %)
- the pushbelt has been replaced by a more efficient involute chain (- 5 %)
- the torque converter has been replaced by a wet plate launch clutch (- 2 %)
- improvements in engine operating point by early upshifting strategy (- 3 %)

The percentages between the brackets represent the target value for each adaptation. The largest step in fuel consumption reduction should be made by the idle-stop functionality. In all, a combined saving potential of 20% is aimed for. To enable a good comparison between the reference and the adapted transmission, measurements are performed under standardized conditions. This means measuring a drive cycle on a calibrated roller bench, after a warm-up procedure. Because the adaptations are most effective during city driving, the Japanese 10/15 drive cycle was selected.

8.1 Measurement with the conventional CVT

The conventional CVT with torque converter, pushbelt and Toyota controls was tested first. In figure 8.1 a number of relevant signals measured on the JP10/15 drive cycle are displayed.

In the first graph both the reference and driven speed profiles are displayed. A deviation of ± 2 km/h is allowed when driving constant speed. During speed transients a larger deviation is allowed (± 5 km/h). In the second graph the CVT ratio realized by Toyota transmission controls is shown. Note that overdrive ratio is only achieved during the final section of the drive cycle. Measured engine speed is displayed in the third graph. Measured fuel mass flow is displayed in the bottom graph. The duty-cycle of the first cylinder injector is measured. Its fuel mass flow has been calibrated for various duty-cycles and pressure differences over the injector. The latter is necessary to compensate for pressure changes in the intake manifold.

By integrating the fuel mass flow over the complete cycle and dividing it by the travelled distance, a fuel consumption figure can be determined. These results are presented in paragraph 8.3, where the conventional and IS²-CVT drivetrains are compared.

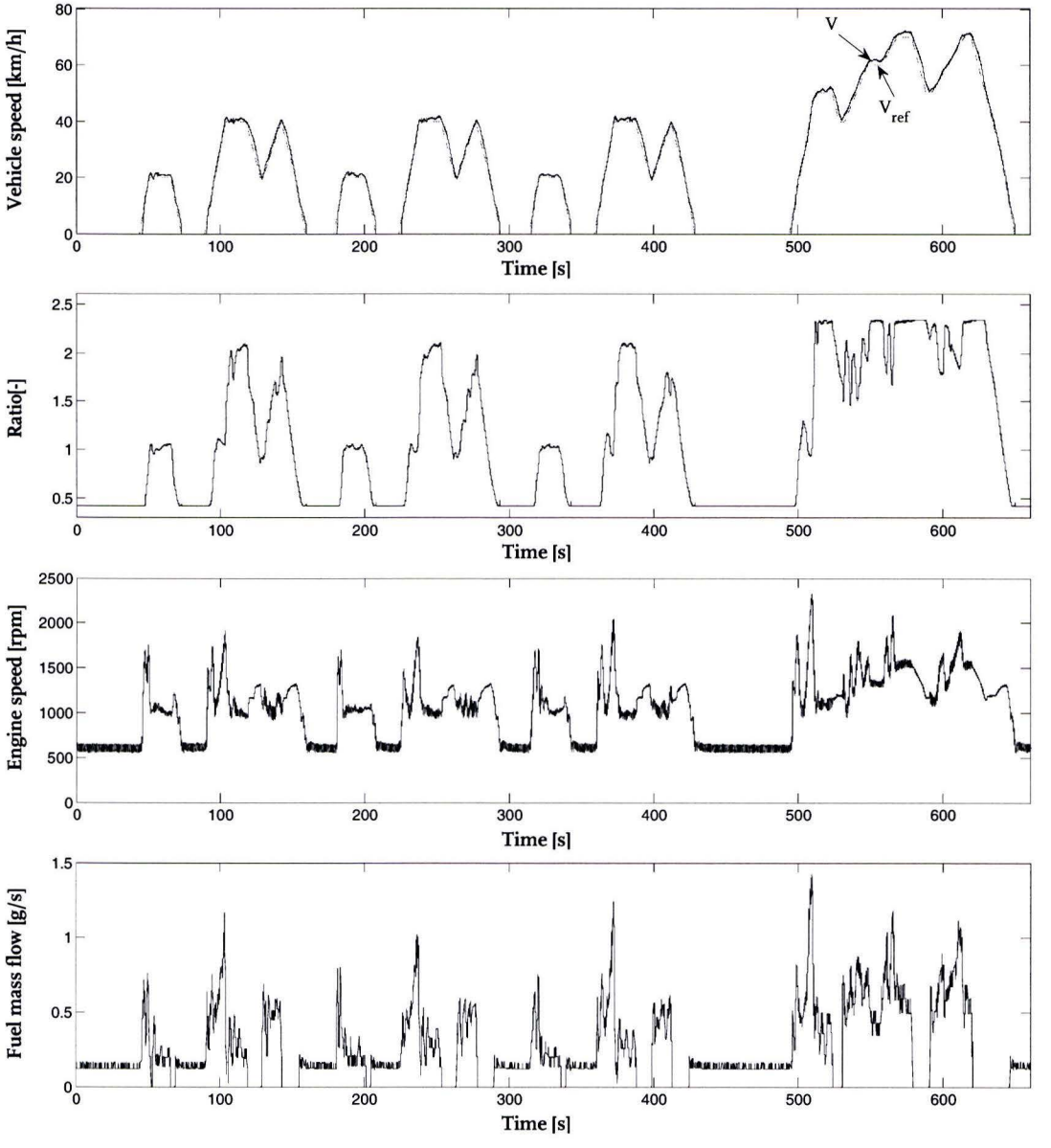

Figure 8.1: measured Japan 10/15 drive cycle with conventional CVT

8.2 Measurement with the IS²-CVT

The Japanese 10/15 drive cycle has also been driven with the IS²-CVT, see figure 8.2. Two additional signals are displayed, being the desired CVT ratio and IS²-flywheel speed. Both vehicle speed tracking as well as ratio tracking are acceptable as can be seen in both upper

graphs. Impulse starting is fully functional during the measurement. This means that the engine is shutdown during each vehicle standstill period, after disconnecting the flywheel at a high state of charge.

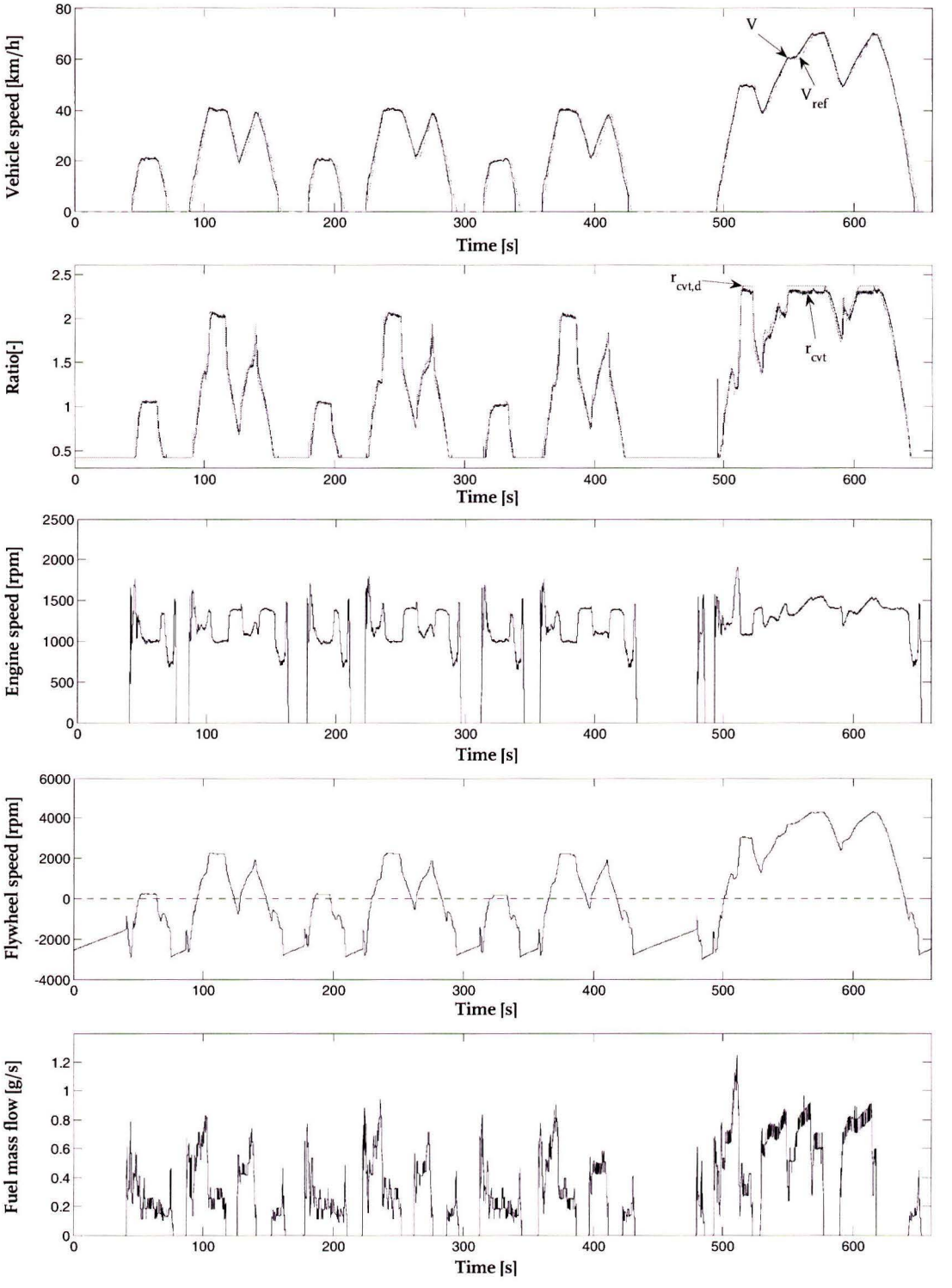

Figure 8.2: measured JP 10/15 drive cycle with IS²-CVT, including Impulse Start functionality

Flywheel coast down rate resulting from frictional losses is too high to bridge the standstill period at t = 430, which requires a shutdown duration of 65 seconds. One additional Impulse Start is needed in this case.

8.3 Fuel consumption savings

The measured fuel mass flow in the bottom graphs of figure 8.1 and 8.2 can be integrated to find the total amount of fuel consumed, see figure 8.3. For the conventional CVT a total fuel consumption of 169.6 grams is found. The IS²-CVT shows 159.4 grams, a reduction of 10.2 grams.

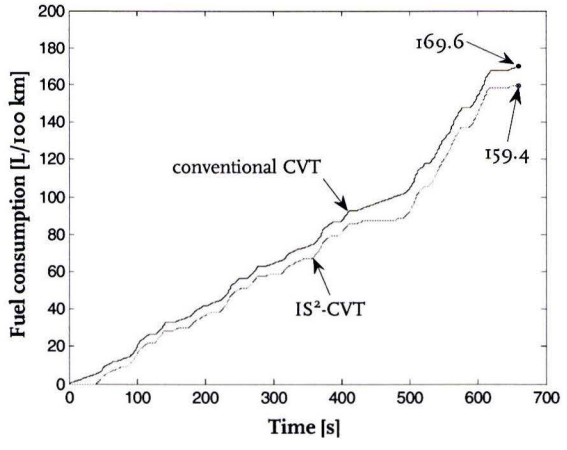

Figure 8.3: consumed fuel in grams

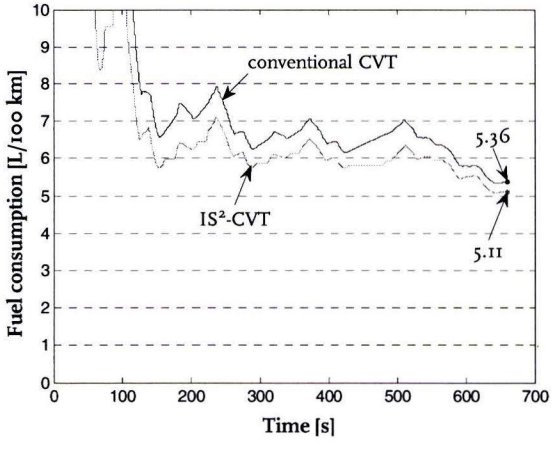

Figure 8.4: fuel consumption in litres per 100 km

The idle fuel consumption of the test vehicle is measured to be 0,097 g/s. On the JP10/15 drive cycle a total standstill time of 207 seconds is seen. This leads to a theoretical idle-stop saving potential of approximately 20 grams. Compared to the conventional CVT this equals 11.8 %.

Figure 8.4 shows the fuel consumption expressed in litres per 100 km. The final value for the conventional CVT is 5.36 L/100 km and 5.11 L/100 km for the IS²-CVT, corresponding to a reduction of 4.7%. This figure is much lower than the initial target of 20%. The difference can be explained by the following:

i. the intended early upshift strategy was already implemented by Toyota, leaving little room for improvement. Therefore the intended 3 % reduction has not been achieved.
ii. intermediate fuel consumption measurements in which only the pushbelt was replaced by an involute chain have shown a reduction of 3 % caused by the chain, instead of the expected 5 %.

iii. additional frictional losses caused by added gears, rotating seals and the IS²-flywheel result in a 2% fuel consumption increase. This increase is found when driving the JP 10/15 cycle with and without connecting the IS²-flywheel.

iv. engine fuel cut-off on the 20 - 0 km/h transients is currently not operational. Measurements with the conventional CVT with Toyota controls show that the ECU closes the injectors during these transients. It is expected that this is an unwanted side effect of taking over transmission controls from the ECU. The result is an additional fuel consumption of 1 %.

v. during the 65 second standstill period at the end of the cycle an extra Impulse Start is needed because flywheel speed becomes critical. This unavoidable action increases overall fuel consumption by approximately 1 %.

vi. the savings realized with idle-stop can be further optimised. During current measurements, the control strategy was such the IS²-flywheel was charged by the engine after coming to a complete standstill. This reduces the idle-stop saving potential. A different strategy is possible where the flywheel is charged during vehicle coast down, enabling an earlier engine shutdown. This requires a higher engine speed during coast down however. Individual tests on the road have shown that an additional 5 % of fuel can be saved by implementing this strategy. It has not been verified on a full drive cycle however.
The lack of control over the ECU during engine restarts causes the engine to accelerate itself to a high speed level, which is not strictly necessary. By intervening in the ECU during restarts, additional fuel can be saved.

With respect to the last two points, it is recommended to implement an additional (electric) assist device on the IS²-flywheel in future designs. A small electric device, with a power rating as low as 50 Watt (see figure 5.13,)would suffice to keep the IS²-flywheel at a speed level suitable for impulse starting:

$$P_{assist} = J_f \dot{\omega}_f \omega_f \approx 0.082 \cdot 3 \cdot 200 = 50 \quad [W] \tag{8.1}$$

By doing this, the engine can be stopped even sooner and the shutdown period is no longer limited to one minute. This would also eliminate the extra start needed during the 65 second standstill period.

With the current IS²-hardware a fuel consumption improvement of 12% should be possible, if the problems described in point iv and v can be avoided. This final saving potential is based on individual tests with improved Impulse Start controls. It has yet to be validated by new measurements on the roller bench however.

Chapter 9

Conclusions and recommendations

9.1 Conclusions

All functionalities of the IS²-CVT have been modelled, analysed and later validated in the test vehicle. Both the vibration isolating properties of the IS²-flywheel as well as problematic eigenmodes have been identified. The idle-stop functionality enabled by *Impulse Starting* has been successfully implemented in the vehicle. Restarting of the combustion engine proves to be very robust. A performance comparison between *Impulse Shifting* and *Zero Inertia* shifting has been made. Both strategy's show a large improvement in acceleration response compared to the reference vehicle. In case of the Toyota Vitz test vehicle, the Zero Inertia strategy proved to deliver the best results. Finally, fuel consumption measurements performed on the Japanese 10/15 drive cycle have shown an improvement over the reference vehicle. The initial fuel saving targets were not fully accomplished however.

Modelling of the dynamic behaviour of the IS²-CVT provided the basis for a drivetrain vibration analysis. It was shown that the additional IS²-flywheel provides extra vibration suppression over a large part of the CVT's ratio range. In ratio's close to low and overdrive, vibration suppression is most effective. In geared-neutral ratio, where the flywheel is at standstill, no additional vibration suppression is seen. Beside these favourable isolating properties, a problematic eigenmode was discovered. When unable to disconnect the flywheel form the drive train, which is the case during one intermediate construction phase, an eigenmode comparable to that of dual-mass flywheel systems is seen. Unacceptably large torsion damper angles during engine start have been predicted, which would lead to possible failure of the torsion damper. A temporary solution was found in the form of adding dry friction to the torsion damper. Testing in the vehicle showed that this solution was sufficient to prevent mechanical damage to occur.

A theoretical analysis of the Impulse Start functionality was performed. It was stated that the combustion engine would need to be restarted in 150 ms, cranking it to at least 600 rpm. Simulations resulted in a range of acceptable flywheel speed levels and clutch closing rates with which these two criteria are met. The influence of the initial crankshaft position was also investigated. It was concluded that the sensitivity of the initial crankshaft position on impulse starting is fairly small. A strategy for releasing the IS²-flywheel at a high state of

charge was developed, thereby optimising maximum engine shutdown time. During impulse starting a reaction torque at the wheels occurs, causing the vehicle to shortly move backwards. Two possible solutions have subsequently been compared in simulation. The solution using a pawl to connect the secondary pulley to the transmission housing was finally implemented in the vehicle.
Identification of components and initial testing of control strategies was performed on the test stand. Finally, the Impulse Start functionality was successfully tested in the vehicle and integrated in the coordinated control.

A downshift performance analysis comparing Zero Inertia and Impulse Shift strategy was performed. It was concluded that in case high shift speeds can be achieved, Zero Inertia strategy provides the best performance. Above Zero Inertia ratio shift speed may be maximized, leading to the highest initial acceleration and minimizing the time needed to reach the final target ratio.
Since the CVT of the Toyota Vitz test vehicle is able to reach high shift speeds, the Zero Inertia strategy has been implemented in the control software. A ratio set point generation tool has been created, based on the earlier performance analysis. Simulations in the time domain have illustrated the influence of different settings of the set point generation tool. Experimental validation of the Zero Inertia shift strategy was performed in the test vehicle. A large improvement in acceleration performance over the conventional CVT was successfully demonstrated. Earlier conclusions regarding the Impulse Shift strategy have also been validated in the vehicle. A small advantage in wheel torque response time was seen over Zero Inertia strategy. Despite this advantage, overall performance of Zero Inertia shifting proved to be best.

A target fuel consumption improvement of 20 % over the conventional vehicle was aimed for. Measurements of the Japanese 10/15 drive cycle performed on the roller bench resulted in a 4.7 % improvement. Savings resulting from the gear chain, early upshifting and impulse starting were less than initially assumed. The Impulse Start strategy during these measurements was far from optimal however. Later individual measurements on the road suggest that a further improvement of 5 % is possible by shutting the engine down earlier. This improved start-stop strategy has yet to be validated on the 10/15 drive cycle. Along with a few more small improvements, a consolidated improvement of nearly 12 % is deemed possible .

9.2 Recommendations and future work

During testing of the Impulse Start functionality a number of possible improvements for later designs arose. The wet environment in which the IS^2-flywheel rotates causes large frictional losses to occur. As a result, flywheel coast down time is penalized. Furthermore, optimisation of bearing losses could also improve coast down times. A different choice in design parameters could enable larger negative flywheel speeds to be reached during vehicle coast downs. Adding a small electric assist device to the flywheel would be a solution for all issues mentioned above.

The controllability of the Impulse Start clutch proved to be insufficient with respect to response time. Since oil leaks out of the plunger chamber, a time delay of 0.3 seconds is seen when an Impulse Start is initiated. For future designs, a closed actuation circuit is proposed.
The reaction torque acting on the secondary drive train during Impulse Starts should also be avoided in future designs. The current park pawl solution is far from perfect, as it difficult to guarantee a successful engagement of the pawl. Another drawback of the current design is the fact that the torque path during impulse starting goes through the torsion damper, winding it up in negative direction. Since the conventional torsion damper is not designed for large negative torques, this leads to unnecessary impacts and possible mechanical damage. A solution to these two issues would be to position the impulse start clutch directly in between the IS²-flywheel and the engine flywheel.

Downshift performance of the test vehicle was improved significantly. However, an optimisation of design parameters could lead to further improvement of initial acceleration response. The current Zero Inertia ratio (r_{zi} = 1.46) might be a bit too high. By choosing a larger value for the flywheel inertia or a planetary gear ratio that enables higher flywheel speeds, the ZI ratio can be lowered. Because of packaging constraints in the Aisin CVT, little improvement is deemed possible for the current test vehicle. Very low values for the ZI ratio are not desired either, since this is likely to result in a very large and heavy flywheel unit. This was the case during the *EcoDrive* project, where a ZI ratio of 0.95 was realized.

Fuel consumption figures can be further improved by optimising flywheel coast down time. This would avoid the extra start during the long standstill period on the 10/15 cycle. Further improvements are possible by enabling more control over the engine management, which is currently fully in the hands of the ECU. Engine torque output control is currently not accurate enough to ensure optimal E-line operation under all circumstances. Direct throttle control, instead of indirect control by means of a faked accelerator pedal signal, could be a solution. Another unwanted phenomenon is the high engine speed seen after impulse starting. This is also a direct result of a lack of control over the ECU. Reducing post-start engine speeds to a range close to 1000 rpm could save additional fuel. As an intermediate solution this could be realized by actuating the launch clutch a bit earlier and stronger after impulse starting.

Bibliography

[1] Cock, J.D.W. de: Vibration Analysis and Synthesis of the Brake/Impulse Shift Transmission Technology, Master Thesis DCT 2004-097, Technische Universiteit Eindhoven, 2004

[2] Druten van, R.M.: Transmission design of the Zero Inertia powertrain, Ph. D. Thesis, Technische Universiteit Eindhoven, 2001

[3] Lechner, G., Naunheimer, H.: Automotive transmissions, Fundamentals, Selection, Design and Application, Springer, 1999

[4] Karnopp, D.C.; Margolis, D.L.; Rosenberg, R.C.: System Dynamics: A Unified Approach, Wiley-Interscience, New York, 1990

[5] Pacejka, H.B.: Tyre and Vehicle Dynamics, Butterworth Heinemann, 2002

[6] Pulkrabek W.W.: Engineering Fundamentals of the Internal Combustion Engine, Pearson Prentice Hall, 1997

[7] Reik, W.; *et. al.*: Das Zweimassenschwunrad, 6. LuK Kolloquium, pp 69-94, 1998

[8] Römers, L.H.J.: Automatic Generation of Combustion Engine Models using MatLab, Traineeship report DCT 2006-038, Technische Universiteit Eindhoven, 2006

[9] Rooij, J. van: The GCI High Torque CVT Chain for Torques up to 2500 Nm, International Congress on Continuously Variable and Hybrid Transmissions, Yokohama, 2007

[10] Serrarens, A.F.A.: Coordinated control of the Zero Inertia powertrain, Ph. D. Thesis, Technische Universiteit Eindhoven, 2001

[11] Vroemen, B.G.: Component control for the Zero Inertia powertrain, Ph. D. Thesis, Technische Universiteit Eindhoven, 2001

Appendix A

Abbreviations and symbols

Abbreviations

AMT	Automated Manual Transmission
AT	Automatic Transmission
BSFC	Brake Specific Fuel Consumption [g/kWh]
CVT	Continuously Variable Transmission
DCT	Dual-Clutch Transmission
DMF	Dual-Mass Flywheel
DNR	Drive-Neutral-Reverse
DPT	Driver Pedal Translation
ECU	Engine Control Unit
E-line	collection of fuel-optimal engine operating points
IS^2	Impulse Shift and Impulse Start
MT	Manual Transmission
NEDC	New European Driving Cycle
WOT	Wide Open Throttle
ZI	Zero Inertia

Symbols - Greek

Symbol	Definition	Value [Unit]
α	road surface inclination angle	[rad]
α_p	torque amplification from flywheel to primary side	1.92 [-]
α_s	torque amplification from flywheel to secondary side	2.04 [-]
γ	torque amplification from engine to secondary side	0.754[-]
ε	engine compression ratio	10.5 [-]
ϕ	relative slip of tire contact surface	[-]
φ_e	crankshaft angular position	[rad]
φ_{pedal}	accelerator pedal angle	[rad]
φ_s	secondary angular position	[rad]
φ_t	torsion damper angular position	[rad]
φ_w	wheel angular position	[rad]
κ	isentropic coefficient	1.35 [-]

λ	crank radius / connection rod ratio	0.3 [-]
μ	tire friction coefficient	[-]
ρ	air density	1.29 [kg/m^3]
$\omega_{annulus}$	annulus gear angular speed	[rad/s]
$\omega_{carrier}$	carrier gear angular speed	[rad/s]
ω_e	engine angular speed	[rad/s]
$\omega_{e,d}$	desired engine speed	[rad/s]
ω_f	IS^2-flywheel angular speed	[rad/s]
ω_h	transmission housing angular speed	[rad/s]
ω_p	primary pulley angular speed	[rad/s]
$\omega_{p,d}$	desired primary pulley speed	[rad/s]
ω_s	secondary pulley angular speed	[rad/s]
ω_t	torsion damper angular speed	[rad/s]
ω_{sun}	sun gear angular speed	[rad/s]
ω_v	vehicle angular speed	[rad/s]
ω_w	angular wheel speed	[rad/s]

Symbols - Roman

Symbol	Definition	Value [Unit]
A_v	vehicle frontal area	[m^2]
b_d	drive shaft damping coefficient	0.5 [Nm s/rad]
b_m	engine mounts damping coefficient	130 [Nm s/rad]
b_{td}	torsion damper damping coefficient	0.5 [Nm s/rad]
b_w	tire slip stiffness	[-]
c_w	air drag coefficient	[-]
c_{x1}	control output for proportional pressure valve x_1	[V]
c_{x3}	control output for proportional pressure valve x_3	[V]
d	piston diameter	0.075 [m]
DC_1	duty-cycle output for ratio control, pilot valve 1	[%]
DC_2	duty-cycle output for ratio control, pilot valve 2	[%]
e_f	relative kinetic energy of IS^2-flywheel versus vehicle	[-]
e_{pri}	relative kinetic energy of primary inertia's versus vehicle	[-]
E_f	IS^2-flywheel kinetic energy	[J]
E_{pri}	primary inertia's kinetic energy	[J]
E_{veh}	vehicle kinetic energy	[J]
f_{ex}	frequency of main engine excitation order	[Hz]
g	gravitational acceleration	9.81 [m/s^2]
G	gyrator modulus	[Nm s/m]
J_e	engine inertia	0.12 [kgm^2]
J_f	IS^2-flywheel inertia	0.082 [kgm^2]
J_h	transmission housing and engine block inertia	12 [kgm^2]
J_p	primary pulley inertia	0.04 [kgm^2]
J_s	secondary pulley inertia	0.033 [kgm^2]
J_t	torsion damper inertia	0.004 [kgm^2]

J_v	rotational vehicle inertia	92 [kgm^2]
J_w	wheel and tire inertia	1.5 [kgm^2]
k_d	drive shaft stiffness	6000 [Nm/rad]
k_m	engine mount stiffness	$12 \cdot 10^3$ [Nm/rad]
k_{td}	torsion damper stifness	347 [Nm/rad]
m_{osc}	oscillating mass of one cylinder	0.5 [kg]
m_v	vehicle mass	1134 [kg]
N_{cyl}	number of cylinders	4 [-]
n_e	engine speed	[rpm]
$n_{e,min}$	minimum engine speed during driving	980 [rpm]
n_f	flywheel speed	[rpm]
$n_{f,o}$	flywheel speed when initiating impulse start	[rpm]
p_{cl}	launch clutch pressure	[bar]
$p_{cl,d}$	desired launch clutch pressure	[bar]
p_{iscl}	impulse start clutch pressure	[bar]
$p_{iscl,d}$	desired impulse start clutch pressure	[bar]
P_d	desired power output	[W]
r	crank raduis	0.037 [m]
r_{cvt}	CVT ratio	[-]
$r_{cvt,d}$	desired CVT ratio	[-]
r_d	final drive ratio	0.189 [-]
r_{gn}	geared-neutral ratio	0.94 [-]
r_{med}	medium ratio	1.0 [-]
r_{low}	low ratio	0.42 [-]
r_{od}	overdrive ratio	2.34 [-]
r_p	connection gear ratio	1.43 [-]
r_{zi}	zero-inertia ratio	1.45 [-]
R_w	dynamic wheel radius	0.277 [m]
T_{air}	air drag torque	[Nm]
T_a	annulus gear torque	[Nm]
$T_{applied}$	applied clutch torque	[Nm]
T_b	brake disc torque	[Nm]
$T_{belt,p}$	pushbelt/gear chain torque acting on primary pulley	[Nm]
$T_{belt,s}$	pushbelt/gear chain torque acting on secondary pulley	[Nm]
T_c	carrier gear torque	[Nm]
T_{ce}	compression/expansion torque on crankshaft	[Nm]
T_{cl}	launch clutch torque	[Nm]
T_{comb}	combustion torque acting on crankshaft	[Nm]
T_d	drive shaft torque	[Nm]
T_e	engine torque	[Nm]
$T_{e,d}$	desired engine torque	[Nm]
$T_{e,fric}$	engine friction torque	[Nm]
T_f	IS^2-flywheel torque	[Nm]
T_G	gyristor element	[Nm]
T_{grad}	torque resulting form road surface gradient	[Nm]
T_h	torque acting on transmission housing	[Nm]
T_{iscl}	impulse start clutch torque	[Nm]
$T_{Karnopp}$	Karnopp torque for closed clutch	[Nm]

T_{loss}	variator mechanical loss torque	[Nm]
T_{mass}	reciprocating mass torque	[Nm]
T_{pump}	hydraulic pump torque	[Nm]
T_{rl}	road-load torque	[Nm]
T_{roll}	tire rolling loss torque	[Nm]
T_s	sun gear torque	[Nm]
$T_{shift.s}$	shift torque acting on secondary pulley	[Nm]
T_t	tire traction torque	[Nm]
T_{td}	torsion damper torque	[Nm]
v	vehicle speed	[m/s]
V	vehicle speed	[km/h]
V_c	cylinder clearance volume	$3.43 \cdot 10^{-5}$ [m^3]
V_d	cylinder displacement volume	$3.25 \cdot 10^{-4}$ [m^3]
V_{ref}	reference vehicle speed	[km/h]
z	planetary gear ratio	[-]

Appendix B

Modelling of components

In the next paragraphs the modelling of all components shown in the free-body diagram of figure B.1 is described, along with the assumption made.

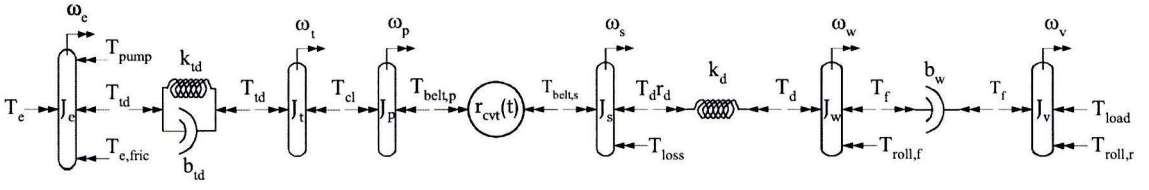

Figure B.1: first construction phase, free-body diagram

B.1 Combustion engine

The dynamic torque over a full 4-stroke cycle (2 crank revolutions) is the sum of three components:

$$T_e(\varphi_e) = T_{ce} + T_{comb} + T_{mass} \tag{B.1}$$

A detailed description of the dynamic engine torque model is presented in appendix C. When engine friction losses and torque needed to drive the hydraulic pump are taken into account, engine acceleration is described by:

$$J_e\dot{\omega}_e = T_e - T_{e,fric} - T_{pump} - T_{td} \tag{B.2}$$

B.2 Torsion damper

The torsion damper is borrowed from the torque converter lock-up disc present in the conventional drivetrain. Its main function is isolating the transmission from engine vibrations. The combined stiffness of the helical spring package has been determined experimentally. Based on experience values, damping has been estimated, which leads to the following parameter values:

$$k_{td} = 347 \quad [Nm/rad] \qquad b_{td} = 0.5 \quad [Nm\ s/rad]$$

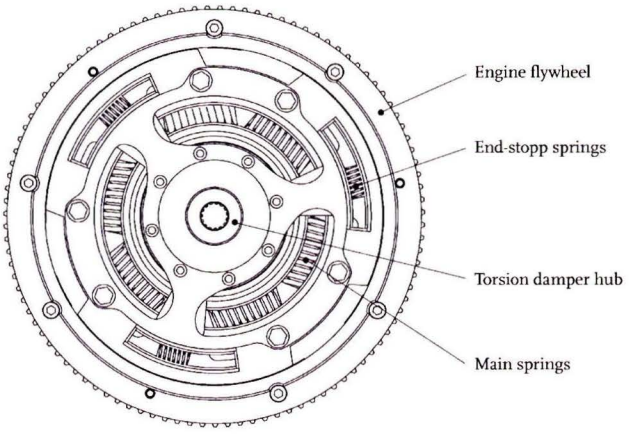

Figure B.2: engine flywheel and torsion damper

The assumption is made that both stiffness and damping are fully linear. Furthermore, no additional friction or backlash is assumed to be present in the torsion damper. Under these assumption the torsion damper reaction torque can be written as:

$$T_{td} = k_{td}(\varphi_t - \varphi_e) + b_{td}(\omega_t - \omega_e) \tag{B.3}$$

Newton's second law for the combined torsion damper and primary input shaft inertia is defined by:

$$J_t \dot{\omega}_t = T_{td} - T_{cl} \tag{B.4}$$

B.3 Launch clutch

The hydraulically actuated wet plate clutch forms the connection between primary input shaft and primary pulley. For a slipping clutch, the transmitted torque is a function of the applied oil pressure and the sign of the speed difference. In a simulation environment this means that an applied torque can be prescribed for as long as there is slip. For a sticking clutch, the dynamic model loses one degree of freedom. To prevent the need to switch between models, a *Karnopp* [4] expression is defined for the sticking clutch. By doing so, the number of degrees of freedom in the model can remain the same as under slip conditions, without causing numerical difficulties. By defining $\dot{\omega}_t = \dot{\omega}_p$, the following expression is found for the Karnopp torque:

$$T_{Karnopp} = \frac{J_t T_{belt,p} + J_p T_{td}}{J_t + J_p} \tag{B.5}$$

The clutch torque for both states can be written as:

$$T_{cl} = \begin{cases} T_{applied} \cdot sign(\omega_t - \omega_p) & \text{for a slipping clutch, in case: } |\omega_t - \omega_p| > \varepsilon \\ T_{Karnopp} & \text{for a sticking clutch, in case: } |\omega_t - \omega_p| \leq \varepsilon \ \wedge \ T_{Karnopp} < T_{applied} \end{cases}$$

B.4 Variator

The variator is modelled as two pulley inertia's connected by a time-dependent ratio. It is assumed that no slip occurs between pulleys and pushbelt (or involute chain). Mechanical losses are taken into account by a friction torque acting on the secondary pulley, see figure B.3(a).

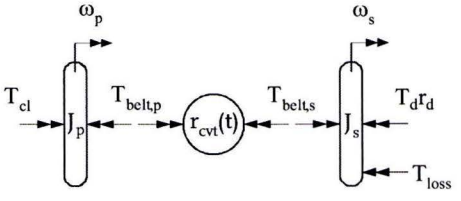

Figure B.3(a): variator dynamics

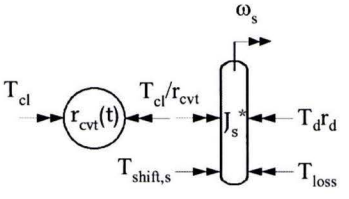

Figure B.3(b): lumped primary pulley

Variator or CVT ratio is defined as secondary divided by primary pulley speed:

$$r_{cvt} = r_{cvt}(t) = \frac{\omega_s}{\omega_p} \tag{B.6}$$

Pushbelt torque acting on the primary pulley is defined as:

$$T_{belt,p} = T_{cl} - J_p \dot{\omega}_p \qquad \text{with:} \qquad \dot{\omega}_p = \frac{\dot{\omega}_s}{r_{cvt}} - \frac{\omega_s}{r_{cvt}^2} \dot{r}_{cvt} \tag{B.7}$$

For the pushbelt torque acting on the secondary pulley follows:

$$T_{belt,s} = \frac{T_{cl}}{r_{cvt}} - J_p \frac{\dot{\omega}_s}{r_{cvt}^2} + J_p \frac{\omega_s}{r_{cvt}^3} \dot{r}_{cvt} \tag{B.8}$$

Having found a definition for the belt torque acting on the secondary pulley, Newton's second law can be written down. Afterwards, primary pulley inertia can be lumped to the secondary variator side, by introducing J_s^* and a shift-speed dependent term $T_{shift,s}$:

$$J_s \dot{\omega}_s = T_{belt,s} - T_d r_d - T_{loss} \tag{B.9}$$

$$J_s^* \dot{\omega}_s = \frac{T_{cl}}{r_{cvt}} + T_{shift,s} - T_d r_d - T_{loss} \tag{B.10}$$

$$\text{with:} \quad J_s^* = J_s + \frac{J_p}{r_{cvt}^2} \qquad T_{shift,s} = J_p \frac{\omega_s}{r_{cvt}^3} \dot{r}_{cvt}$$

B.5 Final drive, differential and drive shafts

Only straight line driving is considered, therefore no differential is modelled. Furthermore, both flexible drive shafts have been lumped into a single linear spring, having stiffness k_d. Backlash effects are not taken into account. The ratio of the combined final drive gear stage corresponds to drive shaft speed divided by secondary pulley speed:

$$r_d = \frac{\omega_d}{\omega_s} \tag{B.11}$$

Damping properties of the flexible drive shafts are assumed to be negligible. Therefore, drive shaft torque acting on the wheels equals:

$$T_d = k_d(\varphi_w - \varphi_s r_d) \qquad k_d = 6000 \quad [Nm/rad] \tag{B.12}$$

B.6 Front wheels and tires

Both wheels have been combined into a single representation, based on the assumption of straight line driving. The traction created between tire and road surface is a modelled as a non-linear function of applied normal force and relative slip between both surfaces. For small slip values, the slip stiffness is virtually linear [5] and the friction coefficient can be written as:

$$\mu(\phi) = b_w \cdot \phi \cdot sign(\omega_w R_w - v) \tag{B.13}$$

Where b_w is the slip stiffness and ϕ is the relative slip of the contact surface. Relative slip is defined for both driving as well as driven wheels:

$$\phi = \begin{cases} 1 - \dfrac{v}{\omega_w R_w} & \textit{in case of driving wheels} \\ 1 - \dfrac{\omega_w R_w}{v} & \textit{in case of driven wheels} \end{cases} \tag{B.14}$$

Wheel traction torque can now be defined as:

$$T_t = m_{v,f} \cdot g \cdot \mu(\phi) \cdot R_w \tag{B.15}$$

When combined with rolling resistance and an applied brake disc torque, front wheel acceleration equals:

$$J_w\dot{\omega}_w = T_d - T_t - T_{r,f} - T_{b,f} \tag{B.16}$$

B.7 Vehicle body, rear wheels and road-load torque

Vehicle body and rear wheels have been lumped into a single inertia, driven by front wheel traction torque. Opposing torques are rear wheel rolling resistance, rear wheel brake torque and the road-load:

$$J_v\dot{\omega}_v = T_t - T_{r,r} - T_{load} - T_{b,r} \qquad J_v = m_v R_w^{\,2} + J_w \tag{B.17}$$

The road-load torque represents the sum of air drag and road surface gradients:

$$T_{load} = T_{air} + T_{grad} = R_w(\tfrac{1}{2}\rho c_w A_v v^2 + m_v g\sin(\alpha)) \tag{B.18}$$

Appendix C

Dynamic engine torque model

The internal combustion machine powering the Toyota Vitz test vehicle is a 4-cylinder gasoline engine (type: 2SZ-FE). It has a displacement volume of 1.3L and is naturally aspirated. A maximum torque output of 121 Nm can be achieved at 4400 rpm and maximum power output of 63 kW is reached at 5500 rpm.

A model of the engine's dynamic torque output, caused by periodic effects taking place in all four cylinders, has been constructed. For each engine operating point, the (gross) dynamic torque output can be constructed from its individual components, being:

- reciprocating mass torque
- compression / expansion torque
- combustion torque

The reciprocating motion of the pistons and connecting rods results in acceleration forces acting on the crank mechanism (figure C.1). The combined gas force acting on each piston can be split into two components, one resulting from compression/expansion and the other from the combustion process. The modelling process of all three components will be described in this appendix. First a single cylinder system will be described, which is later converted into a full engine.

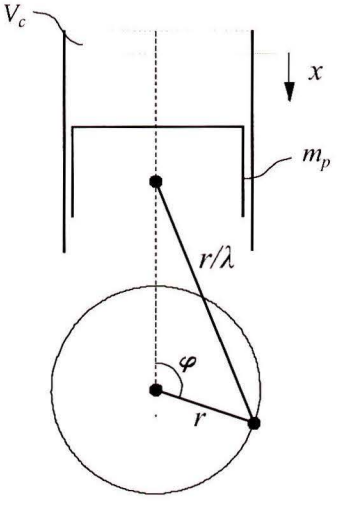

Figure C.1: crank mechanism

C.1 Reciprocating mass torque

The reciprocating mass torque acting on the crankshaft can be derived by writing down the kinematics and dynamics of the piston/crank mechanism. The vertical position of the piston, from top dead centre, can be written as:

$$x(\varphi_e) = r\left((1-\cos(\varphi_e)) + \frac{1}{\lambda}\sqrt{1-\lambda^2 \sin^2(\varphi_e)} \right) \tag{C.1}$$

Where φ_e is the crankshaft angle, r is the crank radius and λ is defined to be crank radius divided by connecting rod length. Equation (C.1) describes the piston position as a function of crank angle. Differentiating it gives an expression for piston velocity:

$$\dot{x}(\varphi_e, \omega_e) = r\,\omega_e \left(\sin(\varphi_e) + \frac{\lambda \sin(2\varphi_e)}{2\sqrt{1-\lambda^2 \sin^2(\varphi_e)}} \right) \tag{C.2}$$

Where ω_e is the crankshaft rotational velocity. Differentiating (C.2) results in an expression for piston acceleration:

$$\begin{aligned} \ddot{x}(\varphi_e, \omega_e) = r\,\omega_e^2 & \left(\cos(\varphi_e) + \frac{\lambda \cos(2\varphi_e)}{\sqrt{1-\lambda^2 \sin^2(\varphi_e)}} + \frac{\lambda^3 \sin^2(2\varphi_e)}{4\left(1-\lambda^2 \sin^2(\varphi_e)\right)^{3/2}} \right) \\ & + r\,\dot{\omega}_e \left(\sin(\varphi_e) + \frac{\lambda \sin(2\varphi_e)}{2\sqrt{1-\lambda^2 \sin^2(\varphi_e)}} \right) \end{aligned} \tag{C.3}$$

Now Newton's second law is used to find the corresponding force acting on the piston. According to [1], the reciprocating mass can be estimated by adding up the piston mass and one-third of the connecting rod mass:

$$F_p = -m_{reci}\,\ddot{x}(\varphi_e, \omega_e) \qquad m_{reci} = m_p + \frac{1}{3} m_{cr} \tag{C.4}$$

The final expression for the mass torque felt at the crankshaft is found by multiplying this force by the crank angle dependent arm length ξ:

$$T_{mass} = F_p\,\xi(\varphi_e) \qquad \xi(\varphi_e) = r\left(\sin(\varphi_e) + \frac{\lambda \sin(2\varphi_e)}{2\sqrt{1-\lambda^2 \sin^2(\varphi_e)}} \right) \tag{C.5}$$

$$T_{mass} = -m_{reci}\,\xi(\varphi_e)\,r\,\omega_e^2\left(\cos(\varphi_e) + \frac{\lambda\cos(2\varphi_e)}{\sqrt{1-\lambda^2\sin^2(\varphi_e)}} + \frac{\lambda^3\sin^2(2\varphi_e)}{4\left(1-\lambda^2\sin^2(\varphi_e)\right)^{3/2}}\right)$$

$$-m_{reci}\,\xi(\varphi_e)^2\,\dot{\omega}_e \qquad \text{(C.6)}$$

Since the last term of (C.6) depends on engine acceleration, it can also be taken into account by adding:

$$J_{reci}(\varphi_e) = m_{reci}\xi(\varphi_e)^2 \qquad \text{(C.7)}$$

to the engine inertia. By doing this, it is seen that the total engine inertia varies with crank angle.

The single cylinder reciprocating mass torque is displayed for a full four-stroke cycle (two revolutions) in figure C.2. It can be seen clearly that it scales quadratically with engine speed.

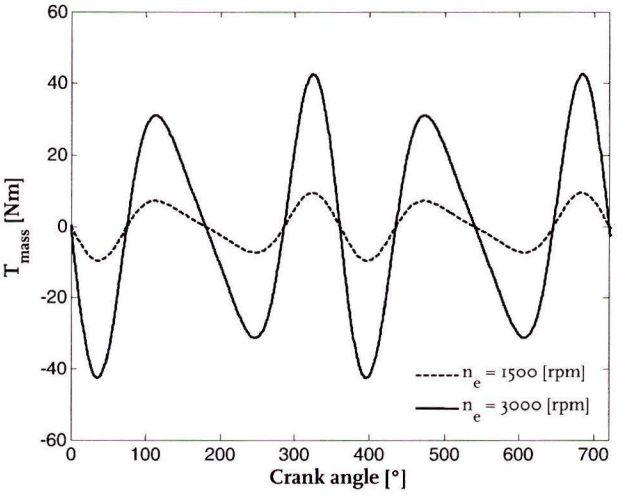

Figure C.2: reciprocating mass torque

C.2 Compression / expansion torque

The first component of the torque caused by gas forces is due to compression/expansion effects. In the following analysis, it is assumed that:

- valve opening and closing takes at place exactly at TDC and BDC
- gas exchange happens instantaneously as soon as a valve opens
- compression takes place under adiabatic conditions

Valve timing and various losses are not taken into account because this would result in an approach which is far too complex for the applications described in this report. Under the mentioned assumptions, cylinder pressure during the compression stroke is described by:

$$p(\varphi_e) = p_{intake} \qquad \text{for: } 0 < \varphi_e < \pi \tag{C.8}$$

Where the intake manifold pressure depends on throttle valve angle. Similarly, cylinder pressure during the exhaust stroke is described by:

$$p(\varphi_e) = p_{exhaust} \qquad \text{for: } 3\pi < \varphi_e < 4\pi \tag{C.9}$$

Exhaust manifold pressure is assumed to be constant, at a value close to ambient pressure. As mentioned above, cylinder pressure during compression/expansion is modeled as an adiabatic process. The cylinder volume equals:

$$V(\varphi_e) = V_c + A_{cyl}\, x(\varphi_e) \qquad A_{cyl} = \frac{\pi d^2}{4} \tag{C.10}$$

The clearance volume in (C.10) can be written in terms of displacement volume and compression ratio:

$$V_c = \frac{V_d}{(\varepsilon - 1)} = \frac{2r\, A_{cyl}}{(\varepsilon - 1)} \tag{C.11}$$

When substituted, the expression for cylinder volume equals:

$$V(\varphi_e) = r\, A_{cyl}\left(\frac{2}{(\varepsilon - 1)} + (1 - \cos(\varphi_e) + \frac{1}{\lambda}(1 - \sqrt{1 - \lambda^2 \sin^2(\varphi_e)} \right) \tag{C.12}$$

Under adiabatic conditions $pV^{\kappa} = constant$, resulting in the following relation between cylinder pressure and volume:

$$\frac{p}{p_o} = \left(\frac{V_o}{V} \right)^{\kappa}$$

$$p(\varphi_e) = p_{intake} \left(\frac{V_c + V_d}{V(\varphi_e)} \right)^{\kappa} \qquad \text{for: } \pi < \varphi_e < 3\pi \tag{C.13}$$

Again, the intake manifold pressure in (C.13) depends strongly on throttle valve angle. Now an estimation for the cylinder pressure over the complete four-stroke cycle is available.

Multiplying the pressure difference over the piston with its surface results in the force acting on the crank mechanism:

$$F_p = A_{cyl}(p(\varphi_e) - p_{amb}) \tag{C.14}$$

Crankshaft torque due to compression/expansion is found by multiplying this force with the expression for the angle dependent arm length, resulting in:

$$T_{ce}(\varphi_e, p_{intake}) = F_p\, \xi(\varphi_e) = A_{cyl}(p(\varphi_e) - p_{amb})\, \xi(\varphi_e) \tag{C.15}$$

Figure C.3(a) shows the cylinder pressure resulting from compression/expansion for two different operating points. One curve corresponds to a slightly opened throttle (p_{intake} = 0.5 bar) and the other to a large throttle opening (p_{intake} = 0.9 bar). Corresponding crankshaft torques are displayed in figure C.3(b).

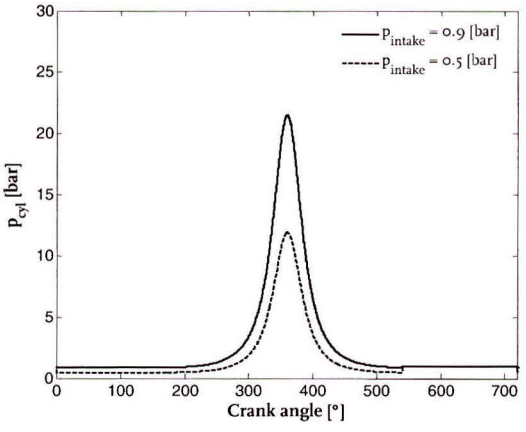

Figure C.3(a): comp./exp. pressure

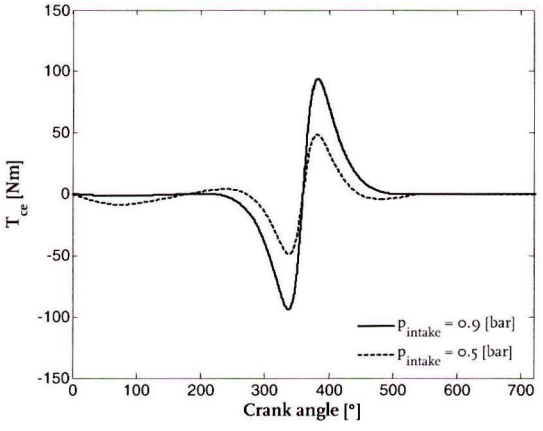

Figure C.3(b): comp./exp. torque

C.3 Combustion torque

The second component of the torque caused by gas forces is a result of the combustion process taking place. An empirical approach is used to model this torque source. The so-called *Isermann* empirical model [8] uses two parameters to describe the contribution of combustion torque during the power stroke. These parameters are the static torque level and the angle at which the combustion torque reaches its maximum value:

$$T_{comb}(\varphi_e, T_{stat}, \varphi_{max}) = \frac{16\,\pi\, T_{stat}}{(\varphi_{max})^3} \cdot \varphi_e^2 \cdot e^{-2\frac{\varphi_e}{\varphi_{max}}} \qquad \text{for:} \quad 0 < \varphi_e < 2\pi \tag{C.16}$$

The angle of maximum combustion torque varies with ignition timing. Integration of (C.16) over a full four-stroke cycle and dividing it by two revolutions results in the average torque value, which corresponds exactly to the requested static torque:

$$\frac{1}{4\pi}\int_{o}^{4\pi} T_{comb}(\varphi)\,d\varphi = T_{stat} \tag{C.17}$$

The influence of both shape parameters on the combustion torque is visualised in figure C.4. In figure C.4(a) the angle of maximum combustion torque is fixed and the static torque output is varied (note that this is still a single-cylinder representation, meaning that a static torque if 30 Nm corresponds to 120 Nm for a four cylinder engine). In figure C.4(b) the static torque output is fixed and the angle of maximum combustion torque is varied.

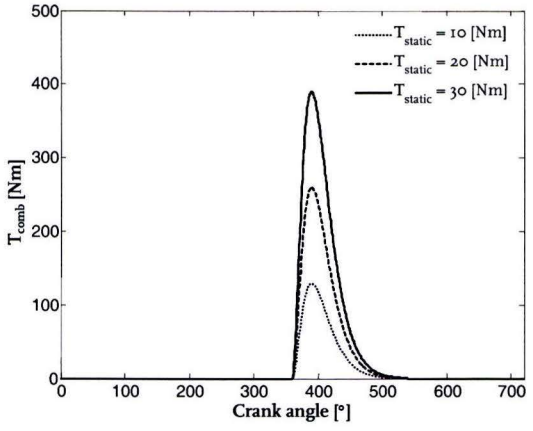

Figure C.4(a): static torque

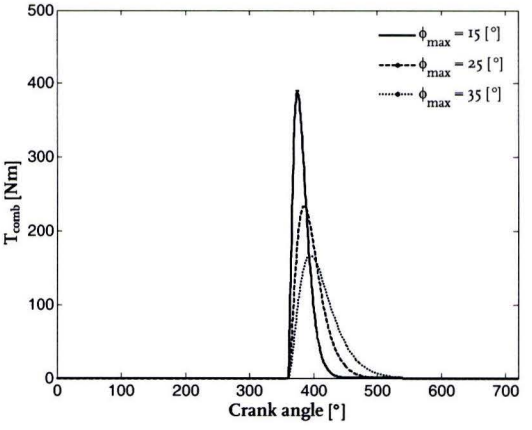

Figure C.4(b): max. combustion torque angle

C.4 Full engine

All three torque components can now be added to form the single-cylinder dynamic torque:

$$T_{cyl} = T_{mass}(\varphi_e, \omega_e) + T_{ce}(\varphi_e, p_{intake}) + T_{comb}(\varphi_e, T_{stat}, \varphi_{max}) \tag{C.18}$$

Dynamic torque output of the full engine can be found by phase-shifting all cylinders and adding them according to:

$$T_e = \sum_{i=o}^{n_{cyl}-1} T_{cyl}\left(\varphi_e + i\frac{4\pi}{n_{cyl}}\right) \tag{C.19}$$

In figure C.5(a) the single-cylinder dynamic torque, along with its components is displayed for a random engine operating point. Figure C.5(b) displays all phase-shifted cylinders along with their sum.

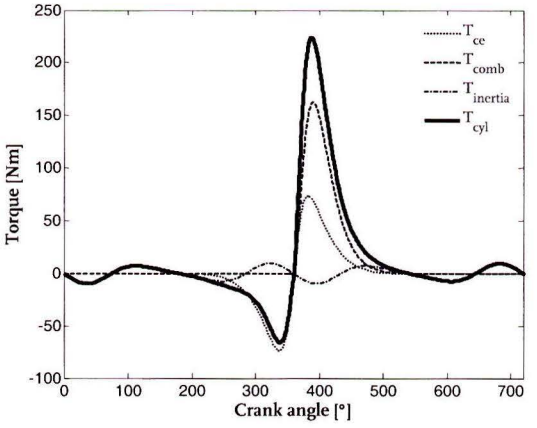

Figure C.5(a): single cylinder torque

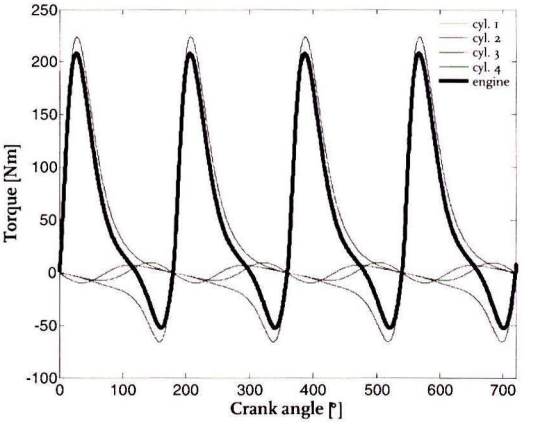

Figure C.5(b): full engine torque

The rotational form of the reciprocating masses, as explained in C.1, must also be summed for all cylinders. Total engine inertia now becomes the sum of a static crankshaft/flywheel inertia and all reciprocating contributors:

$$J_e(\varphi_e) = J_{static} + \sum_{i=0}^{n_{cyl}-1} J_{reci}(\varphi_e + i\frac{4\pi}{n_{cyl}}) \tag{C.20}$$

Newton's second law for the engine inertia can now be expressed as:

$$\begin{aligned} J_e(\varphi_e)\,\dot{\omega}_e &= (T_{mass} + T_{ce} + T_{comb}) - T_{e,fric} - T_{load} \\ J_e(\varphi_e)\,\dot{\omega}_e &= T_e - T_{e,fric} - T_{load} \end{aligned} \tag{C.21}$$

Appendix D

Linear models

D.1 Drive modes

To enable a linear analysis of the IS²-CVT drivetrain in the frequency domain, the system is linearized around a stationary state. It represents a vehicle driving at a constant speed on a flat road without braking. Furthermore, CVT ratio remains fixed. Depending on which operating mode is being analysed, one or both clutches are fully closed. Rolling resistance and efficiency losses are neglected. The input to the system is an external engine torque. Outputs are the acceleration levels behind the torsion damper and at the vehicle mass.

The system can be described by a set of equations:

$$\dot{x}(t) = f\left(x(t)\right) + Bu(t)$$

After linearization around the operating point of interest (x_o, u_o) the system can be written in its standard linear form:

$$\delta\dot{x} = \left.\frac{\delta f(x)}{\delta x}\right|_{x_o} \delta x + B\delta u$$

$$\dot{\bar{x}} = A\bar{x} + Bu \qquad\qquad u = \left[T_e\right]$$

D.1.1 CVT mode

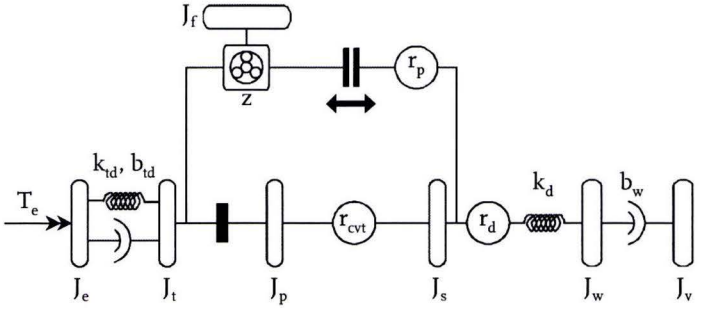

$$x = \left[\omega_e \quad T_{td} \quad \omega_t \quad T_d \quad \omega_w \quad \omega_v\right]^T$$

$$A(1,1) = 0$$

$$A(1,2) = -\frac{1}{J_e}$$

$$A(1,3...6) = 0$$

$$A(2,1) = k_{td}$$

$$A(2,2) = -\frac{b_{td}}{J_e} - \frac{b_{td}}{J^*}$$

$$A(2,3) = -k_{td}$$

$$A(2,4) = \frac{b_{td} r_d r_{cvt}}{J^*}$$

$$A(2,5...6) = 0$$

$$A(3,1) = 0$$

$$A(3,2) = \frac{1}{J^*}$$

$$A(3,3) = 0$$

$$A(3,4) = -\frac{r_d r_{cvt}}{J^*}$$

$$A(3,5...6) = 0$$

$$A(4,1...2) = 0$$

$$A(4,3) = k_d r_d r_{cvt}$$

$$A(4,4) = 0$$

$$A(4,5) = -k_d$$

$$A(4,6) = 0$$

$$A(5,1...3) = 0$$

$$A(5,4) = \frac{1}{J_w}$$

$$A(5,5) = -\frac{b_w m_{v,f} g v_0}{J_w \omega_{w,0}^2}$$

$$A(5,6) = \frac{b_w m_{v,f} g}{J_w \omega_{w,0}}$$

$$A(6,1...4) = 0$$

$$A(6,5) = \frac{b_w m_{v,f} g v_0}{\left(m_v + \frac{J_w}{R_w^2}\right) R_w \omega_{w,0}^2}$$

$$A(6,6) = -\frac{\frac{b_w m_{v,f} g}{R_w \omega_{w,0}} + \rho c_w A v_0}{m_v + \frac{J_w}{R_w^2}}$$

$$B(1,1) = \frac{1}{J_e}$$

$$B(2,1) = \frac{b_{td}}{J_e}$$

$$B(3...6,1) = 0$$

With: $J^* = J_t + J_p + J_s r_{cvt}^2$

D.1.2 Zero Inertia mode

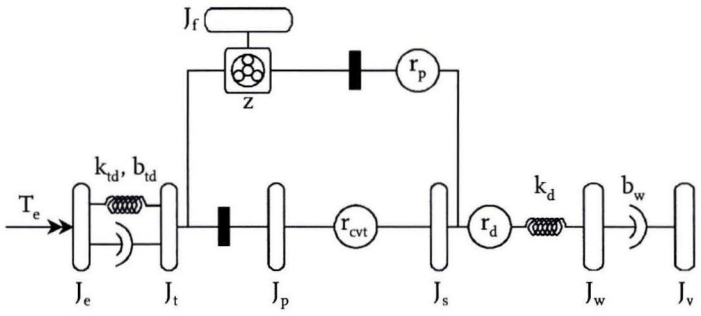

$$x = \begin{bmatrix} \omega_e & T_{td} & \omega_t & T_d & \omega_w & \omega_v \end{bmatrix}^T$$

$A(1,1) = 0$

$A(1,2) = -\frac{1}{J_e}$

$A(1,3...6) = 0$

$A(2,1) = k_{td}$

$A(2,2) = -\frac{b_{td}}{J_e} - \frac{b_{td}}{J^*}$

$A(2,3) = -k_{td}$

$A(2,4) = \frac{b_{td} r_d r_{cvt}}{J^*}$

$A(2,5...6) = 0$

$A(3,1) = 0$

$A(3,2) = \frac{1}{J^*}$

$A(3,3) = 0$

$A(4,1...2) = 0$

$A(4,3) = k_d r_d r_{cvt}$

$A(4,4) = 0$

$A(4,5) = -k_d$

$A(4,6) = 0$

$A(5,1...3) = 0$

$A(5,4) = \frac{1}{J_w}$

$A(5,5) = -\frac{b_w m_{v,f} g v_0}{J_w \omega_{w,0}^2}$

$A(5,6) = \frac{b_w m_{v,f} g}{J_w \omega_{w,0}}$

$A(6,1...4) = 0$

$A(6,5) = \frac{b_w m_{v,f} g v_0}{\left(m_v + \frac{J_w}{R_w^2}\right) R_w \omega_{w,0}^2}$

$$A(3,4) = -\frac{r_d r_{cvt}}{J^*} \qquad A(6,6) = -\frac{\frac{b_w m_{v,f} g}{R_w \omega_{w,o}} + \rho c_w A v_o}{\left(m_v + \frac{J_w}{R_w^2}\right)}$$

$$A(3,5...6) = 0$$

$$B(1,1) = \frac{1}{J_e}$$

$$B(2,1) = \frac{b_{td}}{J_e}$$

$$B(3...6,1) = 0$$

Where: $$J^* = J_t + J_p + \frac{J_s}{r_{cvt}^2} + J_f \left(\frac{z+1}{r_p} r_{cvt} - z\right)^2$$

D.1.3 Impulse Shift mode

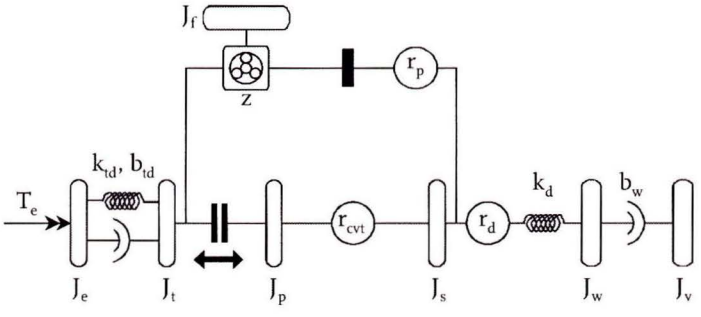

$$x = \left[\omega_e \quad T_{td} \quad \omega_t \quad \omega_s \quad T_d \quad \omega_w \quad \omega_v\right]^T$$

$$A(1,1) = 0 \qquad A(4,3...4) = 0$$

$$A(1,2) = -\frac{1}{J_e} \qquad A(4,5) = -\frac{r_d}{J_s^{**}}$$

$$A(1,3...7) = 0 \qquad A(4,6...7) = 0$$

$$A(2,1) = k_{td}$$

$$A(2,2) = -\frac{b_{td}}{J_e} - \frac{b_{td}}{J_t^{**}}$$

$$A(2,3) = -k_{td}$$

$$A(2,4) = 0$$

$$A(2,5) = \frac{b_{td} J_f (z^2 + z) r_d}{J_t^{**} J_s^{*} r_p}$$

$$A(2,6...7) = 0$$

$$A(3,1) = 0$$

$$A(3,2) = \frac{1}{J_t^{**}}$$

$$A(3,3...4) = 0$$

$$A(3,5) = -\frac{J_f (z^2 + z) r_d}{J_t^{**} J_s^{*} r_p}$$

$$A(3,6...7) = 0$$

$$A(4,1) = 0$$

$$A(4,2) = \frac{J_f (z^2 + z)}{J_s^{**} J_t^{*} r_p}$$

$$A(5,1...3) = 0$$

$$A(5,4) = k_d r_d$$

$$A(5,5) = 0$$

$$A(5,6) = -k_d$$

$$A(5,7) = 0$$

$$A(6,1...4) = 0$$

$$A(6,5) = \frac{1}{J_w}$$

$$A(6,6) = -\frac{b_w m_{v,f} g v_0}{J_w \omega_{w,0}^2}$$

$$A(6,7) = \frac{b_w m_{v,f} g}{J_w \omega_{w,0}}$$

$$A(7,1...5) = 0$$

$$A(7,6) = \frac{b_w m_{v,f} g v_0}{\left(m_v + \frac{J_w}{R_w^2}\right) R_w \omega_{w,0}^2}$$

$$A(7,7) = -\frac{\frac{b_w m_{v,f} g}{R_w \omega_{w,0}} + \rho c_w A v_0}{\left(m_v + \frac{J_w}{R_w^2}\right)}$$

$$B(1,1) = \frac{1}{J_e}$$

$$B(2,1) = \frac{b_{td}}{J_e}$$

$$B(3...7,1) = 0$$

D.2 Engine start mode

For the first and third construction phase the drivetrain representation can be reduced substantially, since there is no connection between the engine and the rest of the drivetrain. During the second construction phase a connection towards the wheels exists via the planetary gear. In this case it is assumed that the transmission is in 'park', connecting the secondary pulley to the transmission housing, and the brakes are applied.

Again, linear models are constructed in which an external engine torque is the input and torsion damper acceleration is the output.

D.2.1 Construction phases 1 and 3

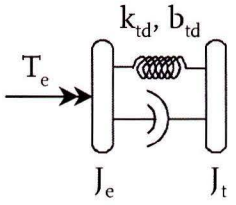

$$x = \begin{bmatrix} \omega_e & T_{td} & \omega_t \end{bmatrix}^T$$

$$A(1,1) = 0 \qquad A(2,3) = -k_{td}$$

$$A(1,2) = -\frac{1}{J_e} \qquad A(3,1) = 0$$

$$A(1,3) = 0 \qquad A(3,2) = \frac{1}{J_t}$$

$$A(2,1) = k_{td} \qquad A(3,3) = 0$$

$$A(2,2) = -\frac{b_{td}}{J_e} - \frac{b_{td}}{J_t}$$

$$B(1,1) = \frac{1}{J_e}$$

$$B(2,1) = \frac{b_{td}}{J_e}$$

$$B(3,1) = 0$$

D.2.2 Construction phase 2

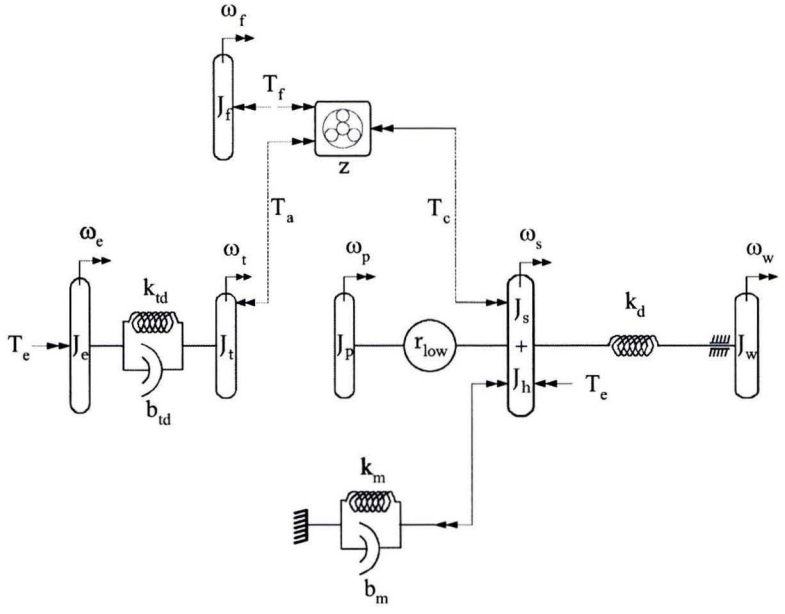

$$x = \left[\omega_e \quad T_{td} \quad \omega_t \quad \omega_b \quad T_d \quad T_m\right]^T \qquad u = \left[T_e\right]$$

$$A(1,1) = 0$$

$$A(1,2) = -\frac{1}{J_e}$$

$$A(1,3...6) = 0$$

$$A(2,1) = k_{td}$$

$$A(2,2) = -\frac{b_{td}}{J_e} - \frac{b_{td}}{J_t^{**}}$$

$$A(2,3) = -k_{td}$$

$$A(2,4) = 0$$

$$A(2,5) = \frac{b_{td} J_f (z^2 + z)}{J_t^{**} J_h^{*}}$$

$$A(2,6) = -\frac{b_{td} J_f (z^2 + z)}{J_t^{**} J_h^{*}}$$

$$A(4,1) = 0$$

$$A(4,2) = \frac{J_f (z^2 + z)}{J_t^{*} J_h^{**}}$$

$$A(4,3...4) = 0$$

$$A(4,5) = -\frac{1}{J_h^{**}}$$

$$A(4,6) = \frac{1}{J_h^{**}}$$

$$A(5,1...3) = 0$$

$$A(5,4) = k_d$$

$$A(5,5...6) = 0$$

$$A(6,1) = 0$$

$$A(3,1) = 0$$

$$A(3,2) = \frac{1}{J_t^{**}}$$

$$A(3,3...4) = 0$$

$$A(3,5) = -\frac{J_f(z^2+z)}{J_t^{**}J_h^*}$$

$$A(3,6) = \frac{J_f(z^2+z)}{J_t^{**}J_h^*}$$

$$A(6,2) = -\frac{b_m J_f(z^2+z)}{J_t^* J_h^{**}}$$

$$A(6,3) = 0$$

$$A(6,4) = -k_m$$

$$A(6,5) = \frac{b_m}{J_h^{**}}$$

$$A(6,6) = -\frac{b_m}{J_h^{**}}$$

$$B(1,1) = \frac{1}{J_e}$$

$$B(2,1) = \frac{b_{td}}{J_e} + \frac{b_{td}J_f(z^2+z)}{J_t^{**}J_h^*}$$

$$B(3,1) = -\frac{J_f(z^2+z)}{J_t^{**}J_h^*}$$

$$B(4,1) = -\frac{1}{J_h^{**}}$$

$$B(5,1) = 0$$

$$B(6,1) = -\frac{b_m}{J_h^{**}}$$

Where:

$$J_t^* = J_t + z^2 J_f$$

$$J_t^{**} = J_t^* - \frac{{J_f}^2(z+1)^2}{J_h^*}$$

$$J_h^* = J_s + J_h + \frac{J_p}{r_{cvt}^2} + J_f(z+1)^2$$

$$J_h^{**} = J_h^* - \frac{{J_f}^2(z+1)^2}{J_t^*}$$

D.2.3 Dual-mass flywheel

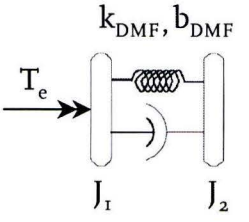

$$x = \begin{bmatrix} \omega_1 & T_{DMF} & \omega_2 \end{bmatrix}^T$$

$$A(1,1) = 0 \qquad A(2,3) = -k_{DMF}$$

$$A(1,2) = -\frac{1}{J_1} \qquad A(3,1) = 0$$

$$A(1,3) = 0 \qquad A(3,2) = \frac{1}{J_2}$$

$$A(2,1) = k_{DMF} \qquad A(3,3) = 0$$

$$A(2,2) = -\frac{b_{DMF}}{J_1} - \frac{b_{DMF}}{J_2}$$

$$B(1,1) = \frac{1}{J_1}$$

$$B(2,1) = \frac{b_{DMF}}{J_1}$$

$$B(3,1) = 0$$

$$k_{DMF} = 450 \ [Nm/rad] \qquad J_1 = 0.14 \ [kg\,m^2]$$

$$b_{DMF} = 0.5 \ [Nm\,s/rad] \qquad J_2 = 0.11 \ [kg\,m^2]$$

Appendix E

Impulse Start behaviour for different initial crank angles

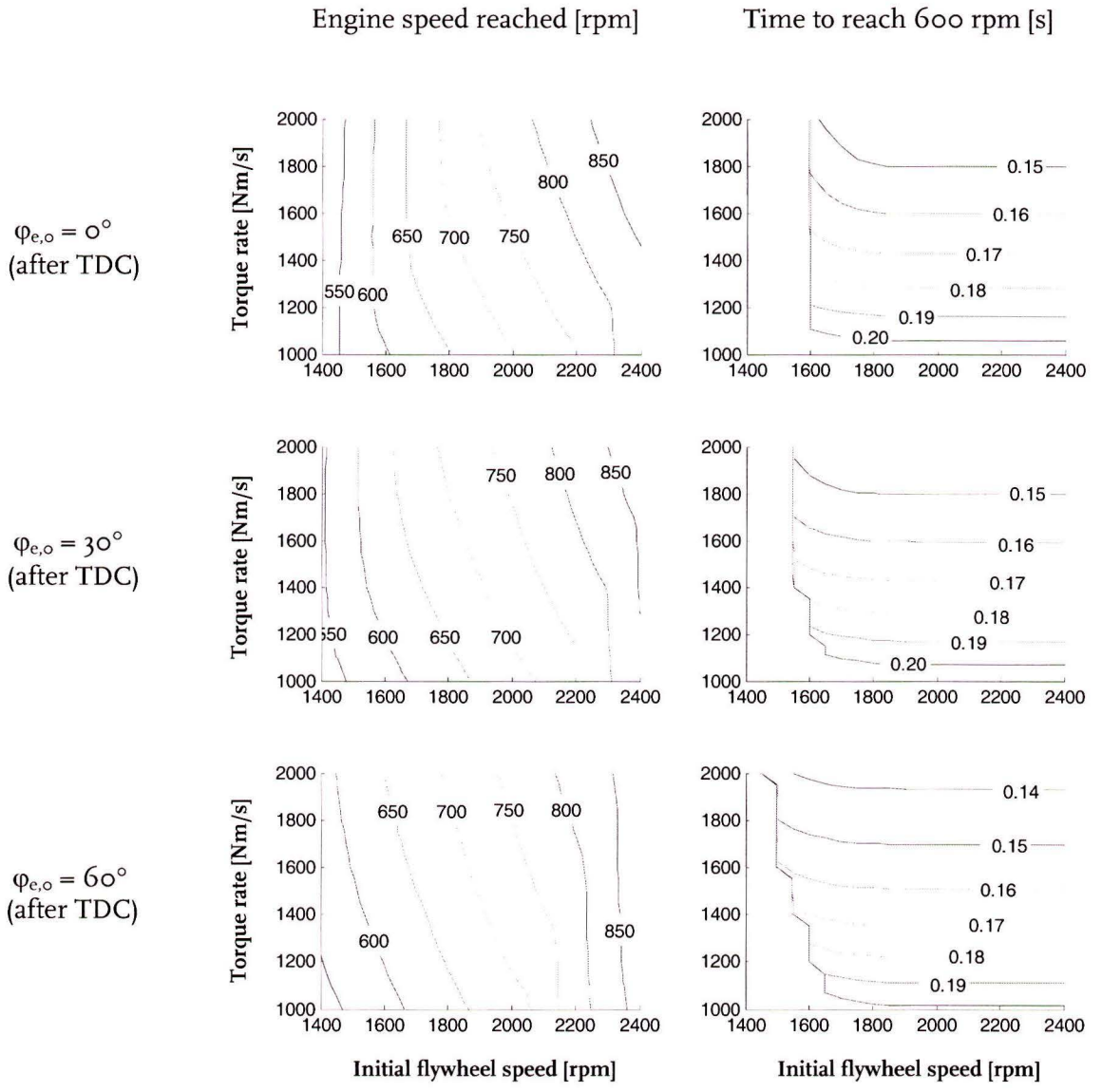

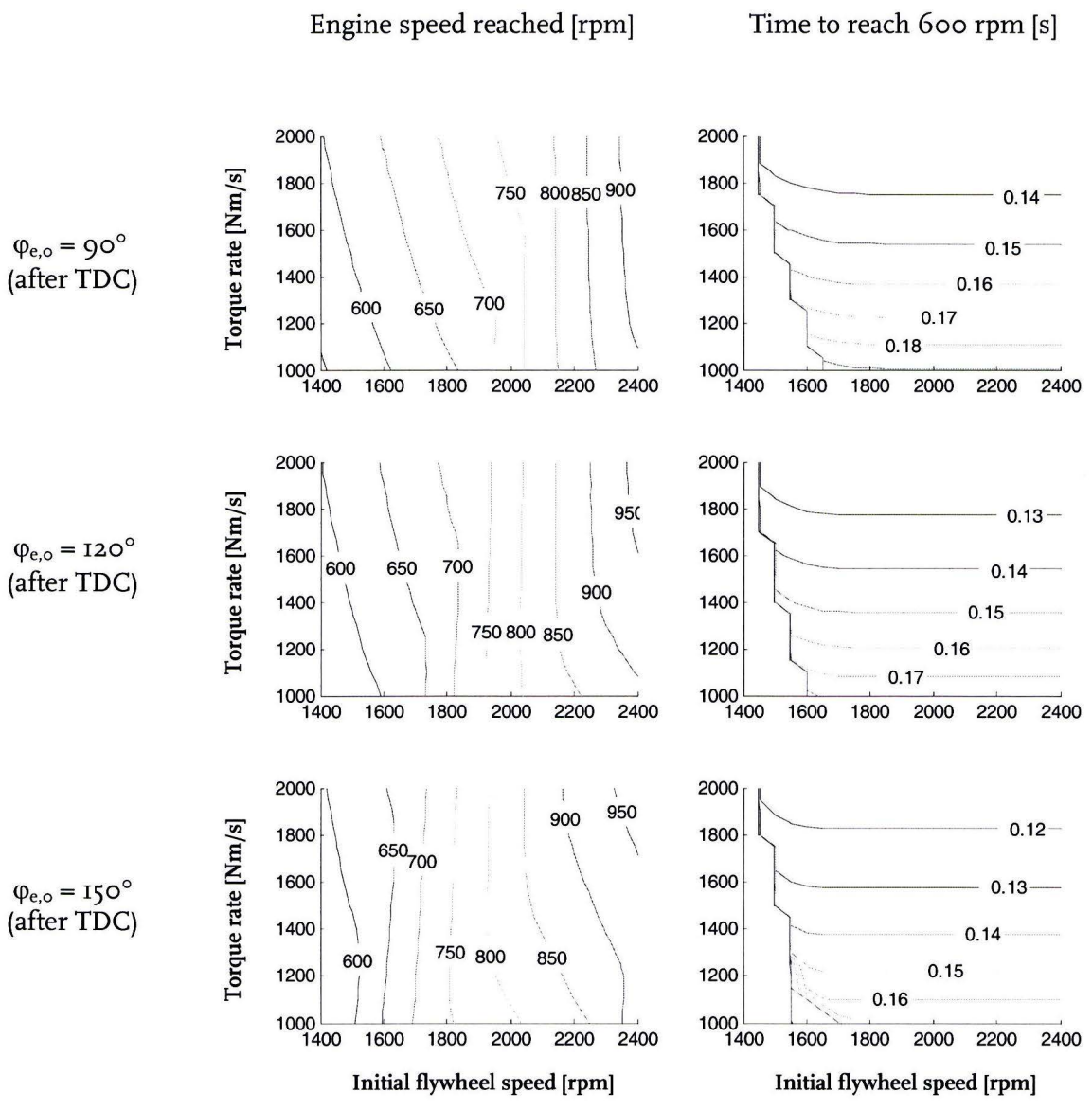
Engine speed reached [rpm]
Time to reach 600 rpm [s]
φe,o = 90° (after TDC)
φe,o = 120° (after TDC)
φe,o = 150° (after TDC)
Torque rate [Nm/s]
Initial flywheel speed [rpm]
600
650
700
750
800
850
900
950
0.12
0.13
0.14
0.15
0.16
0.17
0.18

Appendix F

Modelling of engine/transmission mount dynamics

The engine block and transmission housing are connected to the vehicle chassis by means of flexible mounts. A number of torques act on the engine block and transmission housing, see figure F.1.

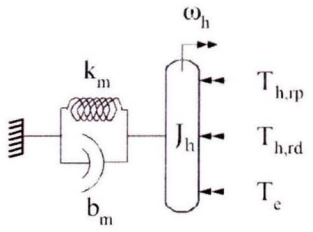

Figure F.1: engine block and transmission housing dynamics

Besides an engine reaction torque, reaction torques from various gear pairs act on the housing, see figure F.2.

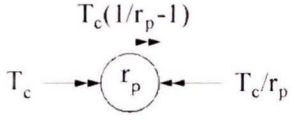

Figure F.2(a): connection gear

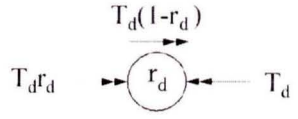

Figure F.2(b): final drive and differential

The dynamics of the engine/transmission block can now be described by:

$$J_h\dot{\omega}_h = T_m - T_e - T_{h,r_p} - T_{h,r_d} \qquad \text{With:} \qquad T_m = k_m\left(o-\varphi_h\right)+b_m\left(o-\omega_h\right)$$

$$T_{h,r_p} = T_c\left(\frac{1}{r_p}-1\right)$$

$$T_{h,r_d} = T_c\left(1-r_d\right)$$

Rotation of the transmission housing has an influence on its inner components, there where a kinematical connection exists. This means that relative rotation of the transmission housing needs to be superimposed on the equations of motion without mount dynamics.

Appendix G

Transmission hydraulics

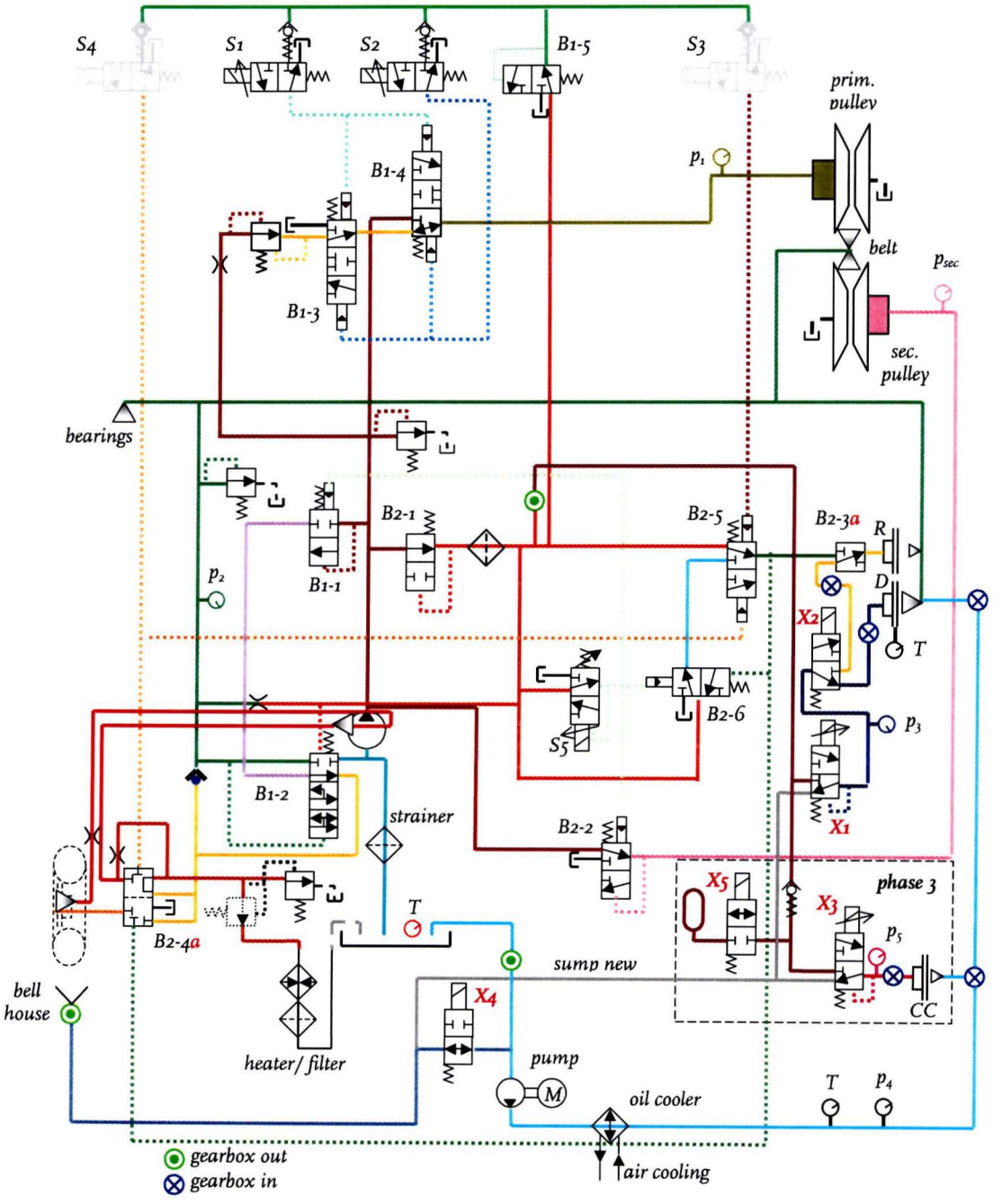

Appendix H

Efficiency maps and road-load characteristic

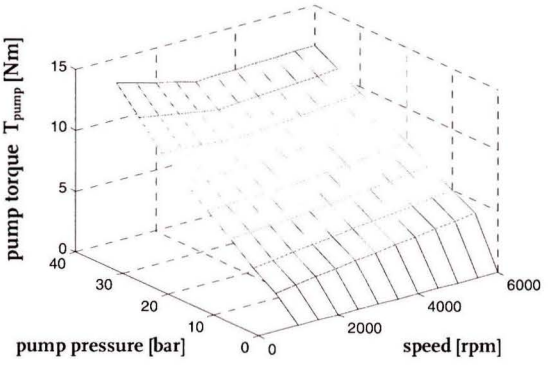

Figure H.1: hydraulic pump losses

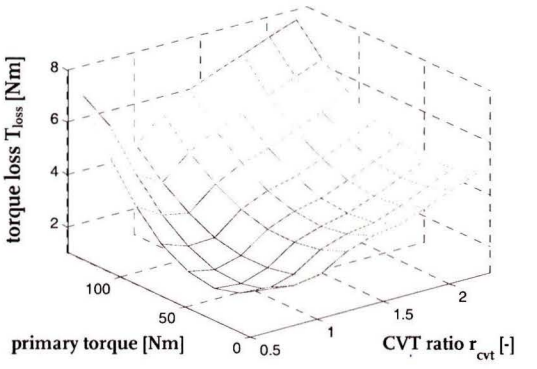

Figure H.2: mechanical CVT losses

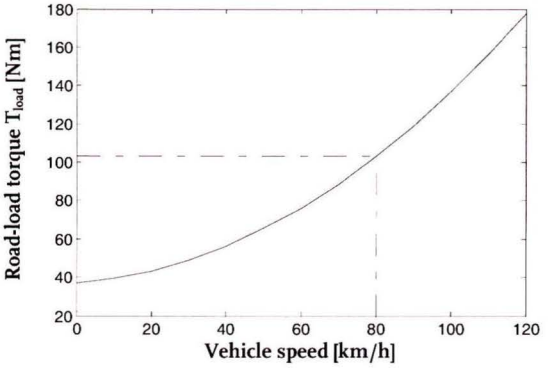

Figure H.3: road-load torque as a function of vehicle speed

Appendix I

Karnopp expression for sticking clutch

Karnopp expression for the sticking drive clutch:

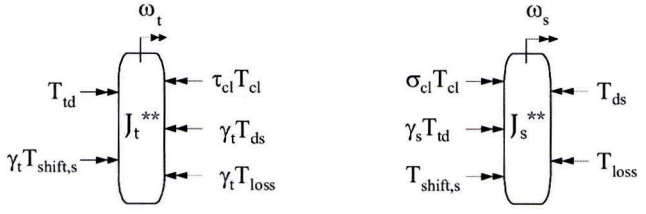

Figure I.1: lumped dynamics of the IS² system

Both decoupled differential equations derived earlier:

$$J_t^{**}\dot{\omega}_t = T_{td} - \tau_{cl}T_{cl} + \gamma_t\left(T_{shift,s} - T_{ds} - T_{loss}\right)$$
$$J_s^{**}\dot{\omega}_s = \sigma_{cl}T_{cl} + T_{shift,s} - T_{ds} - T_{loss} + \gamma_s T_{td}$$

Rewriting in terms of primary pulley speed:

$$\dot{\omega}_s = \dot{\omega}_p r_{cvt} + \omega_p \dot{r}_{cvt}$$
$$J_s^{**}\dot{\omega}_p r_{cvt} = \sigma_{cl}T_{cl} + T_{shift,s} - T_{ds} - T_{loss} + \gamma_s T_{td} - J_s^{**}\omega_p \dot{r}_{cvt}$$
$$T_{shift,p}^{*} = J_s^{**}\omega_p \dot{r}_{cvt} = \frac{J_s^{**}\omega_s \dot{r}_{cvt}}{r_{cvt}}$$
$$J_s^{**}\dot{\omega}_p r_{cvt} = \sigma_{cl}T_{cl} + T_{shift,s} - T_{ds} - T_{loss} + \gamma_s T_{td} - T_{shift,p}^{*}$$

Torsion damper and primary pulley accelerations are equal for a closed clutch:

$$\frac{\sigma_{cl}T_{cl} + T_{shift,s} - T_{ds} - T_{loss} + \gamma_s T_{td} - T_{shift,p}^{*}}{J_s^{**} r_{cvt}} = \frac{T_{td} - \tau_{cl}T_{cl} + \gamma_t\left(T_{shift,s} - T_{ds} - T_{loss}\right)}{J_t^{**}}$$

$$T_{cl} = \frac{-J_t^{**}\left(T_{shift,s} - T_{ds} - T_{loss} + \gamma_s T_{td} - T_{shift,p}^{*}\right) + J_s^{**} r_{cvt}\left\{T_{td} + \gamma_t\left(T_{shift,s} - T_{ds} - T_{loss}\right)\right\}}{J_t^{**}\sigma_{cl} + J_s^{**} r_{cvt}\tau_{cl}}$$

The Karnopp torque can finally be written in its standard form:

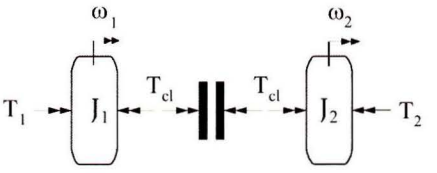

Figure I.2: standard form of the Karnopp clutch torque

$$T_{cl,karnopp} = \frac{J_1 T_2 + J_2 T_1}{J_1\sigma_{cl} + J_2\tau_{cl}}$$

Where:

$$J_1 = J_t^{**}$$
$$J_2 = J_s^{**} r_{cvt}$$
$$T_1 = T_{td} + \gamma_t\left(T_{shift,s} - T_{ds} - T_{loss}\right)$$
$$T_2 = T_{ds} + T_{loss} + T_{shift,p}^{*} - T_{shift,s} - \gamma_s T_{td}$$

Appendix J

Construction drawings

J.1 Reference Aisin AW transmission

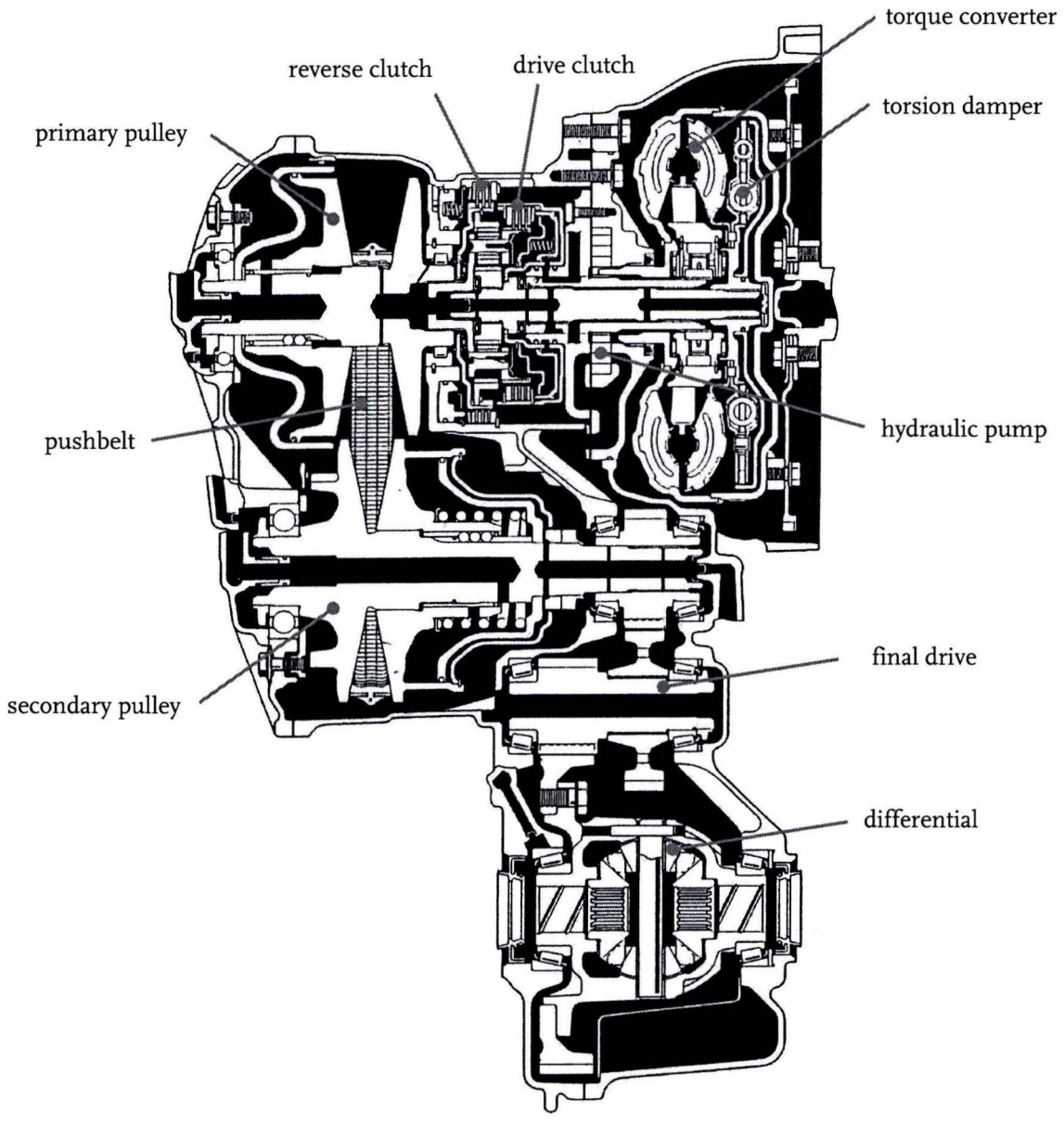

Figure J.1: **reference Aisin AW CVT**

J.2 IS²-CVT, construction phase 1

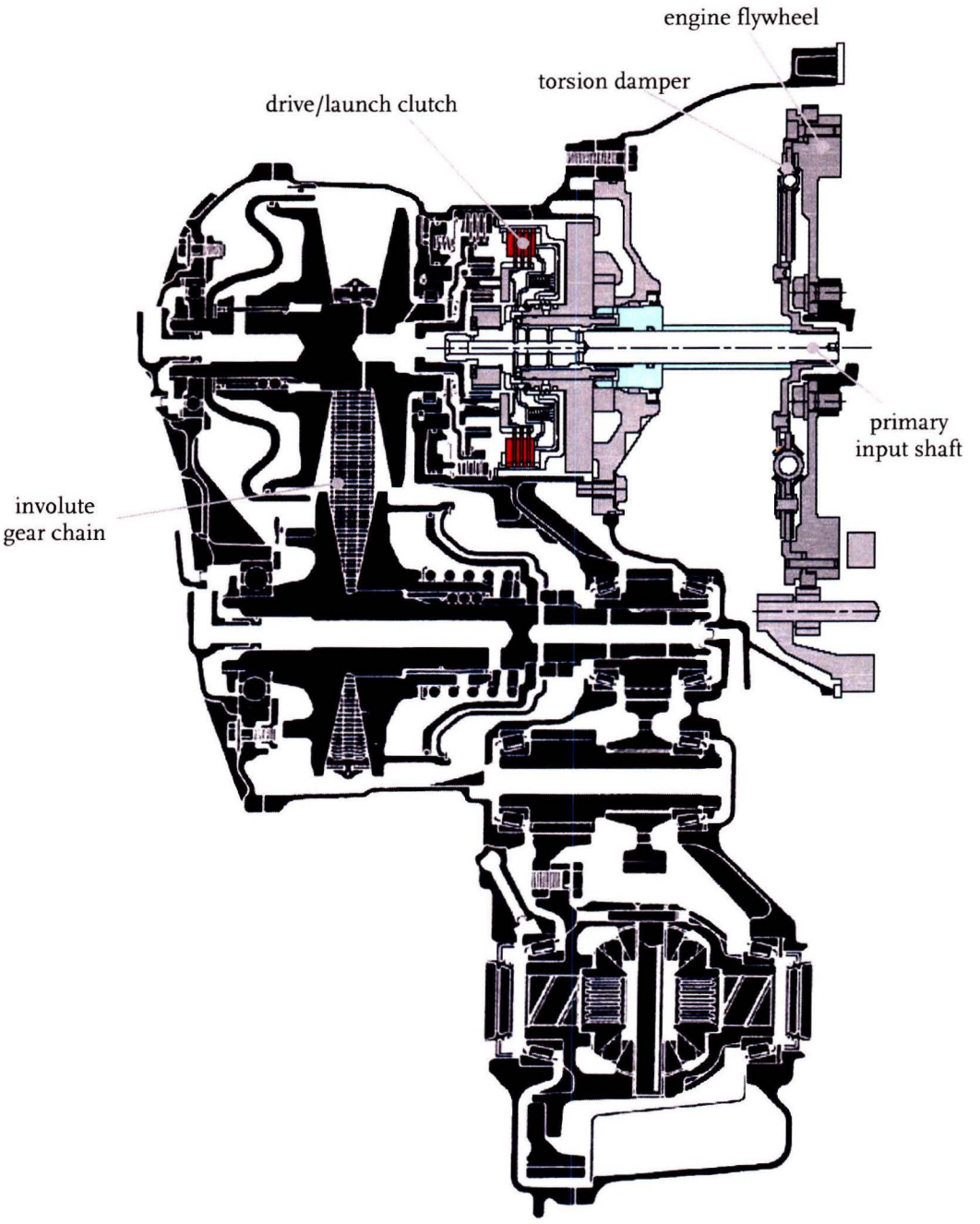

Figure J.2: IS²-CVT , construction phase 1

J.3 IS²-CVT, construction phase 2

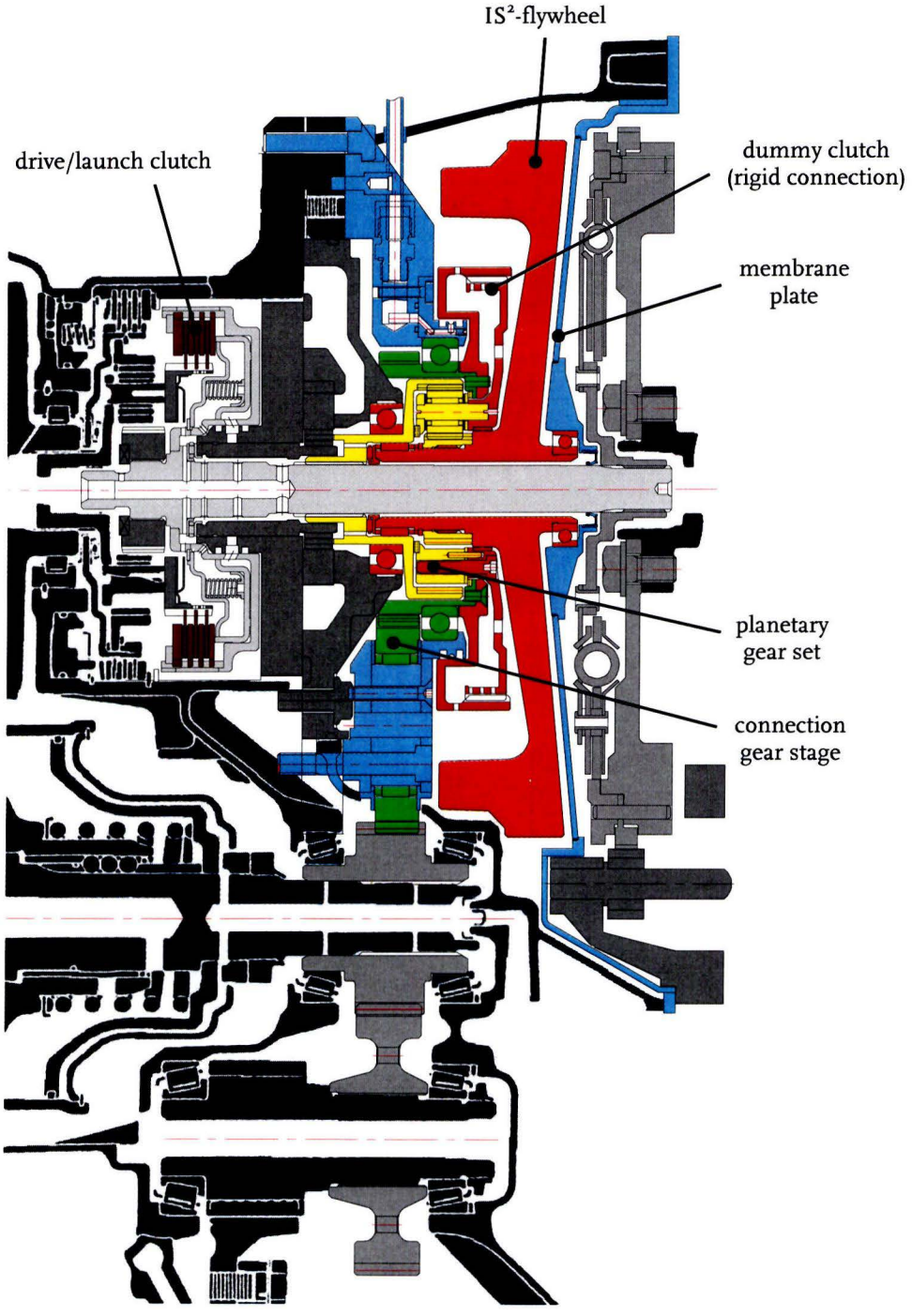

Figure J.3: **IS²-CVT , construction phase 2**

J.4 IS²-CVT, construction phase 3

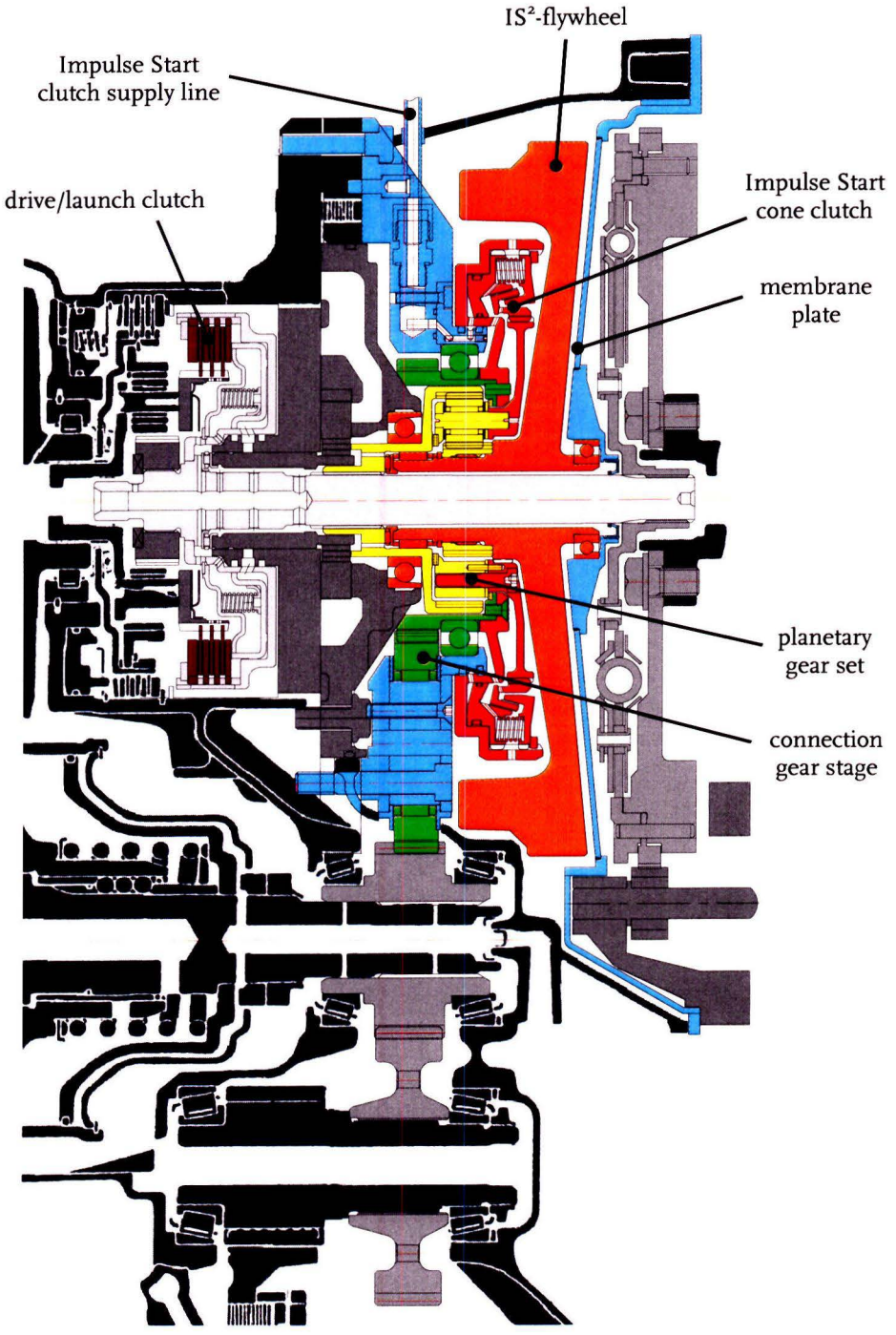

Figure J.4: IS²-CVT , construction phase 3